QUANTUM LIQUIDS AND QUANTUM CRYSTALS

On phase transitions in a Fermi liquid. I. The transition associated with rotational symmetry breaking in momentum space

A. S. Peletminsky

Science and Engineering Center of Electrophysical Treatment, National Academy of Sciences of the Ukraine, 310002 Kharkov, Ukraine

S. V. Peletminsky and Yu. V. Slyusarenko

*National Science Center ''Kharkov Institute of Physics and Technology,'' 310108 Kharkov, Ukraine**

(Submitted November 2, 1998)
Fiz. Nizk. Temp. **25**, 211–221 (March 1999)

A phase transition associated with the rotational symmetry breaking in momentum space in a Fermi liquid is considered. It is shown that the phase transition is connected with the violation of one of the Pomeranchuk conditions, viz., the criterion of normal state stability. The structure of flux densities of the additive integrals of motion is determined in the vicinity of the phase transition point, and a physical interpretation of the phase under investigation is also given. © *1999 American Institute of Physics.* [S1063-777X(99)00103-6]

INTRODUCTION

The phenomenological theory of a normal Fermi liquid (the basic principles of this theory were presented in fundamental works by Landau[1] and Silin[2]) presumes the fulfillment of the so-called Pomeranchuk conditions,[3] i.e., the relations determining the conditions for the stability of the static equilibrium state of a normal Fermi liquid and imposing certain constraints on the interactions between quasiparticles. If we make an attempt to remove such constraints, i.e., leave the stability boundaries for the ground state of a normal Fermi liquid, a natural assumption concerning a spontaneous transition of the system to a new equilibrium state should be made. In other words, the violation of the ground-state stability criteria must be associated with various kinds of phase transitions in the Fermi liquid (see, for example, Ref. 4).

The description of new equilibrium states emerging as a result of such phase transitions necessitates a certain modification of the Landau–Silin theory of a normal Fermi liquid. Above all, such a modification is dictated by the need of introducing new parameters describing the equilibrium state (order parameters). This is due to the fact that the symmetry of the new equilibrium state formed as a result of a phase transition is lower than the symmetry of the Hamiltonian (the state with spontaneously broken symmetry).

In this paper, we analyze the phase transition associated with the breaking of rotational symmetry in the momentum space of a normal Fermi liquid. it will be proved below that such a phase transition corresponds to the violation of the Pomeranchuk stability criterion for one of harmonics in the series expansion of the Landau amplitude in Legendre polynomials.

In the following analysis, we shall disregard the presence of an electric charge for a fermion, paying attention mainly to the properties that are common for charged and neutral Fermi liquids. The inclusion of effects connected with the presence of an electric charge in fermions would have complicated the establishment of the possibility of such a transition in various systems. One of the main goals of this publication is to demonstrate that such phase transitions can be described in principle.

1. STABILITY CRITERION FOR A NORMAL FERMI LIQUID

Before going over to a direct description of a phase transition involving the breaking of rotational symmetry of the momentum space, let us recall some basic concepts of the theory of a normal Fermi liquid, including the stability conditions for the normal state.

The theory of a normal Fermi liquid is based on the assumption concerning the functional dependence of the energy E (Hamiltonian) of the system on the one-particle fermion density matrix:

$$f_{\mathbf{p}_1\sigma_1;\mathbf{p}_2\sigma_2}=\mathrm{Tr}\,\rho(f)\,a^{+}_{\mathbf{p}_2\sigma_2}a_{\mathbf{p}_1\sigma_1}\equiv f_{12},$$

where $\mathbf{p}$ is the quasiparticle momentum, and the index σ labels the component of the fermion spin. The quantity $\rho(f)$ in this expression is the nonequilibrium statistical operator of an ideal gas of quasiparticles, defined as

$$\rho(f)=\exp\left(\Omega-\sum_{1,2}a_1^{+}A_{12}a_2\right), \tag{1}$$

In this formula, the quantities Ω and A_{12} should be determined from the relations

$$\mathrm{Tr}\,\rho(f)=1,\quad f_{12}=\mathrm{Tr}\rho(f)\,a_2^{+}a_1$$

(the trace is taken in the secondary quantization space).

Another important concept in constructing the theory of a normal Fermi liquid is the general definition of the entropy of the system:

$$S=-\operatorname{Tr}\rho(f)\ln\rho(f).$$

The calculation of the trace for the statistical operator (1) appearing in this formula leads to the combinatorial definition of entropy:

$$S=-\operatorname{tr}[f\ln f+(1-f)\ln(1-f)] \tag{2}$$

(the trace is calculated in the space of one-particle states).

It is well known that the equilibrium one-particle density matrix f_{12} is determined from the condition of entropy maximum for given values of energy functional $E(f)$, the number of particles $N=\operatorname{tr} f$, and momentum $P_i=\operatorname{tr} fp_i$. Introducing Lagrangian multipliers Y corresponding to the quantities E, N, and $\mathbf{P}$, we reduce the problem on conditional entropy maximum to the problem on absolute minimum of potential $\Omega(f)$:

$$\Omega(f)=-S(f)+Y_0E(f)+Y_i\operatorname{tr} fp_i+Y_4\operatorname{tr} f \tag{3}$$

[since the statistical equilibrium state presumes that the space is spatially homogeneous, the quantities S, E, P_i, and N are proportional to the volume V of the system and to $\Omega(f)=V\omega(f)$, where $\omega(f)$ is the density of potential $\Omega(f)$]. This variational principle leads to the following self-consistency condition:

$$f=\{\exp(Y_0\hat{\varepsilon}(f)+Y_i\hat{p}_i+Y_4)+1\}^{-1};$$

$$\varepsilon_{12}(f)=\partial E(f)/\partial f_{21}. \tag{4}$$

Here $Y_0=T^{-1}\equiv\beta$; $Y_i=-Y_0v_i$; $Y_4=-Y_0\mu$; T is the temperature, v_i the velocity of the Fermi liquid, and μ the chemical potential. This nonlinear equation defines the equilibrium one-particle density matrix for a Fermi liquid. The quantity $\hat{\varepsilon}(f)$ is a functional of the one-particle density matrix and is the energy operator for a quasiparticle.

In order to impart a physical meaning to Eq. (4), we must specify the energy $E(f)$ of the system. This functional can be chosen in the form

$$E(f)=\sum_{1,2}\varepsilon_{12}f_{21}+\frac{1}{2}(f_0,F_1f_0)+\frac{1}{2}(f_i,F_2f_i),$$

$$(f_0,F_1f_0)=\frac{1}{V}\sum_{\mathbf{p}_1\cdots\mathbf{p}_4}f_{0\mathbf{p}_1\mathbf{p}_2}F_1(\mathbf{p}_1,\mathbf{p}_2;\mathbf{p}_3,\mathbf{p}_4)f_{0\mathbf{p}_3\mathbf{p}_4},$$

$$(f_i,F_2f_i)=\frac{1}{V}\sum_{\mathbf{p}_1\cdots\mathbf{p}_4}(f_i)_{\mathbf{p}_1\mathbf{p}_2}F_2(\mathbf{p}_1,\mathbf{p}_2;\mathbf{p}_3,\mathbf{p}_4)(f_i)_{\mathbf{p}_3\mathbf{p}_4}, \tag{5}$$

where $f_0=\operatorname{tr}_\sigma\hat{f}$, $f_i=\operatorname{tr}_\sigma\hat{f}\sigma_i$, σ_i are the Pauli matrices, and the quantities F_1 and F_2 are the amplitudes of the potential and exchange interactions of quasiparticles respectively, which are known as Landau amplitudes (we assume that $E(f)$ is invariant to spin rotations).

Let us now find the conditions under which the solution of the self-consistent equations leads to the minimum of potential $\omega(f)$ for the normal state. For this purpose, we must define the second variation $\delta^2\omega(f)$ whose positive value corresponds to the stability of the normal state of a Fermi liquid (the first variation vanishes). For this purpose, we consider the spatially homogeneous equilibrium one-particle density matrix for the normal state:

$$f^0_{\mathbf{p}_1\sigma_1\mathbf{p}_2\sigma_2}=f^0_{p_1}\delta_{\mathbf{p}_1\mathbf{p}_2}\delta_{\sigma_1\sigma_2},$$

$$f^0_p=\{\exp[\beta(\varepsilon_p(f^0)-\mu)+1]\}^{-1}, \tag{6}$$

and define the spatially homogeneous density matrix associated with a deviation from the equilibrium state by the formula

$$\delta f_{\mathbf{p}_1\sigma_1;\mathbf{p}_2\sigma_2}=\delta_{\mathbf{p}_1\mathbf{p}_2}\delta f_{\mathbf{p}_1\sigma_1\sigma_2}.$$

It should be noted that δf commutes with f^0, and hence we can treat the matrices δf and f^0 as ordinary functions in the calculation of the second variation of entropy. Varying (2) and presenting $\delta f_{\mathbf{p}}$ in the form

$$\delta f_{\mathbf{p}}=f^0_p(1-f^0_p)(\delta\xi^0_{\mathbf{p}}+\sigma^i\delta\xi^i_{\mathbf{p}}),$$

we obtain

$$\delta^2S=-\frac{V}{(2\pi)^3}\int d^3pf^0_p(1-f^0_p)\{(\delta\xi^0_{\mathbf{p}})^2+\delta\xi^i_{\mathbf{p}}\delta\xi^i_{\mathbf{p}}\}. \tag{7}$$

It can also be easily seen that the second variation of the energy functional (5) leads to the formula

$$\delta^2E=2V\int\frac{d^3pd^3p'}{(2\pi)^6}f^0_p(1-f^0_p)f^0_{p'}(1-f^0_{p'})\times\{F_1(\mathbf{p},\mathbf{p}')\delta\xi^0_{\mathbf{p}}\delta\xi^0_{\mathbf{p}'}+F_2(\mathbf{p},\mathbf{p}')\delta\xi^i_{\mathbf{p}}\delta\xi^i_{\mathbf{p}'}\}, \tag{8}$$

where $F_i(\mathbf{p},\mathbf{p}')\equiv F_i(\mathbf{p},\mathbf{p};\mathbf{p}',\mathbf{p}')$, $i=1,2$. Thus, taking into account relations (3), (7), and (8) and noting also that the relation $f^0_p(1-f^0_p)\simeq T\delta(\varepsilon_p-\mu)$, is valid in the low-temperature region $T\ll\mu$, we can write the second variation of potential density ω in the form

$$\delta^2\omega=\delta^2\omega_1+\delta^2\omega_2, \tag{9}$$

where

$$\delta^2\omega_1=\frac{\nu(\mu)T}{2}\int\frac{dO}{4\pi}(\delta\xi^0(\mathbf{n}))^2+\frac{\nu(\mu)^2T}{2}\int\frac{dOdO'}{(4\pi)^2}F_1(\mathbf{n},\mathbf{n}')\delta\xi^0(\mathbf{n})\delta\xi^0(\mathbf{n}');$$

$$\delta^2\omega_2=\frac{\nu(\mu)T}{2}\int\frac{dO}{4\pi}\delta\xi_i(\mathbf{n})\delta\xi_i(\mathbf{n})+\frac{\nu(\mu)^2T}{2}\int\frac{dOdO'}{(4\pi)^2}F_2(\mathbf{n},\mathbf{n}')\delta\xi_i(\mathbf{n})\delta\xi_i(\mathbf{n}');$$

Here $\mathbf{n}=\mathbf{p}_F/p_F$; $\mathbf{n}'=\mathbf{p}'_F/p_F$;

$$\nu(\mu)=2\int\frac{d^3p}{(2\pi)^3}\delta(\varepsilon_p-\mu);$$

$$F_{1,2}(\mathbf{n},\mathbf{n}')\equiv F_{1,2}(\mathbf{p},\mathbf{p}')|_{p=p'=p_F};\quad \delta\xi_i(\mathbf{n})=\delta\xi^i_p|_{p=p_F}.$$

It follows from (9) that the condition for the positive second variation of the potential $\Omega=V\omega$ leads to the inequalities

$$1+\frac{\nu(\mu)F_l^{(1)}}{2l+1}>0, \quad 1+\frac{\nu(\mu)F_l^{(2)}}{2l+1}>0, \tag{10}$$

where $F_l^{(1)}$ and $F_l^{(2)}$ are the coefficients of expansion of the amplitudes $F_1(\mathbf{n},\mathbf{n}')$ and $F_2(\mathbf{n},\mathbf{n}')$ in the Legendre polynomials $P_l(\cos\theta)$, $\cos\theta=\mathbf{n}\cdot\mathbf{n}'$, i.e.,

$$F_1(\mathbf{n},\mathbf{n}')=\sum_{l=0}^{\infty} P_l(\cos\theta)F_l^{(1)},$$

$$F_2(\mathbf{n},\mathbf{n}')=\sum_{l=0}^{\infty} P_l(\cos\theta)F_l^{(2)}.$$

Relations (10), which were obtained for the first time by Pomeranchuk,[3] are the stability conditions for the equilibrium state if a normal Fermi liquid for all $T>0$. It was noted above that Pomeranchuk conditions can be violated due to various phase transitions in a normal Fermi liquid. This paper is devoted to the analysis of one of such phase transitions.

Let us recall preliminarily the theory of a magnetic phase transition in which the Pomeranchuk condition (10) for the Landau amplitude $F_l^{(2)}$ is violated for $l=0$. Noting that

$$\varepsilon_{\sigma\sigma'}=\frac{\partial E(\hat{f})}{\partial f_{\sigma'\sigma}}$$

and writing the quantities $f_{\sigma\sigma'}$ and $\varepsilon_{\sigma\sigma'}$ in the form

$$f=\tfrac{1}{2}(f_0+f_i\sigma_i), \quad \varepsilon=\tfrac{1}{2}(\varepsilon_0+\varepsilon_i\sigma_i),$$

we obtain

$$\varepsilon_0=2\frac{\partial E}{\partial f_0}, \quad \varepsilon_i=2\frac{\partial E}{\partial f_i}.$$

Consequently, in accordance with (5), we can write the self-consistency condition (4) in the form

$$\varepsilon_i=\frac{2}{V}\sum_{\mathbf{p}'} F_0^{(2)}(p,p')f_i(p'), \tag{11}$$

where $f_i(p')$ is defined, in view of (4), from the relations

$$f_i(p)=\operatorname{tr}\sigma_i\{\exp\beta(\varepsilon-\mu)+1\}^{-1},$$

$$\varepsilon=\tfrac{1}{2}(\varepsilon_0+\varepsilon_i\sigma_i). \tag{12}$$

In the normal state, $\varepsilon_i=0$. Consequently, the function $\varepsilon_i(\mathbf{p})$ plays the role of the order parameter. In accordance with (12), Eq. (11) in the region of small ε_i assumes the following form in the main approximation in ε_i:

$$\varepsilon_i(p)=\frac{2}{V}\sum_{\mathbf{p}'} F_0^{(2)}(p,p')\frac{\partial f_{p'}^0}{\partial\varepsilon_{\mathbf{p}'}^0}\varepsilon_i(p'),$$

$$F_0^{(2)}(p,p')=\frac{1}{4\pi}\int dO F_2(\mathbf{p},\mathbf{p}'),$$

where

$$f_p^0=\{\exp\beta_c(\varepsilon^0-\mu)+1\}^{-1}.$$

This homogeneous equation for $\varepsilon_i(p)$ can be used to determine the critical temperature β_c. If the amplitude $F_0^{(2)}(p,p')$ weakly depends on p and p', the solution of this equation can be written in the form

$$\varepsilon_i(p)=\frac{F_0^{(2)}(p,p_F)}{F_0^{(2)}(p_F,p_F)}\varepsilon_i,$$

the critical temperature β_c being defined from the equation

$$1=-2F_0^{(2)}\frac{\partial n(\beta_c,\mu)}{\partial\mu},$$

where

$$F_0^{(2)}=F_0^{(2)}(p_F,p_F),$$

$$n(\beta,\mu)=\frac{1}{V}\sum_{\mathbf{p}}\{\exp\beta(\varepsilon_p^0-\mu)-1\}^{-1}.$$

In order to find the functions $n(\beta,\mu)$ in the region of small $\beta^{-1}\ll\mu$, we shall use the low-temperature expansion

$$\frac{\partial f_p^0(\beta,\mu)}{\partial\mu}=\delta(\varepsilon-\mu)+\frac{T^2}{6}\pi^2\delta''(\varepsilon-\mu)+\ldots$$

which gives

$$T_c^2=\beta_c^{-2}=-\frac{6}{\pi}\frac{1+F_0^{(2)}\nu(\mu)}{F_0^{(2)}\nu''(\mu)}. \tag{13}$$

Since $T_c\ll\mu$ (the condition for the applicability of the theory of a Fermi liquid) and $\nu''(\mu)\sim\nu(\mu)\mu^{-2}$, we have $F_0^{(2)}\nu(\mu)\approx-1$. Considering that $\nu''(\mu)<0$ and $T_c^2>0$, we obtain $1+F_0^{(2)}\nu(\mu)<0$, i.e., we are dealing with the situation when the Pomeranchuk condition is violated, which leads to the emergence of a magnetically ordered phase. Retaining terms proportional to ε^3 ($\varepsilon=|\boldsymbol{\varepsilon}|$) in the expansion (12) into a power series in ε_i, we can easily prove that

$$\varepsilon^2=-6\frac{\partial^2 n/\partial\beta\partial\mu}{\partial^3 n/\partial\mu^3}(\beta-\beta_c). \tag{14}$$

Using the above temperature expansion, we can easily obtain from (14) the relation

$$\varepsilon^2=2T_c(T_c-T). \tag{15}$$

Knowing the expression for ε, we can find the expression for the ''magnetization'' density:

$$\sigma=\left|\frac{1}{V}\sum_{\mathbf{p}}\operatorname{tr}\sigma f\right|=\left|\frac{1}{V}\sum_{\mathbf{p}}\mathbf{f}_{\mathbf{p}}\right|=-\frac{\partial n}{\partial\mu}\varepsilon.$$

From Eq. (15) we obtain

$$\sigma=\frac{1}{2}\nu(\mu)T_c\sqrt{1-T^2/T_c^2}. \tag{16}$$

2. PHASE TRANSITION ASSOCIATED WITH ROTATIONAL SYMMETRY BREAKING IN MOMENTUM SPACE

In this section, we study the phase transition associated with rotational symmetry breaking in momentum space. It will be proved in subsequent analysis that such a phase

transition is associated with the violation of the Pomeranchuk condition (10) for the amplitude $F_l^{(1)}$ of potential interaction.

Let us consider the equilibrium state of a stationary ($v_i=0$) spatially homogeneous Fermi liquid. In zero magnetic fields and under the assumption that the phase transition is not associated with the emergence of spontaneous magnetization, we present the quantities $\varepsilon_{\mathbf{p}_1\sigma_1\mathbf{p}_2\sigma_2}$ and $f_{\mathbf{p}_1\sigma_1\mathbf{p}_2\sigma_2}$ in the form

$$\varepsilon_{\mathbf{p}_1\sigma_1\mathbf{p}_2\sigma_2}=\varepsilon_{p_1}^{(0)}\delta_{\mathbf{p}_1\mathbf{p}_2}\delta_{\sigma_1\sigma_2},\quad f_{\mathbf{p}_1\sigma_1\mathbf{p}_2\sigma_2}=f_{\mathbf{p}_1}\delta_{\mathbf{p}_1\mathbf{p}_2}\delta_{\sigma_1\sigma_2}.$$

In this case, the energy functional (5) is defined as

$$E(f)=2\sum_{\mathbf{p}}\ \varepsilon_p^{(0)}f_{\mathbf{p}}+\frac{2}{V}\sum_{\mathbf{p}_1,\mathbf{p}_2}\ f_{\mathbf{p}_1}F(\mathbf{p}_1,\mathbf{p}_2)f_{\mathbf{p}_2},$$

$$f_{\mathbf{p}}\equiv\frac{1}{2}f_{0\mathbf{p}},\quad F_1\equiv F. \tag{17}$$

and formula (2) for combinatorial entropy assumes the form

$$S=-2\sum_{\mathbf{p}}\ [f_{\mathbf{p}}\ln f_{\mathbf{p}}+(1-f_{\mathbf{p}})\ln(1-f_{\mathbf{p}})].$$

Defining further the quasiparticle energy as

$$\varepsilon(\mathbf{p})=\frac{1}{2}\frac{\partial E}{\partial f_{\mathbf{p}}}, \tag{18}$$

we can easily obtain from the variational principle the self-consistency equation for the equilibrium distribution function $f_{\mathbf{p}}$:

$$f_{\mathbf{p}}=\{\exp\beta(\varepsilon(\mathbf{p})-\mu)+1\}^{-1}. \tag{19}$$

Formula (18) as well as expressions (17) and (19) lead to the following nonlinear integral equation for $\varepsilon(\mathbf{p})$:

$$\varepsilon(\mathbf{p})=\varepsilon_p^{(0)}+\frac{2}{V}\sum_{\mathbf{p}'}\ F(\mathbf{p},\mathbf{p}')\{\exp\beta(\varepsilon(\mathbf{p}')-\mu)+1\}^{-1}. \tag{20}$$

We shall seek the solution of this equation in the form

$$\varepsilon(\mathbf{p})=\underline{\varepsilon}(p)+\tilde{\varepsilon}(\mathbf{p}),$$

where

$$\underline{\varepsilon}(p)=\varepsilon_0(p),\quad \tilde{\varepsilon}(\mathbf{p})=\sum_{l=1}^{\infty}\ \varepsilon_l(p)P_l(\cos\theta),$$

and

$$\underline{\varepsilon}(p)=\frac{1}{4\pi}\int dO\varepsilon(\mathbf{p}),\quad \int dO\tilde{\varepsilon}(\mathbf{p})=0.$$

Since $\tilde{\varepsilon}=0$ above the phase-transition point $T>T_c$ (T_c is the critical temperature), the value of $\tilde{\varepsilon}$ is smaller than $\underline{\varepsilon}(p)$ near the critical point. Averaging Eq. (20) over angles, we obtain

$$\underline{\varepsilon}(p)=\varepsilon_p^{(0)}+\frac{2}{V}\sum_{\mathbf{p}'}\ F_0(p,p')\{\exp\beta(\underline{\varepsilon}'+\tilde{\varepsilon}'-\mu)+1\}_0^{-1}$$

(the index ''0'' in this formula indicates the zeroth harmonic in the expansion in the Legendre polynomials), where the following notation has been introduced:

$$\underline{\varepsilon}'\equiv\underline{\varepsilon}(p');\quad \tilde{\varepsilon}'\equiv\tilde{\varepsilon}(\mathbf{p}');$$

$$F(\mathbf{p},\mathbf{p}')=\sum_{l=0}^{\infty}\ F_l(p,p')P_l(\cos\theta).$$

Expanding the distribution function $f(\underline{\varepsilon}'+\tilde{\varepsilon}')=\{\exp\beta(\varepsilon'+\tilde{\varepsilon}'-\mu)+1\}^{-1}$ into a power series in $\tilde{\varepsilon}'$, we obtain

$$\underline{\varepsilon}(p)=\varepsilon_p^{(0)}+\frac{2}{V}\sum_{\mathbf{p}'}\ F_0(p,p')\times\left(f(\underline{\varepsilon}')+\sum_{n=1}^{\infty}\frac{1}{n!}\frac{\partial^n f(\underline{\varepsilon}')}{\partial\underline{\varepsilon}'^n}(\tilde{\varepsilon}'^n)_0\right). \tag{21}$$

Separating the lth harmonic in the Legendre polynomials in Eq. (20) and using the addition theorem for the Legendre polynomials, we obtain for $l\neq 0$

$$(2l+1)\tilde{\varepsilon}_l(p)=\frac{2}{V}\sum_{\mathbf{p}'}\ F_l(p,p')\sum_{n=1}^{\infty}\frac{1}{n!}\frac{\partial^n f(\underline{\varepsilon}')}{\partial\underline{\varepsilon}'^n}(\tilde{\varepsilon}'^n)_l$$

$$=\frac{2}{V}\sum_{\mathbf{p}'}\ F_l(p,p')\{f(\underline{\varepsilon}'+\tilde{\varepsilon}')-f(\underline{\varepsilon}')\}_l, \tag{22}$$

where $\tilde{\varepsilon}_l(p)\equiv[\tilde{\varepsilon}(\mathbf{p})]_l$ and $f(\underline{\varepsilon}')=\{\exp\beta(\underline{\varepsilon}'-\mu)+1\}^{-1}$. We assume that the functions $F_l(p,p')$ vary slowly in p and p'. In this case, according to Eq. (22), the quantity $\tilde{\varepsilon}_l(p)$ also varies slowly with p. Since the derivatives $\partial^n f(\underline{\varepsilon}')/\partial\underline{\varepsilon}'^n$ differ from zero at $T\ll\varepsilon_F$ only for $\underline{\varepsilon}'\approx\varepsilon_F$, we can neglect the derivatives of the quantities $F_l(p,p')$ and $\tilde{\varepsilon}_l(p')$ with respect to p' and obtain

$$(2l+1)\tilde{\varepsilon}_l(p)=\frac{2}{V}F_l(p,p_F)\sum_{\mathbf{p}'}\ \{f(\underline{\varepsilon}'+\tilde{\varepsilon}')-f(\underline{\varepsilon}')\}_l. \tag{23}$$

In contrast to (22), the quantity $\tilde{\varepsilon}'$ in this expression is defined as $\tilde{\varepsilon}'=\tilde{\varepsilon}(\mathbf{p}')_{p'=p_F}$. It follows from (23) that the order parameter $\tilde{\varepsilon}_l\equiv\tilde{\varepsilon}_l(p_F)$ satisfies the equation

$$(2l+1)\tilde{\varepsilon}_l=\frac{2}{V}F_l\sum_{\mathbf{p}'}\ \{f(\underline{\varepsilon}'+\tilde{\varepsilon}')-f(\underline{\varepsilon}')\}_l, \tag{24}$$

where

$$\tilde{\varepsilon}_l(p)=\frac{F_l(p,p_F)}{F_l(p_F,p_F)}\tilde{\varepsilon}_l, \tag{24a}$$

and $F_l=F_l(p_F,p_F)$. Introducing the function

$$n(\beta,\mu)=\frac{1}{V}\sum_{\mathbf{p}'}\ f(\underline{\varepsilon}'), \tag{25}$$

we write Eq. (24) in the form

$$(2l+1)\tilde{\varepsilon}_l=2F_l n(\beta,\mu-\tilde{\varepsilon})_l;\quad l\neq 0. \tag{26}$$

The solution of this equation will be sought in the form $\tilde{\varepsilon}_l=\tilde{\varepsilon}_l^{(0)}+\varepsilon_l^{(1)}+\ldots$, where $\tilde{\varepsilon}_l^{(0)}=\tilde{\varepsilon}_{l_0}\delta_{ll_0}$. In this case, in the main approximation we have

$$(2l_0+1)\tilde{\varepsilon}_{l_0}=-2F_{l_0}\frac{\partial n(\beta_c,\mu)}{\partial\mu}\tilde{\varepsilon}_{l_0}^{(0)}.$$

Thus, the equation for determining the phase-transition temperature T_c as a function of l_0 ($T_c=T_c(l_0)$) has the form

$$(2l_0+1)=-2F_{l_0}\frac{\partial n(\beta_c,\mu)}{\partial\mu}. \tag{27}$$

Retaining higher-order terms in $\tilde{\varepsilon}_{l_0}$ in the expansion on the right-hand side of Eq. (26) as well as Eq. (27), we write (26) for $l=l_0$ in the form

$$-\frac{\partial^2 n(\beta_c,\mu)}{\partial\beta_c\partial\mu}(\beta-\beta_c)\tilde{\varepsilon}_{l_0}+\frac{1}{2}\frac{\partial^2 n(\beta_c,\mu)}{\partial\mu^2}\times(\tilde{\varepsilon}^2)_{l_0}-\frac{1}{6}\frac{\partial^3 n(\beta_c,\mu)}{\partial\mu^3}(\tilde{\varepsilon}^3)_{l_0}=0. \tag{28}$$

It can easily be seen that in order to determine $(\tilde{\varepsilon}^2)_{l_0}$, we must take Eq. (26) for $l\neq l_0$ into account along with (28):

$$(2l+1)\tilde{\varepsilon}_l=2F_l\left(-\frac{\partial n(\beta_c,\mu)}{\partial\mu}\tilde{\varepsilon}_l-\frac{\partial^2 n(\beta_c,\mu)}{\partial\beta_c\partial\mu}\times(\beta-\beta_c)\tilde{\varepsilon}_l+\frac{1}{2}\frac{\partial^2 n(\beta_c,\mu)}{\partial\mu^2}(\tilde{\varepsilon}^2)_l\right),\quad l\neq l_0,$$

from which (neglecting the second term on the right-hand side) we obtain

$$\tilde{\varepsilon}_l=\frac{F_l}{2l+1+2F_l(\partial n/\partial\mu)}\frac{\partial^2 n}{\partial\mu^2}(\tilde{\varepsilon}^2)_l+\ldots,l\neq 0,\quad l_0. \tag{29}$$

Thus, along with Eq. (27) for the phase-transition temperature, we have Eqs. (28) and (29) for determining the temperature dependence of the order parameter $\tilde{\varepsilon}_{l_0}$.

Let us now determine the phase-transition point. For this purpose, we present the quantity $n(\beta,\mu)$ [see (25)] in the form

$$n(\beta,\mu)=\frac{1}{2}\int_0^\infty d\varepsilon\,\nu(\varepsilon)\{\exp\beta(\varepsilon-\mu)+1\}^{-1},$$

where

$$\nu(\varepsilon)=\frac{2}{(2\pi)^3}\int d^3p'\,\delta(\varepsilon-\underline{\varepsilon}') \tag{30}$$

is the density of states. Noting further that at $T\ll\mu$ the expansion

$$n(\beta,\mu)=\frac{1}{2}\left(\int_0^\mu\nu(\varepsilon)d\varepsilon+\frac{\pi^2}{6}\beta^{-2}\nu'(\mu)+\ldots\right), \tag{31}$$

holds, we obtain

$$\frac{\partial n(\beta_c,\mu)}{\partial\mu}=\frac{1}{2}\nu(\mu)+\frac{\pi^2}{12}\beta_c^{-2}\nu''(\mu).$$

Consequently, Eq. (27) assumes the form

$$2l_0+1=-F_{l_0}\left(\nu(\mu)+\frac{\pi^2}{6}\beta_c^{-2}\nu''(\mu)\right),$$

whence

$$\beta_c^{-2}\equiv T_c^2=-\frac{6}{\pi^2}\frac{2l_0+1}{\nu''(\mu)F_{l_0}}\left(1+\nu(\mu)\frac{F_{l_0}}{2l_0+1}\right).$$

Since the condition $T_c\ll\mu$ in the vicinity of the phase-transition point, we have

$$T_c^2=\frac{6}{\pi^2}\frac{\nu(\mu)}{\nu''(\mu)}\left(1+\nu(\mu)\frac{F_{l_0}}{2l_0+1}\right). \tag{32}$$

This approximation is valid due to the fact that $\nu(\mu)/\nu''(\mu)\sim\mu^2$, and hence $\nu(\mu)[F_{l_0}/2l_0+1)]\cong-1$ at $T_c\ll\mu$. Noting further that $T_c^2>0$ and $\nu(\mu)>0$, $\nu''(\mu)<0$, we find that

$$1+\nu(\mu)\frac{F_{l_0}}{2l_0+1}<0. \tag{33}$$

Condition (33) shows that the Pomeranchuk criterion (10) for the amplitude of a potential interaction does not hold for the harmonic l_0. Consequently, when condition (33) is satisfied, in the temperature range $T<T_c$ we are dealing with a new phase differing from the normal phase.

In order to determine the temperature dependence of the order parameter, we return to Eqs. (28) and (29). We consider separately the cases of even and odd l_0. Presenting for this purpose the order parameter $\tilde{\varepsilon}$ in the form

$$\tilde{\varepsilon}=\sum_{l\neq l_0}\tilde{\varepsilon}_l P_l+\tilde{\varepsilon}_{l_0}P_{l_0}, \tag{34}$$

we can easily see that $(\tilde{\varepsilon}^2)_{l_0}\approx(\tilde{\varepsilon}_{l_0}^2P_{l_0}^2)_{l_0}=\tilde{\varepsilon}_{l_0}^2(P_{l_0}^2)_{l_0}$ for even l_0. Consequently, it follows immediately from Eq. (28) that

$$\tilde{\varepsilon}_{l_0}=\frac{\partial^2 n(\beta_c,\mu)}{\partial\beta_c\partial\mu}(\beta-\beta_c)\frac{2}{[\partial^2 n(\beta_c,\mu)/\partial\mu^2](P_{l_0}^2)_{l_0}}$$

or, taking into account expansion (31),

$$\tilde{\varepsilon}_{l_0}=B(l_0)\left(1-\frac{T}{T_c}\right),\quad B(l_0)=-\frac{2}{3}\pi^2T_c^2\frac{\nu''(\mu)}{\nu'(\mu)(P_{l_0}^2)_{l_0}}. \tag{35}$$

Substituting (35) into (24a), we obtain in the main approximation the expression determining the temperature dependence of the order parameter $\tilde{\varepsilon}(\mathbf{p},T)$:

$$\tilde{\varepsilon}(\mathbf{p})=\frac{F_{l_0}(p,p_F)}{F_{l_0}(p_F,p_F)}B(l_0)\left(1-\frac{T}{T_c}\right)P_{l_0}(\cos\theta). \tag{36}$$

This formula is valid for even l_0.

In the case of odd l_0, we obtain, using (34),

$$(\tilde{\varepsilon}^2)_{l_0}\approx 2\tilde{\varepsilon}_{l_0}\sum_{l\neq l_0}\tilde{\varepsilon}_l(P_{l_0}P_l)_{l_0}, \tag{37}$$

[$(\tilde{\varepsilon}_{l_0}^2P_{l_0}^2)_{l_0}=0$ in view of the odd nature of the function $P_{l_0}^3$ for odd l_0]. Noting also that $(\tilde{\varepsilon}^2)_l=\tilde{\varepsilon}_{l_0}^2(P_{l_0}^2)_l$, we write (37) taking into account (29) in the form

$$(\tilde{\varepsilon}^2)_{l_0}=2\tilde{\varepsilon}_{l_0}^3\frac{\partial^2 n(\beta_c,\mu)}{\partial\mu^2}\times\sum_{l\neq l_0}\frac{F_l}{2l+1+2F_l[\partial n(\beta_c,\mu)/\partial\mu]}(P_{l_0}^2)_l(P_lP_{l_0})_{l_0}. \tag{38}$$

Using the fact that

$$(\tilde{\varepsilon}^3)_{l_0}=\tilde{\varepsilon}_{l_0}^3(P_{l_0}^3)_{l_0},\quad (P_{l_0}^2)_l(P_lP_{l_0})_{l_0}=\frac{2l_0+1}{2l+1}[(P_{l_0}^2)_l]^2,$$

we write Eq. (28) in the form

$$\frac{\partial^2 n(\beta_c,\mu)}{\partial\beta_c\partial\mu}(\beta-\beta_c)=\tilde{\varepsilon}_{l_0}^2\left\{\left(\frac{\partial^2 n(\beta_c,\mu)}{\partial\mu^2}\right)^2\sum_{l\neq l_0}\frac{F_l}{2l+1+2F_l[\partial n(\beta_c,\mu)/\partial\mu]}\times\frac{2l_0+1}{2l+1}[(P_{l_0}^2)_l]^2-\frac{1}{6}\frac{\partial^3 n(\beta_c,\mu)}{\partial\mu^3}(P_{l_0}^3)_{l_0}\right\}\right\}, \tag{39}$$

which readily leads, on account of the low-temperature expansion (31), to the following expression for the quantity $\tilde{\varepsilon}_{l_0}$ for odd l_0:

$$\tilde{\varepsilon}_{l_0}=A(l_0)\sqrt{1-T/T_c}, \tag{40}$$

where

$$A(l_0)=\left(\frac{2\pi^2T_c^2\nu''(\mu)}{\nu''(\mu)(P_{l_0}^3)_{l_0}-3\nu'(\mu)^2(2l_0+1)\Sigma_{l\neq l_0}\dfrac{F_l}{2l+1+F_l\nu(\mu)}\dfrac{[(P_{l_0}^2)_l]^2}{2l+1}}\right)^{1/2}. \tag{41}$$

Finally, substituting (40) into (24a), we obtain in the main approximation

$$\tilde{\varepsilon}(\mathbf{p})=\frac{F_{l_0}(p,p_F)}{F_{l_0}(p_F,p_F)}A(l_0)\sqrt{1-T/T_c}P_{l_0}(\cos\theta). \tag{42}$$

Thus, we see that in contrast to the case of even l_0, we have a nonanalytic temperature dependence of the order parameter for odd l_0 (see (42)), which is typical of the Landau theory for second-order phase transitions.

3. FLUXES OF ADDITIVE INTEGRALS OF MOTION NEAR THE PHASE-TRANSITION POINT

In this section, we consider the variation of various physical quantities (in the approximation linear in $[1-(T/T_c)]^{1/2}$) in the phase transition under investigation. It can easily be seen that scalar quantities such as heat capacity, thermodynamic potential, energy and entropy density do not change under the phase transition. On the contrary, vector and tensor quantities such as flux densities of the number of particles, energy, and momentum density may change as a result of phase transition in this approximation. In order to verify this, let us construct formulas for the flux densities of number of particles, momentum and energy.

Proceeding from the kinetic equation for the one-particle density matrix $\hat{f}$ in the approximation $\omega\tau\gg1$ (ω^{-1} is the characteristic time of variation of f and τ the relaxation time), i.e.,

$$i\frac{\partial\hat{f}}{\partial t}=[\hat{\varepsilon}(\hat{f}),\hat{f}], \tag{43}$$

we can derive the expressions for the flux densities of additive integrals of motion (see Ref. 5 in this connection).

Using this kinetic equation, we can easily see that the time derivative of the density of a physical quantity $a(x,\hat{f})=\mathrm{tr}\,\hat{f}a(x)$ is defined by the formula

$$\frac{\partial a(x,\hat{f})}{\partial t}=-\frac{\partial a_k(x,\hat{f})}{\partial x_k}+i\,\mathrm{tr}\,\hat{f}[\hat{\varepsilon}(x,\hat{f}),\hat{A}], \tag{44}$$

where

$$\hat{a}_k(x)=i\int d^3x'x_k'\int_0^1 d\xi[\hat{\varepsilon}\{x-(1-\xi)x';\hat{f}\},\hat{a}(x+\xi x')];$$

$$\hat{A}=\int d^3x\hat{a}(x);$$

$\varepsilon_{12}(x,\hat{f})=\partial\varepsilon(x)/\partial f_{21}$ is the energy density of a quasiparticle, $\mathcal{E}(x)$ the energy density of the Fermi liquid, $\int d^3x\varepsilon(x,\hat{f})=E(\hat{f})$. Formula (44) follows directly from the kinetic equation (43) according to which

$$\frac{\partial a(x,\hat{f})}{\partial t}=i\mathrm{tr}\,\hat{f}[\hat{\varepsilon}(\hat{f}),\hat{a}(x)],$$

and from the obvious relation

$$i[\hat{\varepsilon}(\hat{f}),\hat{a}(x)]=i[\hat{\varepsilon}(x,\hat{f}),\hat{A}]-\frac{\partial\hat{a}_k(x)}{\partial x_k}.$$

Putting in this formula $\hat{a}(x)=\hat{\rho}(x)$, where $\hat{\rho}(x)=\delta(x-\hat{x})$ ($\hat{x}$ is the coordinate operator), and noting that $\hat{A}\equiv\int\hat{\rho}(x)d^3x=1$, we obtain

$$\frac{\partial\rho(x,\hat{f})}{\partial t}=-\frac{\partial j_k(x,\hat{f})}{\partial x_k}, \tag{45}$$

where

$$j_k(x,\hat{f}) = i\int d^3x' x'_k \,\mathrm{tr}\int_0^1 d\xi \hat{f}[\hat{\varepsilon}\{x-(1-\xi)x';\hat{f}\},$$

$$\hat{\rho}(x+\xi x')]. \tag{46}$$

In order to derive the expression for the momentum flux density $\pi_i(x)$, we note that the energy density $\mathcal{E}(x,\hat{f})$ of the Fermi liquid satisfies the property of invariance to translations over the vector y:

$$\varepsilon(x+y, e^{i\hat{p}y}\hat{f}e^{-i\hat{p}y}) = \varepsilon(x,\hat{f})$$

($\hat{p}$ is the momentum operator). Differentiating this expression with respect to y and putting $y=0$, we obtain

$$\frac{\partial\varepsilon(x,\hat{f})}{\partial x_k} = \mathrm{tr}\,\hat{f}[\hat{\varepsilon}(x,\hat{f}),\hat{p}_k]. \tag{47}$$

Returning to formulas (44) and assuming that in these formulas

$$\hat{a}(x) = \hat{\pi}_i(x) \equiv \tfrac{1}{2}\{\hat{p}_i, \delta(x-\hat{x})\},$$

and also using (47), we obtain

$$\frac{\partial\pi_i(x\hat{f})}{\partial t} = -\frac{\partial t_{ik}(x,\hat{f})}{\partial x_k}, \tag{48}$$

where the momentum flux density $t_{ik}(x,\hat{f})$ has the form

$$t_{ik}(x\hat{f}) = -\varepsilon\delta_{ik} + i\int d^3x' x'_k \,\mathrm{tr}\int_0^1 d\xi\hat{f}$$

$$\times[\hat{\varepsilon}\{x-(1-\xi)x';\hat{f}\}, \hat{\pi}_i(x+\xi x')]. \tag{49}$$

Finally, let us formulate the differential law of energy conservation. Noting that

$$\frac{\partial\varepsilon(x,\hat{f})}{\partial f_{12}} = \varepsilon_{21}(x,\hat{f}),$$

and using the kinetic equation (43), we obtain

$$\frac{\partial\varepsilon(x,\hat{f})}{\partial t} = \mathrm{tr}\,\hat{f}[\hat{\varepsilon}(\hat{f}),\hat{\varepsilon}(x,\hat{f})].$$

Assuming now that $\hat{a}(x) = \hat{\varepsilon}(x,\hat{f})$ in formulas (44), we obtain

$$\frac{\partial\varepsilon(x,\hat{f})}{\partial t} = -\frac{\partial q_k(x,\hat{f})}{\partial x_k}, \tag{50}$$

where

$$q_k(x,\hat{f}) = \frac{i}{2}\int d^3x' x'_k \,\mathrm{tr}\int_0^1 d\xi\hat{f}[\hat{\varepsilon}\{x$$

$$-(1-\xi)x';\hat{f}\},\hat{\varepsilon}(x+\xi x';\hat{f})]. \tag{51}$$

For spatially homogeneous states ($[\hat{f},\hat{p}_k]=0$), formulas (46), (49), and (51) are simplified and assume the following graphic form:

$$j_k = \frac{2}{V}\sum_{\mathbf{p}} f_{\mathbf{p}}\frac{\partial\varepsilon_{\mathbf{p}}}{\partial\mathbf{p}_k}, \tag{52}$$

$$q_k = \frac{2}{V}\sum_{\mathbf{p}} f_{\mathbf{p}}\varepsilon_{\mathbf{p}}\frac{\partial\varepsilon_{\mathbf{p}}}{\partial p_k}, \tag{53}$$

$$t_{ik} = -\left(\varepsilon - \frac{2}{V}\sum_{\mathbf{p}} f_{\mathbf{p}}\varepsilon_{\mathbf{p}}\right)\delta_{ik} + \frac{2}{V}\sum_{\mathbf{p}} f_{\mathbf{p}}p_i\frac{\partial\varepsilon_{\mathbf{p}}}{\partial p_k}, \tag{54}$$

where $\varepsilon_{\mathbf{p}}$ is the quasiparticle energy.

If the distribution function $f_{\mathbf{p}}$ is an equilibrium function with the drift velocity **u**, i.e.,

$$f_{\mathbf{p}} = \{\exp\beta(\varepsilon_{\mathbf{p}} - \mathbf{p}\cdot\mathbf{u} - \mu) + 1\}^{-1},$$

these formulas assume the form

$$j_k = u_k\frac{2}{V}\sum_{\mathbf{p}} f_{\mathbf{p}},$$

$$q_k = u_k\frac{2}{V}\sum_{\mathbf{p}}\left(f_{\mathbf{p}}\varepsilon_{\mathbf{p}} - \frac{1}{\beta}\ln(1-f_{\mathbf{p}})\right),$$

$$t_{ik} = u_k\pi_i + \delta_{ik}\left(-\frac{1}{\beta}\right)\frac{1}{V}\left(2\sum_{\mathbf{p}}\ln(1-f_{\mathbf{p}})\right.$$

$$\left.+\beta\varepsilon V - 2\beta\sum_{\mathbf{p}} f_{\mathbf{p}}\varepsilon_{\mathbf{p}}\right).$$

Using formula (3), we can easily see that the thermodynamic potential density ω is defined as

$$\omega = \frac{1}{V}\left(2\sum_{\mathbf{p}}\ln(1-f_{\mathbf{p}}) + \beta\varepsilon V - 2\beta\sum_{\mathbf{p}} f_{\mathbf{p}}\varepsilon_{\mathbf{p}}\right)$$

and hence the formulas for t_{ik}, q_k, and j_k can be written in the form

$$t_{ik} = u_k\pi_i - \frac{\omega}{\beta}\delta_{ik}, \quad q_k = u_k(\varepsilon - \omega/\beta), \quad j_k = nu_k. \tag{55}$$

Consequently, the quantity $-(\omega/\beta)\equiv p$ can be interpreted as pressure, while the quantity $w = -(\omega/\beta) + \mathcal{E}$ can be regarded as the enthalpy density (n is the number density of fermions).

Let us now determine the density of the momentum emerging as a result of phase transition. Since **p** is the momentum of an individual particle, the momentum density of the system is defined by the formula

$$\boldsymbol{\pi} = \frac{2}{V}\sum_{\mathbf{p}}\mathbf{p}f_{\mathbf{p}}$$

or, noting that $f(\underline{\varepsilon}+\tilde{\varepsilon}) = f(\underline{\varepsilon}) + (\partial f/\partial\underline{\varepsilon})\tilde{\varepsilon}$, we have

$$\boldsymbol{\pi} = \frac{2}{(2\pi)^3}\int d^3p\,\mathbf{p}\frac{\partial f}{\partial\underline{\varepsilon}}\tilde{\varepsilon}(\mathbf{p}).$$

Going over to integration with respect to angles and ε and noting that $df/d\varepsilon = -\delta(\varepsilon-\mu)$, we obtain

$$\pi_i = -\frac{2}{(2\pi)^3}\int dO\left(\frac{p^2}{v}p_i\tilde{\varepsilon}(\mathbf{p})\right)_{p_F}, \quad v = \frac{\partial\varepsilon}{\partial p}.$$

Since

$$\nu(\mu) = \frac{2}{(2\pi)^3}\int d^3p\,\delta(\underline{\varepsilon}-\mu) = \frac{1}{\pi^2}\left(\frac{p_F^2}{v_F}\right),$$

we have

$$\pi_z = -\frac{\nu(\mu)}{3} p_F A(1) \sqrt{1-T/T_c}\,\delta_{l_0,1}, \quad \pi_x = \pi_y = 0, \tag{56}$$

where

$$A(1) = \frac{10\pi^2 T_c^2 \nu''(\mu)}{3\nu''(\mu) - \nu'^2(\mu)[F_2/\{5+F_2\nu(\mu)\}]}, \quad F_2 \equiv F|_{l=2}.$$

Thus, a nonzero momentum density appears only for $l_0 = 1$.

Let us now find expressions for the densities of fluxes j_i, q_k, and t_{ik} emerging as a result of the phase transition. Since the drift velocity of particle does not appear in the expression for the fermion distribution function in the new phase, these fluxes j_i and q_i vanish in accordance with (55).

However, momentum must be conserved in the phase transition. If the momentum of the system in the normal state was zero, the momentum after the phase transition must also be zero. Consequently, the distribution function after the phase transition must have the form

$$f = \{\exp\beta(\underline{\varepsilon} + \tilde{\varepsilon} - \mathbf{p}\cdot\mathbf{u} - \mu) + 1\}^{-1}$$

$$\approx \{\exp\beta(\underline{\varepsilon} + \tilde{\varepsilon} - \mu) + 1\}^{-1} + \frac{\partial f(\underline{\varepsilon})}{\partial \underline{\varepsilon}}(-\mathbf{p}\cdot\mathbf{u})$$

($\mathbf{u}$ is the drift velocity of the system as a whole). As a result, the momentum density after the phase transition is given by

$$\boldsymbol{\pi}' = \boldsymbol{\pi} - \frac{2}{V}\sum_{\mathbf{p}} \frac{df(\varepsilon)}{d\varepsilon}(\mathbf{p}\cdot\mathbf{u})\mathbf{p}.$$

It was noted above that the momentum must vanish after the phase transition ($\boldsymbol{\pi}' = 0$), i.e., the velocity of the Fermi system will be determined from the relation

$$\frac{2}{V}\sum_{\mathbf{p}} \frac{df(\varepsilon)}{d\varepsilon}(\mathbf{p}\cdot\mathbf{u})\mathbf{p} = \boldsymbol{\pi},$$

where the value of $\boldsymbol{\pi}$ is defined by (56). Going over from summation to integration and evaluating the obtained integral, we obtain the following expression for the velocity of the Fermi liquid:

$$u_z = -\frac{3}{\nu(\mu)p_F^2}\pi_z = -\frac{A(1)}{2p_F}\sqrt{1-T/T_0}, \tag{57}$$

$$u_x = u_y = 0.$$

Thus, the fluxes j_i, q_k, and t_{ik} are defined by formulas (55) in which the drift velocity u is replaced by (57) (since $\pi = 0$ in the absence of a phase transition, the density of the momentum flux T_{ik} also vanishes).

If fermions are electrons of a metal, they interact with the crystal lattice, and the momentum can be partially transferred to the latter. The effect considered above is similar to the Einstein–de Haas effect, in which the body starts rotating as a result of magnetization in view of the angular momentum conservation law due to the fact that electrons acquire an additional angular momentum.

In conclusion, we formulate some considerations concerning physical objects in which the phase transition considered by us here can take place. An analysis of experimental data on the measurements of Landau amplitudes for ^{3}He (see, for example, Ref. 6) leads to the conclusion that the phase transition described above is hardly possible in ^{3}He. The available experimental data concerning the measurements of the parameters of an electron liquid in various metals (see, for example, Refs. 7, 8 in this connection) suggests that such systems are most suitable for observing such phase transitions.

In all probability, the phase transition in the Fermi liquid under investigation can be observed in some alloys.[9] We mean the experimental observation of ''hopping'' of samples prepared from such alloys at a certain temperature during cooling. This effect corresponds qualitatively to the conclusion drawn by us here concerning the average momentum acquired by fermions as a result of the phase transition, which is transferred to the crystal lattice and causes a directional movement of the sample. However, additional experiments are required to confirm this assumption. We could not find in the literature any experimental results of measurements of parameters (Landau amplitudes) of an electron liquid in such materials which would confirm or refute the above assumption.

This research was carried out under the financial support from the Ukrainian State Foundation of Fundamental Studies (grant No. 24/378).

*E-mail: slusarenko@kipt.kharkov.ua

[1] L. D. Landau, Zh. Éksp. Teor. Fiz. **30**, 1058 (1956) [Sov. Phys. JETP **3**, 920 (1956)]; Zh. Éksp. Teor. Fiz. **32**, 59 (1957) [Sov. Phys. JETP **5**, 101 (1957)].
[2] V. P. Silin, Zh. Éksp. Teor. Fiz. **33**, 495 (1957) [Sov. Phys. JETP **6**, 387 (1957)]; Zh. Éksp. Teor. Fiz. **35**, 1243 (1958) [Sov. Phys. JETP **8**, 870 (1958)].
[3] I. Ya. Pomeranchuk, Zh. Éksp. Teor. Fiz. **35**, 524 (1958) [Sov. Phys. JETP **8**, 361 (1958)].
[4] I. A. Akhiezer, Ukr. Fiz. Zh. **25**, 177 (1980).
[5] A. I. Akhiezer and S. V. Peletminsky, *Methods of Statistical Physics* [in Russian], Nauka, Moscow (1977).
[6] W. P. Halperin and L. P. Pitaevskii (Eds.), *Helium Three*, North-Holland, Amsterdam, Oxford, New York, Tokyo (1990).
[7] P. Platzman and P. Wolff, *Waves and Interactions in Solid State Plasmas*, Academic Press, New York (1973).
[8] E. V. Bezuglyi, N. G. Burma, A. Yu. Deineka, and V. D. Fil, Fiz. Nizk. Temp. **19**, 667 (1993) [Low Temp. Phys. **19**, 477 (1993)].
[9] V. S. Boiko, R. I. Garber, and A. M. Kosevich, *Reversible Ductility of Crystals* [in Russian], Nauka, Moscow (1991).

Translated by R. S. Wadhwa

SUPERCONDUCTIVITY, HIGH-TEMPERATURE SUPERCONDUCTIVITY

Critical current density and granularity in crystals of K_3C_{60} fulleride

V. A. Buntar

*Atominstitut der Österreichischen Universitäten, A-1020 Vienna, Austria**

A. G. Buntar

Vinnitsa State Technical University, 286021 Vinnitsa, Ukraine
(Submitted August 3, 1998; revised October 20, 1998)
Fiz. Nizk. Temp. **25**, 222–229 (March 1999)

The temperature dependence of the critical current density $J_c(T)$ in superconducting fulleride K_3C_{60} crystals is investigated on the basis of magnetization measurements in these materials. According to ac susceptibility data, the best crystals do not exhibit granularity for supercurrent flows, and can be regarded as single crystals from this point of view. The obtained results on J_c in K_3C_{60} are compared with those for other crystalline and powder-type compounds $A_xB_yC_{60}$. Possible granularity of the crystals and its influence on J_c are discussed in detail. The irreversibility line for a K_3C_{60} single crystal is also determined. [S1063-777X(99)00203-0]

1. INTRODUCTION

After the discovery of superconductivity in fullerenes doped by alkali metals,[1] considerable attention has been paid to the analysis of the critical current in these materials. The critical current density J_c is one of the most important parameters for applications of superconductors in engineering. The measurement of J_c from the transport characteristics of current is a difficult problem as such since such measurements require high current densities. Besides, considerable difficulties are encountered in preparing high-quality low-resistance junctions on brittle materials as in fullerene superconductors (FS) and earlier, in HTSC materials. However, the most serious obstacle in transport measurements is the instability of superconductivity in FS when the material comes in contact with oxygen. For this reason, FS samples are usually sealed in glass or quartz capsules, which hampers the preparation of electric junctions. Thus, the measurements of magnetic susceptibility is one of the most important method of studying the critical current density. For this purpose, the model of critical state proposed by Bean[2] is used. According to this model, J_c is proportional to the width Δm of the hysteresis loop.

First measurements of the critical current density on FS were made on powder samples in which intergranular supercurrents played an important role. It has become possible to make measurements on high-quality monocrystalline samples having a large size. Hence, an analysis of the temperature and field dependences of the critical current density in these crystals and a comparison with the results obtained on powders are of special importance. (Here and below, ''crystals'' and ''single crystals'' are the terms applied to crystalline samples of a large size of the order of mm^3, for which the volume of the superconducting phase is smaller than or equal to 100% in contrast to powder samples which in principle are also crystalline with a grain size of the order of μm^3.)

In this paper, we describe the results of magnetic studies of J_c carried out on K_3C_{60} crystals. These results are compared with the data obtained for other $A_xB_yC_{60}$ compositions of crystalline and powder samples.

2. OBJECT AND METHOD OF INVESTIGATION

The measurements were made on two SQUID magnetometers in magnetic fields 1–8 T. The first magnetometer (commercial Quantum Design) with a sensitivity up to $10^{-10}\,A\cdot m^2$ ensured the control of the field trapped a superconducting magnet at a level not higher than 5×10^{-8} T. The same magnetometer was used for the measurement of dynamic magnetic susceptibility (ac measurements) in the frequency range from 3 Hz to 1.5 kHz and the ac magnetic field amplitude varying from 10^{-6} to 5×10^{-4} T. The second magnetometer, equipped with a superconducting magnet producing a field up to 8 T, was used for measuring hysteresis loops in the temperature range from 5 K to T_c.

The critical current density was studied on three large K_3C_{60} crystals (K1, K2, and K3 samples) whose volume was of the order of several cubic millimeters. The process of sample preparation and parameters of the samples are described in detail in Ref. 3. However, we shall mention some of these parameters here once again. For instance, the superconducting phase (x_{sc}) amounted to 100% in samples K1 and K2, while x_{sc} for the K3 sample was 25%. In this paper, we shall mainly describe the results obtained for K1 and K2 single crystals. However, some results [e.g., dynamic (ac) magnetizations and $H_{irr}(T)$] will be given for all the three samples.

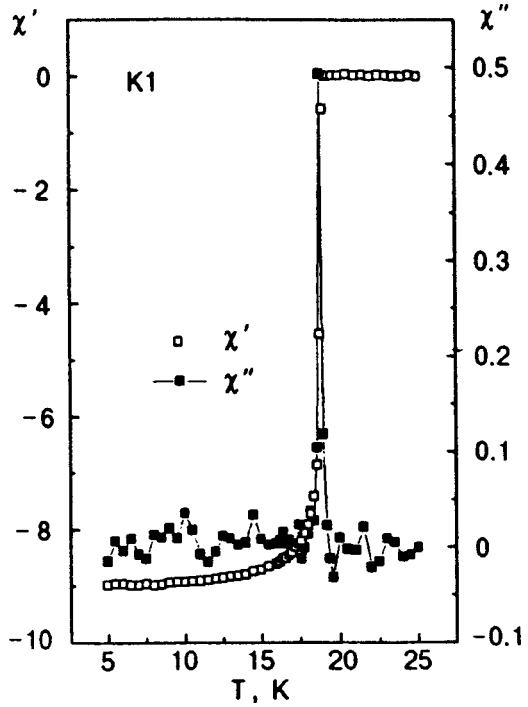

FIG. 1. Temperature dependence of dynamic magnetic susceptibility for K1 sample.

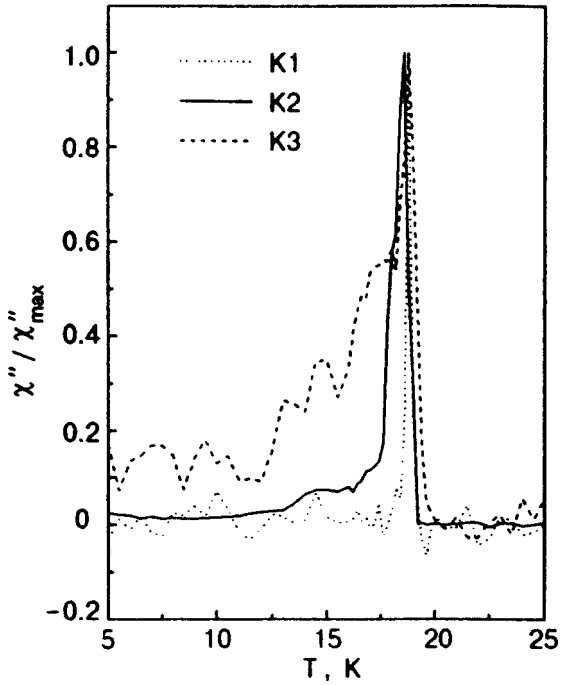

FIG. 2. Temperature dependence of the imaginary component of susceptibility.

In order to establish the presence and effect of intergranular structure, we carried out the measurements of dynamic magnetization. Such measurements were made for fullerides in several laboratories.[4–6] The presence of two clearly distinguishable peaks on the temperature dependence of the imaginary component of susceptibility[6] (χ'') indicated unambiguously the existence of inter- as well as intragranular scattering mechanisms.

Only one peak is observed in sample K1 with a 100% screening of magnetic field. Figure 1 shows the temperature dependences of the real and imaginary components of dynamic susceptibility for this sample. These dependences were measured in zero magnetic field. The peak on the $\chi''(T)$ curve lies near the critical temperature and corresponds to energy dissipation in the superconducting material. As the constant (dc) field increases, the peaks become slightly broader and shifts towards low temperatures. No other peaks are observed on the temperature dependence of χ'' for K1 in the entire experimental range of ac and dc fields. On the contrary, the $\chi''(T)$ dependence for sample K2 displays one more less clearly manifested peak near the first one and additional scattering at lower temperatures ~ 15 K.

In contrast to samples with 100% screening of the field, the temperature dependence $\chi''(T)$ obtained for sample K3 has a much more complex structure. Figure 2 shows for comparison the $\chi''(T)$ dependences for all the three samples. The sharp peak observed for K1 is also clearly seen for K3. At the same time, several other peaks corresponding to lower temperatures are also seen clearly. These peaks are associated with energy dissipation at weak interphase links. The formation of such links in K3 is undoubtedly associated with the presence of nonsuperconducting inhomogeneities (undoped C_{60} or probably K_1C_{60}).

Thus, ac measurements show that sample K1 does not display granularity for supercurrents flowing through the sample. This sample is 100% screened from a magnetic field and contains no other phases except K_3C_{60}. Nevertheless, the sample still contains a mosaic structure with a block disorientation angle of 3°. In all probability, this mosaic structure does not hamper supercurrents. In this respect, K1 sample resembles in its properties ''melt-textured'' HTSC materials also exhibiting a weak disorientation of blocks, which does not lead to granularity of the sample as a whole for supercurrents. Sample K2 possesses virtually the same characteristics as K1. However, a weak effect of granularity is still present in the sample. Sample K3 with a nonuniform stoichiometry displays a strong effect of granularity.

3. DISCUSSION OF RESULTS

Almost the entire experimental information on the temperature and field dependences of critical current density in FS was obtained from magnetic measurements. It was noted above that some peculiarities observed in FS strongly complicate the measurement of J_c from the transport characteristics of current. First, superconductivity in fullerides becomes unstable after contact with oxygen. Second, high-quality crystalline samples required for such measurements were not available until recently. Thus, magnetization measurements in a magnetic field at various temperatures used for obtaining information on J_c on the basis of the model of critical state[2] were the only possible experimental method for studying the critical current density in these materials. The simplest version of Bean's model is based on the assumption that the critical current density is independent on the field, and hence the density distribution of the field penetrating the sample decreases linearly from the surface to the center.

TABLE I. Critical current density and parameters ΔM and m for K_3C_{60} and Rb_3C_{60} samples.

Compound	R, mm	J_c, A/m^2	ΔM, 10^3 A/m: 5 K, 0.5 T	ΔM, 10^3 A/m: 5 K, 0.1 T	References	m from (2)
K_3C_{60}	10^{-3}	10^9	0.7	1.97	6	1.47 [25]
	10^{-3}	$1.2\cdot10^9$	–	–	23	1.5 [3]
	10^{-3}	-10^9	−0.7	–	24	–
	$10^{-3}-3\cdot10^{-1}$	–	3.4	7.63	12	–
	1	10^7	14.6	25.33	11	–
	1	$6\cdot10^7$	9.3	25	K1*	–
	1	$4\cdot10^7$	7.1	18.5	K2*	–
Rb_3C_{60}	10^{-3}	$4\cdot10^{10}$	0.68	0.97	13	1.59 [25]
	10^{-3}	$1.5\cdot10^{10}$	0.23	0.32	8	1.8-2 [26]
	10^{-3}	$2\cdot10^{10}$	–	–	10	–
	10^{-3}	-10^{10}	–	–	24	2.0 [27]
	$10^{-3}-3\cdot10^{-1}$	–	1.72	3.71	12	–
	1	-10^7	19.7	–	11	–
	1	$6\cdot10^8$	21.9	–	14	–

Note: Asterisks mark our results.

With increasing external magnetic field, magnetic vortices penetrate the samples more and more deeply until they approach its center at a certain value of the magnetic field H^*. On the magnetization curve, H^* can be determined as the field at which the magnetization attains its peak value. A further increase in the field leaves the magnetization unchanged. As the applied field decreases, the sign of the distribution density gradient is reversed. This model obviously leads to a dependence of magnetization on the size and geometry of the sample. The value of J_c can be determined from the experimental curve obtained from dc magnetization on the basis of the equation[2]

$$J_c = A(M_+ - M_-)/R, \tag{1}$$

where A is the coefficient determined by the sample geometry,[2,7] M_+ and M_- are the magnetizations measured for the same value of magnetic field during its increase and decrease, respectively, and R is the sample radius. In Refs. 8 and 9, the value of J_c was determined simultaneously from dc and ac measurements, and good agreement of the results was observed. This indicates that the critical state model can be used for FS.

Table I shows some values of critical current density obtained for fullerene superconductors in the powder and crystalline form with a crystal size up to several mm[3]. These results were obtained from magnetic measurements and demonstrate a considerable hysteresis of magnetization up to high values of magnetic field. This indicates a strong pinning of vortex filaments, and hence high values of critical current density. For example, the value of J_c in Rb_3C_{60}[10] at $T=23\,\mathrm{K}=0.82T_c$ in a magnetic field of 0.5 T is still quite large (5×10^8 A/m^2).

When the critical current density is calculated in powders, the sample is treated as an aggregate of uncoupled superconducting spheres. The averaged diameter of these spheres is equal to the average diameter of a grain in the sample. In this case, the error in determining the absolute value of J_c can be quite large, which is due to, first, a not very accurate value of the geometrical coefficient A for grains of a complex shape, and second, the indeterminacy in the value of R. The second factor is more significant. The problem of calculation of the critical current density for crystalline samples is not less complicated than the problem for powders, especially for sample with the superconducting fraction x_{sc} smaller than 100%. For such samples, we must make certain assumptions concerning their microscopic structure in order to obtain the values of R.

Irons *et al.*[11] were the first to study the critical current density in large crystalline samples. The value of J_c obtained in these experiments was of the order of 10^6 A/m^2, which is much smaller than that observed for powder samples ($\sim10^9$ A/m^2). Boss *et al.*[12] studied the dependence of the critical current density on the grain size in the sample. In these experiments, the average radius of grains was 1, 3, 10, 30, 100, and 300 μm in different samples. Boss *et al.*, established that the value of J_c is inversely proportional to the grain size (see Table I in Ref. 12). In our opinion, the ''decrease'' in the critical current density upon an increase in the average grain size observed by Boss *et al.*[12] is due to an incorrect value of R used for calculating J_c on the basis of formula (1). Otherwise, the linear dependence $J_c \propto 1/R$, or (which is the same) the constant width of hysteresis loops for all the samples being measured, leads to only one possible conclusion that the actual radius R of the region in which the screening current flows should not exceed the minimum average radius of grains in the sample. This means that the value of R must be smaller than 1 μm. This, however, contradicts the results of magnetic measurements obtained by different authors for K_3C_{60} as well as Rb_3C_{60}.[6,11,13,14] According to these data, the width of hysteresis loops increases with the grain size (see Table I), although the dependence is not linear. For example, as the value of R increases by three orders of magnitude (from 1 μm to 1 mm), the value of $\Delta M=\Delta m/V$, where Δm is the width of a hysteresis loop and V the sample volume, increases only by a factor of

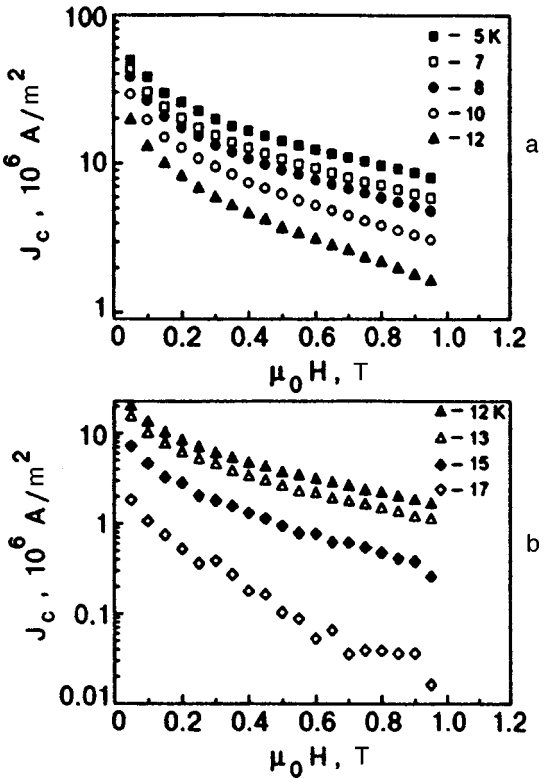

FIG. 3. Field dependence of the critical current density for K1 sample at various temperatures.

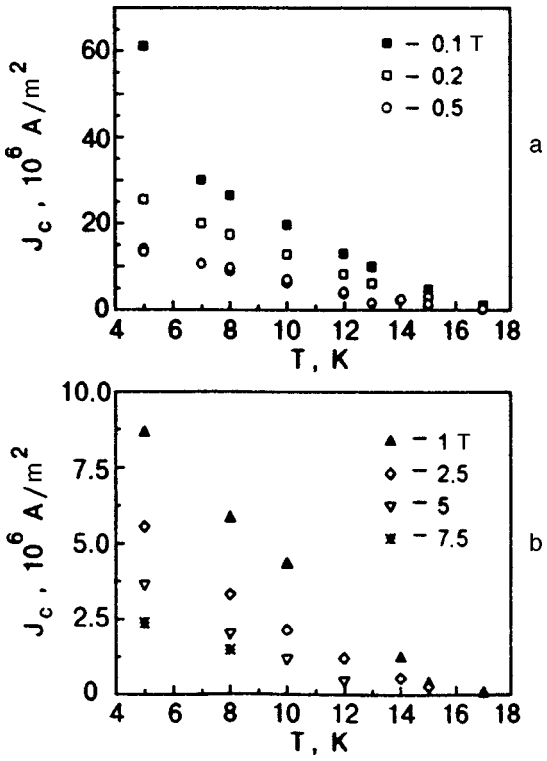

FIG. 4. Temperature dependence of the critical current density for K1 sample at different values of magnetic field.

10–30. This can be due to a weaker pinning in single crystals as compared to powders in view of the fact that single crystals have a more perfect structure, a smaller number of structural defects, and hence a smaller number of pinning centers.

It should be noted, however, that crystalline FS samples synthesized at present are polycrystals rather than single crystals. Many samples have a nonideal stoichiometry, and hence inclusions of a nonsuperconducting phase. Besides, the monocrystalline structure of C_{60} crystals is broken by doping, giving rise to a mosaic structure. In this connection, we can hardly expect that the pinning in such crystals will be much weaker than in powders. For this reason, the disproportionally small increase in ΔM as compared to the increase in R cannot be attributed only to a weaker pinning in single crystals. We can also assume that the values of J_c calculated for powders are slightly exaggerated since we assume that grains are absolutely isolated when we choose R equal to the average radius of grains. It must be borne in mind, however, that the surfaces of grains are the first to be doped and become superconducting in the course of doping. Consequently, grains are often electrically coupled or exhibit a weak Josephson coupling even in an unpressed powder. Naturally, this leads to values of R larger than the average size of grains, and the value of J_c calculated by formula (1) must accordingly be lower.

Irrespective of the nature of the phenomenon discussed above, it creates additional difficulties in the calculation of J_c and shows that the absolute values of critical current density calculated from the results of measurements of irreversible magnetization should be taken with care, especially if the value of R is not determined absolutely accurately. It was noted above, however, that the qualitative form of the temperature and field dependences of the critical current density obtained from these experiments must be correct.

While calculating the critical current density in sample K1 with 100% field screening, we assume that $R=1$ mm (sample size) since it has been proved that the granularity for supercurrents in the sample was not observed. Using formula (1), we obtain $J_c=6\times10^7$ A/m^2 at $T=5$ K and $\mu_0 H=0.05$ T. This value is close to those obtained by Irons *et al.*[11] on K_3C_{60} and Rb_3C_{60} crystals of the millimeter size. However, the values of J_c obtained for Rb_3C_{60}[14] are 15 times higher than our values. This difference can be due to the quality of crystals, and hence the pinning force.

The field and temperature dependences of critical current density for K1 are shown in Figs. 3 and 4. It can be seen that the critical current density decreases smoothly with increasing magnetic field and temperature. These values of J_c are virtually two orders of magnitude lower than those obtained on twinless YBCO single crystals (this material has the lowest anisotropy among HTSC).[15] The reason behind this difference in the values of J_c is unclear since the expected contribution of structure defects to the pinning of magnetic vortices also depends on the thermodynamic critical field H_c and the coherence length ξ. Both these parameters have close values for FS and HTSC.

The influence of internal structure of the sample on R can be seen clearly from the results obtained for K2 for which the value of ΔM is smaller by a factor of 1.3 than for K1. At first sight, this result appears as unexpected since the size of K2 is 1.5 times larger than that of K1. However, the

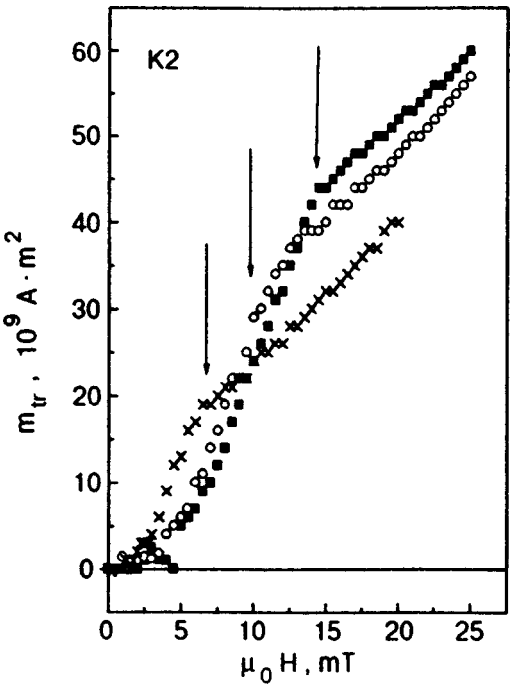

FIG. 5. Field dependence of the trapped magnetic moment $m_{\rm tr}$ for K2 sample at T, K: 5 (×), 7 (○), and 12 (■).

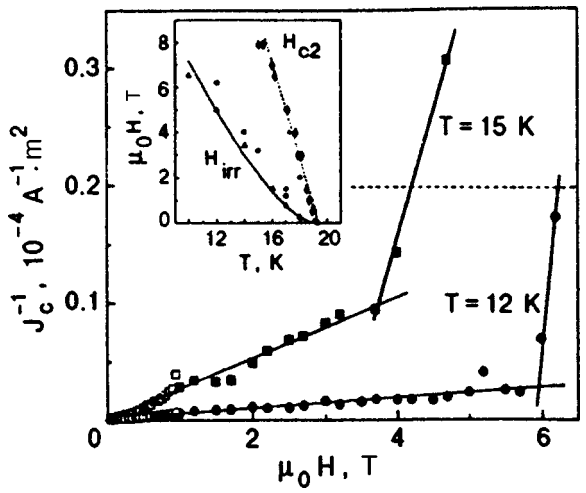

FIG. 6. Field dependence of $1/J_c$. The inset shows the temperature dependences of the upper critical field H_{c2} and the irreversibility field $H_{\rm irr}$ for samples K1 (dark symbols) and K3 (light symbols).

small value of ΔM in K2 can be explained by the presence of grains. It is well known (see the discussion of the quality of single crystals in Ref. 3) that a mosaic structure is formed in the sample as a result of doping. At the same time, grains can also appear due to the formation of microcracks in the single crystal. Indeed, ac measurements in K2 indicate the presence of intergranular peaks on the $\chi''(T)$ curve, which are absent in the case of K1 sample (see Fig. 2). Besides, the dependence of the trapped magnetic flux on the external magnetic field (see the details of experiment in Ref. 16) for K2 has a kink for the characteristic value of the field $\mu_0 H^*$ of the order of several mT. This dependence is shown in Fig. 5. We relate the emergence of the kink to the instant of time when the applied field reaches the center of the sample (or the center of grains). This kink is not manifested in this range of external fields for sample K1 whose size is smaller than that of K2, indicating the presence of grains for supercurrents in K2. The estimates of the average size of grains obtained from the experimental values of H^* give a value of the order of several tens of micrometers.[17] These grains are quite large and are formed in all probability due to the emergence of microcracks during sample doping.

An important characteristic of HTSC materials is the ''irreversibility point'' ($T_{\rm irr}$ or $H_{\rm irr}$) observed for the first time in experiments by Müller *et al.*[18] for La–Ba–Cu–O ceramics. For various values of external magnetic field, it was defined as the point at which ''field-cooled'' (FC) and ''zero-field-cooled'' (ZFC) temperature dependences merge into one reversible curve. This effect is observed for all HTSC, and the irreversibility curve $H_{\rm irr}(T)$ has become an object of detailed investigations for many years. From the point of view of fundamental studies, the $H_{\rm irr}(T)$ dependence provides information on the type of pinning in a sample and on structural peculiarities of the system of magnetic vortices. Most experimental results show that the irreversibility curve can be described by the equation

$$H_{\rm irr}=H_0(1-T/T_c)^m, \tag{2}$$

where H_0 is the value of $H_{\rm irr}$ at zero temperature. In a thermally activated flux flow (TAFF) model with collective pinning,[19] the value of m in Eq. (2) is 1.5, while $m=4/3$ in the vortex-glass (VG) model[20] and $m=2$ or 1.5 in the theory of vortex lattice melting.[21]

The irreversibility curve is usually determined in experiments as the point of merging the ZFC and FC curves (as, for example, for K_3C_{60} and Rb_3C_{60} powders in Ref. 22) or as a characteristic value of the field at which current densities drop below a certain value. The irreversibility curves for fullerides obtained by these methods are also described by Eq. (2) with the value of m between 1.47 and 2.15 (see Table I). However, the determination of $T_{\rm irr}$ and $H_{\rm irr}$ from these measurements is complicated and requires the application of certain criteria in view of the fact that both temperature and field dependences of magnetization gradually become reversible.

In our experiments, the irreversibility curve was determined from field dependences of critical current density, where $1/J_c$ is proportional to B in a wide range of external fields (Fig. 6). However, at certain values of field, the value of J_c decreases abruptly below the resolution limit of our instrument (see Fig. 6), the values of characteristic field being the lower the higher the temperature. These values of magnetic field is regarded as the irreversibility field $H_{\rm irr}$.

The temperature dependences of $H_{\rm irr}$ (irreversibility curves) obtained by this method for K1 and K3 samples are shown in the inset to Fig. 6. The irreversibility curves follow the power law (2) with $m=1.5$. Thus, the irreversibility curve can be described on the basis of the TAFF model.[19] It should be noted, however, that this value of exponent in (2) is also in accord with some models of vortex lattice melting.[21]

4. CONCLUSION

Using the measurements of magnetization, we studied the temperature and field dependences of the critical current density in single crystals of fulleride K_3C_{60}. On the basis of the critical state model, we obtained the critical current density $J_c = 6 \times 10^7$ A/m^2 at $T = 5$ K and $\mu_0 H = 0.05$ T, which is much smaller that the corresponding value for powders. It is shown that the internal structure of the sample considerably affects the characteristic value of R used for calculating J_c.

The irreversibility curve obtained in experiments follows a power law with an exponent $m = 1.5$ and can be described on the basis of the TAFF model. However, the final answer to the question about the nature of the irreversibility curve in FS cannot be obtained in view of insufficient amount of experimental data on the $H_{\rm irr}(T)$ dependence.

*E-mail: buntar@ati.ac.at

[1] A. F. Hebard, M. J. Rosseinsky, R. C. Haddon *et al.*, Nature (London) **350**, 600 (1991).
[2] C. P. Bean, Phys. Rev. Lett. **8**, 250 (1962).
[3] V. Buntar, F. M. Sauerzopf, H. W. Weber *et al.*, Phys. Rev. B **54**, 14952 (1996).
[4] G. S. Boebinder, T. T. M. Palstra, A. Passner *et al.*, Phys. Rev. B **46**, 5876 (1992).
[5] G. Sparn, J. D. Thompson, S.-M. Haung *et al.*, Science **252**, 1829 (1991); G. Sparn, J. D. Thompson, R. L. Whetten *et al.*, Phys. Rev. Lett. **68**, 1228 (1992).
[6] M. Baenitz, M. Heinze, E. Straube *et al.*, Physica C **228**, 181 (1994).
[7] W. A. Fietz and W. W. Webb, Phys. Rev. **178**, 657 (1969).
[8] M. W. Lee, M. F. Tai, S. C. Luo, and J. B. Shi, Physica C **245**, 6 (1995).
[9] V. Buntar, Physica C (in press).
[10] C. Politis, V. Buntar, and V. P. Seminozhenko, Int. J. Mod. Phys. **B7**, 2163 (1993).
[11] S. H. Irons, J. Z. Liu, P. Klavins, and R. N. Shelton, Phys. Rev. B **52**, 15517 (1995).
[12] R. D. Boss, J. S. Briggs, E. W. Jacobs *et al.*, Physica C **243**, 29 (1995).
[13] C. Politis, V. Buntar, W. Krauss, and A. Gurevich, Europhys. Lett. **17**, 175 (1992).
[14] S. Chu and M. E. McHenry, Phys. Rev. B **55**, 11722 (1997).
[15] F. M. Sauerzopf, H. P. Wiesinger, W. Kritscha *et al.*, Phys. Rev. B **43**, 3091 (1991).
[16] V. Buntar, F. M. Sauerzopf, and H. W. Weber, Phys. Rev. B **54**, R9651 (1996).
[17] M. W. McElfresh *et al.*, Physica A **168**, 308 (1990).
[18] K. A. Müller, M. Takashige, and J. G. Bednorz, Phys. Rev. Lett. **58**, 1143 (1987).
[19] Y. Yeshurun and A. P. Malozemoff, Phys. Rev. Lett. **60**, 2202 (1988); M. Tinkham, Phys. Rev. Lett. **61**, 1658 (1988); C. W. Hagen and R. Griessen, Phys. Rev. Lett. **62**, 2857 (1989).
[20] D. S. Fisher, M. P. A. Fisher, and D. A. Huse, Phys. Rev. B **43**, 130 (1991); P. L. Gammel, L. F. Schneemeyer, and D. J. Bishop, Phys. Rev. Lett. **66**, 953 (1991); R. H. Koch, V. Foglietti, W. J. Gallagher, *et al.*, Phys. Rev. Lett. **63**, 1511 (1989).
[21] A. Houghton, R. A. Pelcovits, and A. Sudbo, Phys. Rev. B **40**, 6763 (1989); E. H. Brandt, Phys. Rev. Lett. **63**, 1106 (1989); D. E. Farrel, J. P. Rice, and D. M. Ginsberg, Phys. Rev. Lett. **67**, 1165 (1991); R. G. Beck *et al.*, Phys. Rev. Lett. **68**, 1594 (1992); L. I. Glazman and A. E. Koshelev, Phys. Rev. B **43**, 2835 (1991); M. F. Schmidt, N. E. Israeloff, and A. M. Goldman, Phys. Rev. Lett. **70**, 2162 (1993); G. Blatter and B. Ivlev, Phys. Rev. Lett. **70**, 2621 (1993).
[22] E. Zeldov, D. Majer, M. Konczykowski *et al.*, Nature (London) **375**, 373 (1995).
[23] K. Holczer, O. Klein, G. Gruner *et al.*, Phys. Rev. Lett. **67**, 271 (1991).
[24] J. D. Thompson, G. Sparn, K. Holczer *et al.*, in *Physical and Material Properties of High-Temperature Superconductors* (ed. by S. L. Malic and S. S. Shah), Nova Science Publishers, Commack, NJ (1994).
[25] C. L. Lin, T. Mihalisin, N. Bykovetz *et al.*, Phys. Rev. B **49**, 4285 (1994).
[26] M. Warden, R. Schauwecker, P. Erhart *et al.*, Physica C **235-240**, 2505 (1994).
[27] V. Buntar, F. M. Sauerzopf, H. W. Weber *et al.*, *Recent Advances in Chemistry and Physics of Fullerenes and Related Materials*, *4*, 1021 (1997).

Translated by R. S. Wadhwa

On the theory of Josephson effect in a diffusive tunnel junction

E. V. Bezuglyi, E. N. Bratus' and V. P. Galaiko

*B. Verkin Institute for Low Temperature Physics and Engineering, National Academy of Sciences of the Ukraine, 310164 Kharkov, Ukraine**)

(Submitted September 16, 1998)
Fiz. Nizk. Temp. **25**, 230–239 (March 1999)

Specific features of the equilibrium current-carrying state of a Josephson tunnel junction between diffusive superconductors (with the electron mean free path l smaller than the coherence length ξ_0) are studied theoretically in the $1D$ geometry when the current does not spread in the junction banks. It is shown that the concept of ''weak link'' with the phase jump $\Phi \sim 1$ of the order parameter exists only for a low transmissivity of the barrier $\Gamma \ll l/\xi_0 \ll 1$. Otherwise, the presence of the tunnel junction virtually does not affect the distributions of the order parameter modulus and phase. It is found that the Josephson current flowing in the vicinity of the tunnel barrier induces localized states of electron excitations, which are a continuous analog of Andreev's levels in a ballistic junction. The depth of the corresponding ''potential well'' is much larger than the separation between an Andreev's level and the continuous energy spectrum boundary for the same transmissivity of the barrier. In contrast to a ballistic junction in which the Josephson current is transported completely by localized excitations, the contribution to current in a diffusive junction comes from the entire spectral region near the energy gap boundary, where the density of states differs considerably from its unperturbed value. The correction to the Josephson $j(\Phi)$ in the second order of the barrier transmissivity, which contains the second harmonic of the phase jump Φ, is calculated and it is found that the true expansion parameter $j(\Phi)$ of the perturbation theory for a diffusive junction is not the tunneling probability Γ, but a much larger parameter $W=(3\xi_0/4l)\Gamma$. This simplifies the conditions for the experimental observation of higher harmonics of $j(\Phi)$ in junctions with controllable transmissivity of the barrier.
[S1063-777X(99)00303-5]

1. INTRODUCTION

In recent years, considerable advances have been made in the technology of preparing low-resistance tunnel junctions with a comparatively high barrier transmissivity (tunneling probability) Γ. This applies primarily to controlled break- junctions[1] as well as systems based on $2D$ electron gas,[2] whose conductivity undergoes a crossover from tunnel- to metal-type conductivity upon a change in the barrier parameters. The problem of calculation of the Josephson current through a junction with an arbitrary transmissivity in the ballistic mode (with the electron mean free path $l \gg \xi_0$, where ξ_0 is the coherence length) was solved by many authors[3] on the basis of the model of a one-mode junction with massive current-carrying banks ensuring a rapid ''spreading'' of supercurrent and the equality of the order parameter modulus Δ at the barrier to its bulk value (the ''rigidity'' condition for Δ).

In the $1D$ geometry (e.d., a planar junction or a superconducting channel with a tunnel barrier[1)]), the problem is complicated considerably due to the change in the order parameter and the quasiparticle energy spectrum in the vicinity of the junction, which makes a contribution to the phase dependence of the current $j(\Phi)$. Antsygina and Svidzinskii[4] determined the corresponding corrections to $j(\Phi)$ of the order of Γ^2 for a pure ($l \gg \xi_0$) superconductor in the limit of low transmissivity $\Gamma \ll 1$:

$$\delta j(\Phi) = -\alpha(T) I(\Delta) \Gamma \left(\sin\Phi - \frac{1}{2}\sin 2\Phi \right), \quad \alpha(T) \sim 1, \tag{1}$$

$$I(\Delta) = \frac{\pi}{4} e \nu_F v_F \Gamma \Delta = I_c(\Delta)/\tanh(\Delta/2T), \tag{2}$$

where ν_F is the density of states, v_F the Fermi velocity, and $I_c(\Delta)$ the critical current through the junction.

In a diffusive superconductor (the ''dirty'' limit $l \ll \xi_0 = \sqrt{D/2\Delta}$, $D = v_F l/3$ is the diffusion coefficient), the calculation of the Josephson current for an arbitrary Γ is hardly possible[2)] even in a simple model disregarding the variation of the order parameter in the vicinity of the junction, using the numerical methods of solving equations for Green's functions averaged over the ensemble of scatterers. As a matter of fact, the boundary conditions for isotropic Green's functions $\hat{g}(\mathbf{r}, t_1 t_2)$ at the junction, which were obtained for the first time by Kupriyanov and Lukichev,[7], i.e.,

$$-l(\hat{g}\nabla\hat{g})_L = -l(\hat{g}\nabla\hat{g})_R = \frac{3}{4}\left\langle \frac{\mu d(\mu)}{r(\mu)} \right\rangle [\hat{g}_L, \hat{g}_R],$$

$$r(\mu) = 1 - d(\mu), \tag{3}$$

where $d(\cos\theta)$ is the tunneling probability for an electron impinging the barrier at an angle θ, and the subscripts R and L mark the value to the right and left of the barrier, are valid

only in the first order of smallness of the angle-averaged transmissivity $\Gamma=\langle \mu d(\mu)\rangle$. Lambert *et al.*[8] proved that the derivation of the boundary conditions in the general case ($d\sim 1$) is reduced to an analysis of a system of nonlinear integral equations for the terms in the expansion of the averaged Green's function $\hat{g}(\mathbf{r},\mathbf{p},t_1t_2)=\hat{g}(\mathbf{r},t_1t_2)+\mathbf{p}\cdot\hat{\mathbf{g}}_1(r,t_1t_2)+\ldots$ over Legendre polynomials. This problem can be solved only for $\Gamma\ll 1$ by writing the right-hand side of (3) in the form of a power series in Γ, which was used in Ref. 8 for calculating the corrections to the Josephson current of the order of Γ^2.

In this paper, we pay attention to the fact that the problem of calculation of the current–phase relation for a diffusive junction in the $1D$ geometry has a meaning only in the case of the low transmissivity of the barrier. Indeed, simple estimates obtained on the basis of the well-known formula for $j(\Phi)$ in the first order in Γ, which coincides with the Ambegaokar–Baratoff[9] result for a pure superconductor on account of the Anderson theorem, i.e.,

$$j_0(\Phi)=I(\Delta)\tanh\frac{\Delta}{2T}\sin\Phi, \tag{4}$$

show that even for $\Gamma\sim l/\xi_0\ll 1$ the critical current through the junction becomes of the order of the bulk thermodynamic critical current $n_s e v_{sc}$, where $v_{sc}\sim 1/m\xi_0$ is the critical velocity of the condensate, $n_s\sim m\nu_F D\Delta$ its density, m the electron mass, and $\hbar=1$. Thus, for $\Gamma\gg l/\xi_0$ the tunnel junction does not any longer play the role of ''weak link'' with the jump of the order parameter phase Φ and other features of a Josephson element. This follows even from the boundary conditions (3) if we use the estimate $\nabla\hat{g}\sim\hat{g}/\xi_0$ in the vicinity of the junction, which leads to $[\hat{g}_L,\hat{g}_R]\sim\sin\Phi\to 0$ for $\Gamma\gg l/\xi_0$ in the main approximation.[3)] This criterion of weak link can be also formulated in terms of the conductance of the system in the normal state: the resistance of the junction must be higher than the resistance of a layer of the current-carrying metal of thickness $\sim\xi_0$.

It follows hence that the parameter

$$W=(3\xi_0/4l)\Gamma\gg\Gamma \tag{5}$$

plays a fundamental role in the theory of Josephson effect for diffusive junction (the factor 3/4 is chosen for convenience of notation). We can attach to this parameter the meaning of the effective tunneling probability for Cooper pairs, which is higher than the conventional probability Γ of quasiparticle tunneling. Small values of $W\ll 1$ correspond to ''weak link'' conditions (Josephson effect). For $W>1$, the presence of a tunnel barrier virtually does not affect the supercurrent flow and the distribution of order parameter in a diffusive superconductor. Moreover, we can expect that it is W and not Γ that it a true parameter of the expansion of $j(\Phi)$ in the barrier transmissivity since the Anderson theorem (in the given case, the statement concerning the absence of a dependence of the Josephson current on the mean free path) is valid only in the main approximation in Γ (4), and hence this dependence must be manifested in higher-order terms in the expansion of $j(\Phi)$ in the emergence of an additional dimensionless parameter ξ_0/l in them, which vanishes as $l\to\infty$. An analysis of corrections to the current–phase dependence (3) carried out in Sec. 4 of this article in the next order in W confirms these considerations and proves that the corrections $\sim\Gamma^2$ to the boundary conditions (3) and Josephson current (4) obtained in Ref. 8 are insignificant indeed.

Another important result of the analysis of the current-carrying state of a diffusive Josephson junction obtained by us here is the conclusion concerning the emergence of localized states of electron excitations in the vicinity of the barrier. This phenomenon is well known for a ballistic tunnel junction[10,11] in which discrete energy levels

$$\varepsilon_n(\Phi)=\pm\Delta(1-d\sin^2\Phi/2)^{1/2}, \tag{6}$$

associated with Andreev's localization of electron excitations near the jump in the order parameter phase split from the continuous spectrum in the current-carrying state. A similar phenomenon also takes place in a diffusive junction in which, however, isolated coherent energy levels cannot exist due to electron scattering at impurities and defects. In this case, The most adequate description of the variation of the energy spectrum of excitations is the one in terms of their local density of states $N(\varepsilon,\mathbf{r})=\mathrm{Re}\,u^+(\varepsilon,\mathbf{r})$ (u^+ is the diagonal component of the retarded Green's function for the superconductor), which is assumed for brevity to be normalized to its value ν_F in the normal metal. In the absence of current, the density of states in a homogeneous superconductor has the standard form $N_0(\varepsilon)=|\varepsilon|\Theta(\varepsilon^2-\Delta^2)/\sqrt{\varepsilon^2-\Delta^2}$ [$\Theta(x)$ is the Heaviside function] with root singularities at the gap boundaries. In the current state, the momentum p_s of the superfluid condensate plays the role of a depairing factor smoothing the singularities of $N(\varepsilon)$ and reducing the energy gap $2\varepsilon_*$ by $\Delta-\varepsilon_*(p_s)\sim(Dp_s^2)^{2/3}$.[12] In the vicinity of a weak link, a similar (and main) factor suppressing the energy gap is the phase jump Φ which leads to the formation of a ''potential'' well having a width of the order of ξ_0 and containing localized excitations with an energy $|\varepsilon|<\Delta$ (see Sec. 3).

2. EQUATIONS FOR GREEN'S FUNCTION OF A JOSEPHSON JUNCTION WITH A LOW TRANSMISSIVITY

In order to calculate the density of states and equilibrium supercurrent

$$j=\frac{1}{4}e\nu_F v_F D\int_{-\infty}^{+\infty}d\varepsilon f_0(\varepsilon)\mathrm{Tr}\,\sigma_z(\hat{g}^+\nabla\hat{g}^+-\hat{g}-\nabla\hat{g}^-)(\varepsilon) \tag{7}$$

we must solve equations for the matrix retarded (advanced) Green's functions $\hat{g}^{\pm}(\mathbf{r},\varepsilon)$ averaged over the ensemble of scatterers:

$$[\sigma_z\varepsilon+\Delta\exp(i\sigma_z\chi)i\sigma_y,\hat{g}]=iD\nabla(\hat{g}\nabla\hat{g}), \tag{8}$$

$$\hat{g}^2=1. \tag{9}$$

Here Δ and χ are the modulus and phase of the order parameter and $f_0(\varepsilon)=(1/2)[1+\tanh(\varepsilon/2T)]$ is the equilibrium distribution function.

According to the normalization condition (9) for a Green's function, the matrix $\hat{g}$ can be presented in the form $\hat{g}=\boldsymbol{\sigma}\cdot\mathbf{u}$, where $\boldsymbol{\sigma}$ is the vector formed by Pauli matrices. Using the well-known relations $(\boldsymbol{\sigma}\cdot\mathbf{a})(\boldsymbol{\sigma}\cdot\mathbf{b})=\mathbf{a}\cdot\mathbf{b}+\mathbf{i}\boldsymbol{\sigma}[\mathbf{a}$

$\times\mathbf{b}]$, $[\boldsymbol{\sigma}_z,\boldsymbol{\sigma}]=2i[\boldsymbol{\sigma}\times\mathbf{s}]$, where $\mathbf{s}$ is the unit vector of ''isotopic spin'' directed along the z-axis in the space of Pauli matrices, we can obtain from (3), (8), and (9) the following equations and the boundary conditions for the vector Green's function $\mathbf{u}$:

$$\varepsilon[\mathbf{s}\times\mathbf{u}]+i\Delta[\chi\times\mathbf{u}]=(D/2)\nabla[\mathbf{u}\times\nabla\mathbf{u}],\quad \mathbf{u}^2=1, \tag{10}$$

$$\xi_0[\mathbf{u}\times\nabla\mathbf{u}]_{L,R}=2W[\mathbf{u}_L\times\mathbf{u}_R], \tag{11}$$

where $\chi=(\sin\chi,\cos\chi,0)$ is the symbolic vector of the order parameter phase.

Singling out the component of the vector $\mathbf{u}$ along the direction $\mathbf{s}$, i.e., $\mathbf{u}=\mathbf{s}u+i\mathbf{v}$ $(\mathbf{v}\cdot\mathbf{s}=0)$, we project Eqs. (10) onto the (x,y)-plane in the space of Pauli matrices:

$$\varepsilon\mathbf{v}-\Delta u\chi=(iD/2)\nabla(u\nabla\mathbf{v}-\mathbf{v}\nabla u),\quad u^2-\mathbf{v}^2=1 \tag{12}$$

and introduce the unit vector $\boldsymbol{\psi}=(\sin\psi,\cos\psi,0)$ directed along $\mathbf{v}$: $\mathbf{v}=\psi v$, where $\psi(\mathbf{r},\varepsilon)$ is the phase of ''anomalous'' Green's function v $(\nabla\psi=[\psi\times\mathbf{s}]\nabla\psi)$. The obtained system of scalar equations is a possible representation of Usadell equations:

$$\varepsilon v-\Delta u\cos(\psi-\chi)=(iD/2)[\nabla(u\nabla v-v\nabla u)-uv(\nabla\psi)^2], \tag{13}$$

$$\Delta v\sin(\psi-\chi)=(iD/2)\nabla(v^2\nabla\psi), \tag{14}$$

$$u^2-v^2=1, \tag{15}$$

and its solutions determine the value of supercurrent (7) according to

$$j(\Phi)=-e\nu_F D\int_{-\infty}^{+\infty}d\varepsilon f_0\,\mathrm{Im}(v^+)^2\nabla\psi^+. \tag{16}$$

Choosing the coordinate axis x at right angles to the contact plane $x=0$ $(\chi(+0)=-\chi(-0)=\Phi/2)$ and taking into account the continuity of Green's function and antisymmetry of their derivatives, we can easily obtain from (11) the boundary conditions to Eqs. (13) and (14) for $x\to+0$:

$$\xi_0(u\nabla v-v\nabla u)(0)=4Wu(0)v(0)\sin^2\psi(0), \tag{17}$$

$$\xi_0(v\nabla\psi)(0)=2Wv(0)\sin 2\psi(0). \tag{18}$$

Away from the junction, the behavior of the order parameter phases and Green's function is described by a linear asymptotic form corresponding to the given value of current

$$\xi(+\infty)=\psi(+\infty)=\chi_\infty+2p_s x,\quad p_s=(W/\xi_0)\sin\Phi, \tag{19}$$

i.e., of the superfluid momentum p_s whose magnitude is determined in the main approximation by the condition of equality of the current (4) through the junction to its value $j=\pi e\nu_F D p_s\Delta\tanh(\Delta/2T)$ in the bulk of the metal, and Green's functions tend to their asymptotic values satisfying Eqs. (13)–(15) for $\psi=\chi$ and $\nabla u=\nabla v=0$.

Using the parametrization $u=\cosh\theta$, $v=\sinh\theta$, which takes into account the normalization condition (15), we can put in correspondence to the vector Green's function $\mathbf{u}$ the following visual geometrical image.[13] The unit vector $\mathbf{u}$ in a normal metal is directed along the isospin axis z (which corresponds to a purely electron or hole state of excitation of a Fermi gas), while in a superconductor this vector is deflected from the axis through an imaginary angle $i\theta$ and turned about the isospin axis through the azimuthal angle ψ. In the spatially homogeneous case, this angle obviously coincides with the phase of the order parameter $(\psi=\chi)$, and the scalar Green's functions u and v are described by the formulas

$$u^{\pm}=\cosh\theta_s=\frac{\varepsilon}{\sqrt{(\varepsilon\pm i0)^2-\Delta^2}}, \tag{20}$$

$$v^{\pm}=\sinh\theta_s=\frac{\Delta}{\sqrt{(\varepsilon\pm i0)^2-\Delta^2}},$$

where $\pm i0$ defines the position of singularities of the retarded (advanced) Green's function in the complex plane ε, and the square root in (20) is defined so that $u^{\pm}\to\pm1$ for $\varepsilon\to+\infty$.

The equations (13)–(15) for Green's functions should be supplemented by the self-consistency conditions for the modulus and phase of the order parameter:

$$\Delta=\lambda\int_{-\infty}^{+\infty}d\varepsilon f_0\,\mathrm{Re}\,v^+, \tag{21}$$

$$\int_{-\infty}^{+\infty}d\varepsilon f_0\,\mathrm{Re}\,v^+\sin(\psi^+-\chi)=0, \tag{22}$$

where λ is the constant of superconducting interaction. Taking into account the current conservation law [Eqs. (14) and (22)], it is convenient to calculate the value of current at the barrier $(x\to+0)$ by expressing $\nabla\psi(0)$ in (16) with the help of (18) through the phase jump $2\psi(0)$:

$$j(\Phi)=-\frac{e}{2}\nu_F v_F\Gamma\int_{-\infty}^{+\infty}d\varepsilon f_0\,\mathrm{Im}[v^+(0)]^2\sin 2\psi^+(0), \tag{23}$$

which allows us to single out explicitly the small parameter of the theory, i.e., the barrier transmissivity Γ. It can easily be verified that in the main approximation using the unperturbed values of Green's function (20) and phase $\psi(0)\approx\chi(0)=\Phi/2$, formula (23) leads to the result (4).

A simplifying factor in the case of a low transmissivity of the barrier is that the quantities $\psi-\chi$ and $\nabla\psi$ proportional to the current through the junction are small (see (18) and (14)), and hence we can omit in Eq. (13) the terms quadratic in W and containing the phase. Replacing $\psi(0)\approx\chi(0)=\Phi/2$ in the boundary conditions (17) and (18) to the same degree of accuracy, we obtain the equation and the boundary conditions for the parameter θ:

$$\varepsilon\sinh\theta-\Delta(x)\cosh\theta=(iD/2)\nabla^2\theta, \tag{24}$$

$$\xi_0\nabla\theta(0)=2W\sinh 2\theta(0)\sin^2\Phi/2,$$

$$\theta(+\infty)=\theta_s. \tag{25}$$

An attempt to apply the perturbation theory directly to the solution of Eq. (24) $(\theta(x)=\theta_0+\theta_1(x),\ \Delta(x)=\Delta_0+\Delta_1(x))$ leads to an expression for the correction $\theta_1(x)$ containing nonintegrable singularities at the gap boundaries, and as a consequence, to the divergence of the corresponding correction to the Josephson current (4). This is associated with the emergence of localized states of quasiparticles at a

tunnel junction in the current-carrying state mentioned in Introduction. These states will be considered in the next section.

3. LOCALIZED STATES AT A TUNNEL BARRIER

It will be proved below that the depth of the ''potential well'' in the vicinity of the barrier is much larger than the scale of variation of the order parameter. Consequently, it is sufficient to confine an analysis of the behavior of the density of state to the model with a constant Δ, in which Eq. (24) has a simple solution describing the attenuation of perturbations of Green's functions at a distance $\sim\xi_0$ from the barrier:

$$\tanh\frac{\theta(x)-\theta_s}{4}=\tanh\frac{\theta(0)-\theta_s}{4}\exp(-k_\varepsilon|x|),$$

$$k_\varepsilon^{-2}=i\xi_0^2\sinh\theta_s,\quad \mathrm{Re}\,k_\varepsilon>0. \tag{26}$$

The quantity $\theta(0)$ satisfies the boundary condition following from (25) and (26):

$$k_\varepsilon\xi_0\sinh\frac{\theta_s-\theta(0)}{2}=\gamma\sinh 2\theta(0),$$

$$\gamma=W\sin^2\Phi/2\ll 1, \tag{27}$$

which can be reduced to the eighth-degree algebraic equation in $z=\exp\theta(0)$:

$$2z^3(z-z_s)^2=i\gamma^2(z_s^2-1)(z^4-1)^2,\quad z_s=\exp\theta_s. \tag{28}$$

In the general case (for an arbitrary ε), the solution of Eq. (28) can be obtained only numerically, but the presence of the small parameter γ in (27) and (28) makes it possible to apply the perturbation theory. Far away from the spectrum boundary, we can put $\theta(0)=\theta_s$ on right-hand side of (27), which leads to the following expression for the correction to the density of states at the barrier:

$$N(\varepsilon,0)-N_0(\varepsilon)=-2\gamma\,\mathrm{Re}(\sqrt{i\sinh^3\theta_s}\sinh 2\theta_s), \tag{29}$$

that becomes obviously inapplicable for $|\varepsilon|\to\Delta$, where $|\theta_s|\to\infty$. In this region, we must apply the modified perturbation theory (MPT) by putting $|z|$, $|z_s|\gg 1$ for an arbitrary (not necessarily small) value of $z-z_s$. This not only reduces the degree of the general equation (28), but also allows us to write it in a universal form free of the depairing parameter γ:

$$(y\sqrt{E}-1)^2=iy^5,\quad y=z/\beta\sqrt{2},$$

$$E=\beta^2(\varepsilon-\Delta)/\Delta,\quad \beta=(2/\gamma)^{1/5}\gg 1. \tag{30}$$

Relations (30) show that the increase in the density of states is bounded by a quantity of the order of $\beta\sim W^{-2/5}$ as we approach the spectrum boundary, and the range of applicability of the conventional perturbation theory (29) is determined by the condition $(\varepsilon-\Delta)/\Delta\gg\beta^{-2}$ and overlaps with the region of applicability $(\varepsilon-\Delta)/\Delta\ll 1$ of the MPT. The boundary ε_* of the spectrum (the position of the bottom of the potential well) below which the density of states vanishes corresponds to the emergence of a purely imaginary root of the equation (30) at the point $E_*=-(25/6)(2/3)^{1/5}\approx-3.842$

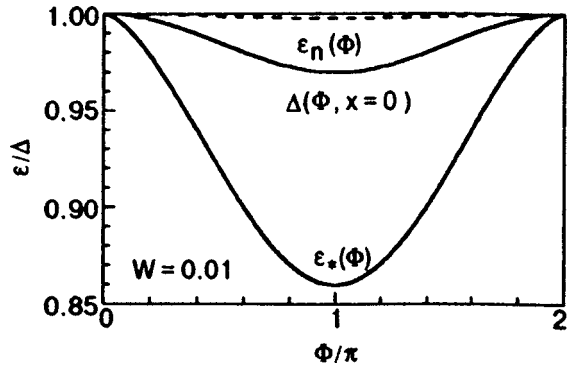

FIG. 1. Dependence of the position of the bottom of the ''potential well'' ε_* (31) and the order parameter $\Delta(0)$ (49) in the vicinity of the tunnel junction on the phase difference Φ (solid curves) at $T=0$, $W=0.01$ and $\xi_0/l=5$. The dashed curve shows for comparison the position of the Andreev level in a pure one-mode junction (5) for the same barrier transmissivity.

$$\varepsilon_*(\Phi)=\Delta\left[1-C\left(W\sin^2\frac{\Phi}{2}\right)^{4/5}\right],$$

$$C=\frac{25}{3\times 6^{1/5}}\approx 5.824. \tag{31}$$

The dependence of the position of the spectrum boundary on the phase jump at the junction is illustrated in Fig. 1 in which a similar dependence of the position of the Andreev level (6) in a junction between pure superconductors is shown for comparison. It should be noted that the scale of variation of $\varepsilon_*(\Phi)$ is much larger than the splitting of the Andreev level from the boundary of the continuous spectrum for the same barrier transmissivity. This is associated with the large value of the depairing parameter γ in the diffusive junction as compared to the splitting parameter Γ of the Andreev level as well as with the large numerical value of the constant C defining the shift of the spectrum boundary (31). Figure 2 shows the results of numerical calculation of the density of states at the junction on the basis of the general formula (28) for different values of the depairing parameter, which prove that in addition of the root singularity $(\sim\sqrt{\varepsilon-\varepsilon_*})$ at the spectrum boundary, the quantity $N(\varepsilon)$

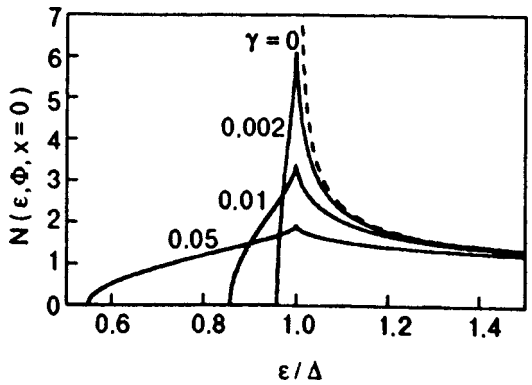

FIG. 2. Dependence of the density of states $N(\varepsilon,\Phi,0)$ at the tunnel junction on the energy of quasiparticles for various values of the depairing parameter $\gamma=W\sin^2(\Phi/2)$ (solid curves). The dashed curve shows the energy dependence of the unperturbed density of states $N_0(\varepsilon)$.

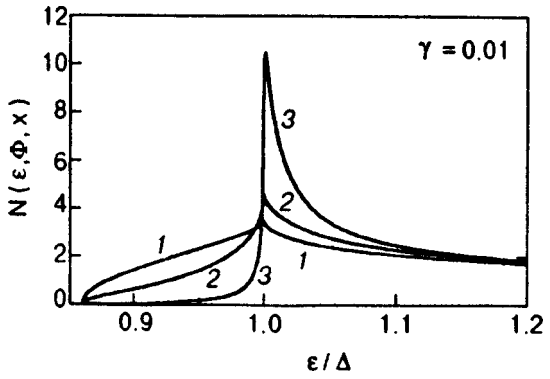

FIG. 3. Energy dependence of the density of states $N(\varepsilon,\Phi,x)$ for $\gamma=0.01$ at different distances x from a diffusive tunnel junction: 0 (curve *1*), ξ_0 (curve *2*), and $5\xi_0$ (curve *3*).

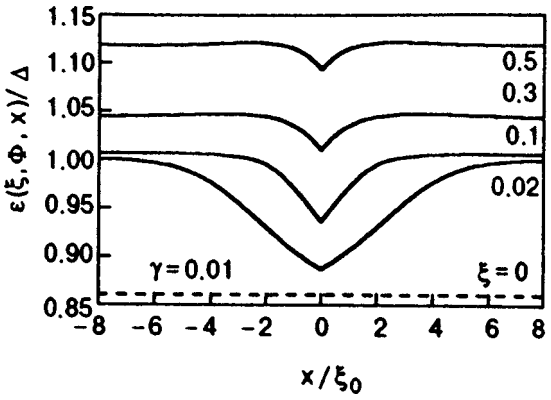

FIG. 4. Lines corresponding to the number of states of quasiparticles $\xi(\varepsilon,\Phi,x)=\text{const}$ (34) for $\gamma=0.01$ and various values of ξ in the vicinity of the junction. The dashed line shows the position of the bottom of the ''potential well'' ($\xi=0$, $\varepsilon=\varepsilon_*(\Phi)$).

has a ''beak-type'' root singularity for $\varepsilon=\Delta$. Its physical nature is associated with an indefinite increase in the attenuation length k_ε^{-1} of the perturbation of Green's function (26) in the vicinity of the gap boundary in the bulk of the metal. For $\varepsilon_*<\varepsilon<\Delta$, the density of states decreases exponentially with increasing distance from the junction to $\geqslant\xi_0$ (Fig. 3), which corresponds qualitatively to the image of the potential well of depth $\Delta-\varepsilon_*$ and of width $\sim\xi_0$ with excitations localized in them.

It is well known that Josephson current is carried through a ballistic junction by localized excitations only and can be presented in the following visual form:

$$j(\Phi)=-2e\sum_n \frac{\partial\varepsilon_n(\Phi)}{\partial\Phi}\tanh\frac{\varepsilon_n(\Phi)}{2T}, \tag{32}$$

where the index n labels Andreev's levels. At the same time, formula (23) for current expressed in the MPT approximation in terms of the reduced variables (30), i.e.,

$$j(\Phi)\approx -I(\Delta)\tanh\frac{\Delta}{2T}\sin\Phi\int_{E_*(\Phi)}^{\infty}\frac{dE}{\pi}\,\mathrm{Im}(y^+)^2=j_0(\Phi) \tag{33}$$

shows that the charge transfer in a diffusive junction is performed not only by the states in the potential well ($E<0$, $\varepsilon<\Delta$), but also by excitations with energy $\varepsilon>\Delta$ in the region $\varepsilon-\Delta\sim\Delta\beta^{-2}$, where the density of states differs significantly from the unperturbed value $N_0(\varepsilon)$. It should be noted in this connection that Argaman[14] proposed an analog of the formula (32) for a diffusive system, which can be obtained by the replacement of the energy $\varepsilon_n(\Phi)$ of Andreev's levels by the local value $\varepsilon(\xi,\Phi,x)$ of the excitation energy for $x=0$, which is adiabatically deformed by supercurrent, using instead of the discrete number n the continuous variable

$$\xi=\int_{\varepsilon_*(\Phi)}^{\varepsilon(\xi,\Phi,x)}d\varepsilon' N(\varepsilon',\Phi,x) \tag{34}$$

viz., the number of states with an energy smaller than ε ($\xi=\Theta(\varepsilon^2-\Delta^2)\sqrt{\varepsilon^2-\Delta^2}$ for a homogeneous superconductor).[4)] We can propose that the contributions from the bound and delocalized states to the Josephson current are taken into account simultaneously by the formula

$$j(\Phi)=-2e\nu_F\int_0^\infty d\xi\frac{\partial\varepsilon(\xi,\Phi,0)}{\partial\Phi}\tanh\frac{\varepsilon(\xi,\Phi,0)}{2T}, \tag{35}$$

which, however, leads to correct results only in the case of a homogeneous current-carrying state (where $\nabla\chi$ plays the role of Φ) or a broad *SNS*-junction (with a width $L\gg\xi_0$ of the normal superlayer) and is inapplicable for a narrow bridge and tunnel junction. Nevertheless, the application of the function $\varepsilon(\xi,\Phi,x)$ is useful in these cases also since this allows us to visualize the variation of the energy distribution of quasiparticle states in the vicinity of the junction (Fig. 4).

4. CURRENT–PHASE DEPENDENCE FOR A JUNCTION IN THE SECOND ORDER IN *W*

Although the modified perturbation theory for Green's function in the energy representation described in the preceding section is the most physically visual method operating with actual excitation energies. it leads to considerable formal difficulties in the calculation of corrections to the Josephson current (4). Indeed, it was shown in the previous section that the expression for $j(\Phi)$ calculated on the basis of the MPT for Green's functions (33) coincides with (4) since the small MPT parameter β^{-2} cancels out as we go over to the reduced variables (30). Thus, in order to calculate the corrections to (4) we are interested in, we must leave approximation (30) that describes the behavior of Green's functions correctly only in a narrow range of singularity in the density of states. For this purpose, it is convenient to use the formalism of temperature Green's functions by going over from integration with respect to energy in (21)–(23) to summation over the Matsubara frequencies $\omega_n=\pi T(2n+1)$, $n=0,\pm1,\pm2,\ldots$:

$$j(\Phi)=-\pi e\nu_F v_F\Gamma T\sum_{\omega_n>0}\mathrm{Re}\,v^2(0)\sin 2\psi(0), \tag{36}$$

$$\Delta(x)=-2\pi\lambda T\sum_{\omega_n>0}\mathrm{Im}\,v(x) \tag{37}$$

and making the substitution $\varepsilon \to i\omega_n$ in Eq. (24). This allows us to avoid divergences of the type (29) in perturbation theory which, unlike the MPT, makes it possible to take into account the coordinate dependence $\Delta(x)$.

It is expedient to use as the main approximation in the asymptotic expansion $\theta = \theta_0 + \theta_1 + \ldots$ the ''adiabatic'' value of Green's function corresponding to the local value of $\Delta(x) = \Delta + \Delta_1(x)[\Delta_1(\infty) = 0]$:

$$u_0(x) = \cosh\theta_0(x) = \frac{\omega_n}{\tilde{\omega}_n(x)}, \quad v_0(x) = \sinh\theta_0(x) = \frac{\Delta}{\tilde{\omega}_n(x)},$$

$$\tilde{\omega}_n(x) = \sqrt{\omega_n^2 + \Delta^2(x)}. \tag{38}$$

In this case, the correction $\theta_1(x)$ corresponds to the nonhomogeneous equation

$$\nabla^2\theta_1 - k_\omega^2\theta_1 = \nabla^2\theta_0, \quad k_\omega^2 = 2\tilde{\omega}_n/D \tag{39}$$

with the boundary conditions

$$\nabla\theta_1(+0) = 2W\sinh 2\theta_s \sin^2\Phi/2, \quad \theta_1(\infty) = 0,$$

where $\cosh\theta_s = \omega_n/\tilde{\omega}_n$ ($\tilde{\omega}_n = \sqrt{\omega_n^2 + \Delta^2}$) is the value of the Green's function far away from the junction with the unperturbed value of Δ.

The self-consistency condition for $\Delta_1(x)$ following from the equation (21), i.e.,

$$\Delta_1(q) T\sum_{\omega_n>0} \frac{\Delta^2}{\tilde{\omega}_n^3} = -T\sum_{\omega_n>0} \frac{\omega_n}{\tilde{\omega}_n} \mathrm{Im}\,\theta_1(i\omega_n, q) \tag{40}$$

completes the system of equations for determining the corrections θ_1 and Δ_1, whose solution in the Fourier representation has the form

$$\Delta_1(q) = -8W\Delta \frac{B(q)}{\xi_0 A(q)} \sin^2\frac{\Phi}{2},$$

$$\theta_1(i\omega_n, q) = 8W\Delta \frac{i\omega_n}{\tilde{\omega}_n} \frac{1}{q^2 + k_\omega^2} \frac{A(0)}{\xi_0 A(q)} \sin^2\frac{\Phi}{2}, \tag{41}$$

$$A(q) = A(0) + q^2 B(q), \quad A(0) = 2\pi T\sum_{\omega_n>0} \frac{\Delta^2}{\tilde{\omega}_n^3}, \tag{42}$$

$$B(q) = 2\pi T\sum_{\omega_n>0} \frac{\omega_n^2}{\tilde{\omega}_n^3} \frac{1}{q^2 + k_\omega^2},$$

$$[\theta_1(i\omega_n, x), \Delta_1(x)] = \int_{-\infty}^{+\infty} \frac{dq}{2\pi} e^{iqx} (\theta_1(i\omega_n, q), \Delta_1(q)).$$

As regards the correction to the asymptotic value (19) of the phase $\psi(x)$ of the Green's function, it is equal to zero in this approximation. In order to prove this, we introduce the quantity $\varphi = \psi - \chi \ll 1$, which, according to (14), satisfies the equation

$$\nabla^2\varphi - k_\omega^2\varphi = -\nabla^2\chi_1, \tag{43}$$

where $\chi_1 = \chi(x) - \chi(\infty)$ is a correction to (19) localized near the junction. Taking into account the boundary condition $\nabla\varphi(0) = -\nabla\chi_1(0)$ following from (18) and (19), we find that this equation has the simple solution $\varphi(i\omega_n, q) = -q^2\chi_1(q)/(q^2 + k_\omega^2)$ which leads, after the substitution into the self-consistency condition (22), to the following homogeneous integral equation for $\chi_1(q)$:

$$T\sum_{\omega_n>0} \frac{\Delta}{\tilde{\omega}_n} \int_{-\infty}^{+\infty} dq \frac{q^2\cos qx}{q^2 + k_\omega^2} \chi_1(q) = 0. \tag{44}$$

The only nonsingular solution of Eq. (14) is $\chi_1(q) \equiv 0$, which proves the absence of a correction to the Josephson current due to the deviation of the behavior of the phases of the order parameter and Green's functions from the linear law (19). This result can be explained as follows. The correction $\chi_1(x)$ is obviously of the order of the small correction $p_{s1}(x)$ to the constant value p_s (19) in the vicinity of the junction, that ensures the conservation of the current upon a change in $N(\varepsilon)$ and Δ. Since the value of $p_s \sim W$, the correction to this quantity, and hence $\chi_1(x)$ and φ have a higher order of smallness ($\sim W^2$) than the corrections of the order of W we are interested in.

Substituting the obtained solution (41) and (42) into formula (23), we obtain the required correction to the Josephson current:

$$\delta j = j(\Phi) - j_0(\Phi) = -\frac{4T}{\Delta} I(\Delta)\sin\Phi \sum_{\omega_n>0} \mathrm{Re}\left(v^2 + \frac{\Delta^2}{\tilde{\omega}_n^2}\right)$$

$$= -I(\Delta) W_0 Z(T)\left(\sin\Phi - \frac{1}{2}\sin 2\Phi\right), \tag{45}$$

$$Z(T) = \frac{16}{\pi}\sqrt{\Delta\Delta_0}\, T\sum_{\omega_n>0} \frac{\omega_n^2}{\tilde{\omega}_n^4} \int_{-\infty}^{+\infty} \frac{dk}{k^2 + \tilde{k}_\omega^2}\left(1 + \frac{\tilde{k}_\omega^2 B(k)}{A(k)}\right),$$

$$\tilde{k}_\omega = \frac{\tilde{\omega}_n}{\Delta}, \tag{46}$$

where $A(k)$ and $B(k)$ are defined by formulas (42) upon the substitution $k_\omega \to \tilde{k}_\omega$, and W_0 and Δ_0 are the values of W and Δ at $T = 0$.

At low temperatures ($T \ll \Delta$), the summation over ω_n in formulas (42) and (46) can be replaced by integration with respect to the continuous variable ω:

$$A(0) = 1,$$

$$B(k) = \int_0^\infty \frac{\tanh^2 v\, dv}{k^2 + \cosh v} = \frac{1}{k^4}\left[\frac{\pi}{2} - 2\sqrt{1-k^2} \times \arctan\left(\frac{1-k^2}{1+k^2}\right)^{1/2} - k^2\right],$$

which leads to the following asymptotic value of the function $Z(T)$ for $T \to 0$:

$$Z(T) = \frac{8}{\pi^2}\int_0^\infty dk\left[\frac{\pi k^2}{(1+k^2)^{9/4}} + \frac{2B^2(k)}{1 + k^2 B(k)}\right] \approx 2.178,$$

$$T \ll \Delta. \tag{47}$$

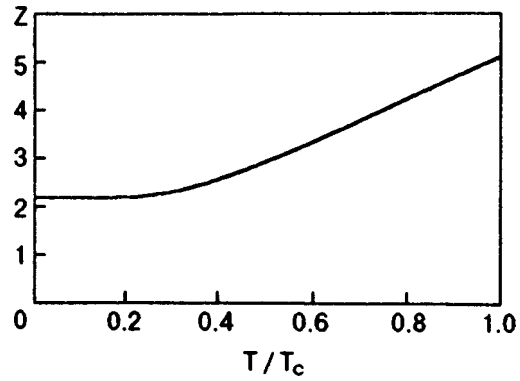

FIG. 5. The function $Z(T)$ (46) defining the temperature dependence of the ratio $\delta j(\Phi)/I(\Delta)$ (45).

In the vicinity of critical temperature ($\Delta \ll T$), the quantity $A(0) \approx 7\zeta(3)\Delta^2/4\pi^2T^2$ is small, and the main contribution to integral (46) comes from the region of small wave vectors $k \sim \Delta/T$ corresponding to damping of perturbations at large distances of the order of $\xi(T) \sim (T_c - T)^{-1/2}$. This allows us to replace the function $B(k)$ by its value $\pi\Delta/4T$ for $k=0$:

$$Z(T) = \frac{32\sqrt{\Delta\Delta_0}}{\pi^3 T} \sum_{n \geqslant 0} \frac{1}{(2n+1)^2} \int_0^\infty \frac{B(0)\,dk}{A(0) + k^2 B(0)}$$

$$= 2\pi \left(\frac{\pi\Delta_0}{7\zeta(3)T_c} \right)^{1/2} \approx 5.099, \quad \Delta \ll T. \tag{48}$$

The results of numerical calculations of the $Z(T)$ dependence in the entire temperature range $0 < T < T_c$ are presented in Fig. 5.

Similarly, by using (41) and (42) we can calculate the asymptotic values of the correction $\Delta_1(0)$ to the unperturbed value of the order parameter at the junction:

$$\frac{\Delta_1(0)}{\Delta_0} = -\alpha(T) W_0 \sin^2 \frac{\Phi}{2}, \quad \alpha(0) = 3.037,$$

$$\alpha(T_c) = 5.782. \tag{49}$$

The dependence of the order parameter $\Delta(0)$ on the phase jump at the junction at $T=0$ presented in Fig. 1 shows that the main contribution to the energy gap suppression comes from the depairing mechanism considered in Sec. 3, and the change in the order parameter is smaller than $\varepsilon_*(\Phi)$.

The structure and the phase and temperature dependences of the correction to the Josephson current (45) in a diffusive superconductor virtually coincide with expression (1) for a junction between pure metals except the following circumstance noted in Introduction: the parameter of the expansion of $j(\Phi)$ in the transmissivity of the junction for $l \ll \xi_0$ is not the tunneling probability Γ, but a considerably larger parameter W (5). This allows us to observe higher harmonics of the current–phase dependence in diffusive tunnel junction with a comparatively high resistance. Koops *et al.*[17] apparently reported on the first experimental results in this field.

The theory discussed above describes the current–phase dependence for a diffusive Josephson junction in the entire temperature range $0 \leqslant T < T_C$ except a narrow neighborhood of T_c in which $\Delta/T_c \sim W_0$ (while in a pure superconductor $\Delta/T_c \sim \Gamma$), the magnitude of corrections (45) and (1) becomes equal to $J_0(\Phi)$, while the correction (49) to Δ becomes equal to its unperturbed value. This means that in the definition of the parameter W (5) near T_c the coherence length $\xi_0(T)$ describing the characteristic scale of spatial variations of Green's function and density of states should be replaced by the characteristic length $\xi(T)$ of variation of the order parameter (healing length) in the Ginzburg–Landau theory, whose order of magnitude is the same as ξ_0 far away from T_c. Taking into account the results of calculations of $j(\Phi)$ for a pure superconductor in the vicinity of T_c,[5] we can obtain the following interpolation estimate of the effective transmissivity W suitable for any temperatures and mean free paths:

$$W \sim \Gamma\,\xi(T) \left(\frac{1}{l} + \frac{1}{\xi(0)} \right). \tag{50}$$

As we approach T_c, the value of W increases unlimitedly, this is accompanied by a decrease in the phase jump for a given external current bounded by its critical value. Thus, in the $1D$ geometry for an indefinitely large normal resistance of the junction, there exists a narrow region near T_c in which the phase difference of the order parameter at the junction is small up to values of current of the order of the bulk critical current.

The author are grateful to T. N. Antsygina and V. S. Shumeiko for fruitful discussions.

This research was supported by the Foundation for Fundamental Studies at the National Academy of Sciences of the Ukraine (Grant No. 2.4/136).

*)E-mail: bezugly@ilt.kharkov.ua

1)The transverse size of the junction is assumed to be smaller than the Josephson penetration depth, which ensures the uniform distribution of the current over the cross section of the junction.

2)The only exception is the case of temperatures close to critical, when the presence of the small parameter Δ/T_c makes it possible to formulate the effective computational algorithm of the solution of this problem.[5,6]

3)Strictly speaking, in this relation contains the jump in the phase of Green's function instead of the jump in the order parameter phase, but these quantities virtually coincide for $\Gamma \ll 1$ (see Sec. 4).

4)The concept of adiabatic deformation of ''energy levels'' in the continuous spectrum of a superconducting diffusive system in the current-carrying state and their classification on the basis of the continuous ''quantum number'' ξ was introduced for the first time in Ref. 15 and systematically used in Ref. 16.

[1] N. van der Post, E. T. Peters, I. K. Yanson, and J. M. van Ruitenbeek, Phys. Rev. Lett. **73**, 2611 (1994).
[2] H. Takayanagi, T. Akazaki, and J. Nitta, Phys. Rev. Lett. **75**, 3533 (1995).
[3] W. Haberkorn, H. Knauer, and S. Richter, Phys. Status Solidi **47**, K161 (1978); A. V. Zaitsev, Zh. Éksp. Teor. Fiz. **86**, 1742 (1984) [Sov. Phys. JETP **59**, 1015 (1984); G. B. Arnold, J. Low Temp. Phys. **59**, 143 (1985).
[4] T. N. Antsygina and A. V. Svidzinskii, Teor. Mekh. Fiz. **14**, 412 (1973).
[5] V. P. Galaiko, A. V. Svidzinskii, and V. A. Slyusarev, Zh. Éksp. Teor. Fiz. **56**, 835 (1969) [Sov. Phys. JETP **29**, 454 (1969).
[6] E. N. Bratus' and A. V. Svidzinskii, Teor. Mekh. Fiz. **30**, 239 (1977).
[7] M. Yu. Kupriyanov and M. F. Lukichev, Zh. Éksp. Teor. Fiz. **94**, 139 (1987) [Sov. Phys. JETP **67**, 1163 (1987).

[8] C. J. Lambert, R. Raimondi, V. Sweeney, and A. F. Volkov, Phys. Rev. B **55**, 6015 (1997).
[9] V. Ambegaokar and A. Baratoff, Phys. Rev. Lett. **10**, 486 (1963).
[10] A. Furusaki and M. Tsukada, Phys. Rev. B **43**, 10164 (1991).
[11] S. V. Kuplevakhskii and I. I. Fal'ko, Fiz. Nizk. Temp. **17**, 961 (1991) [Sov. J. Low Temp. Phys. **17**, 501 (1991).
[12] Yu. N. Ovchinnikov, Zh. Éksp. Teor. Fiz. **59**, 128 (1970) [Sov. Phys. JETP **32**, 72 (1970).
[13] Yu. V. Nazarov, Phys. Rev. Lett. **73**, 1420 (1994).
[14] N. Argaman, Cond. Mat./9709001 (1997).
[15] V. P. Galaiko, Zh. Éksp. Teor. Fiz. **64**, 1824 (1973) [Sov. Phys. JETP **37**, 922 (1973).
[16] E. V. Bezuglyi and A. Yu. Azovskii, Fiz. Nizk. Temp. **11**, 1248 (1985) [Sov. J. Low Temp. Phys. **11**, 691 (1985)].
[17] M. C. Koops, G. V. van Duyneveldt, A. N. Omelyanchouk, and R. de Bruyn Ouboter, Czech. J. Phys. **46**, Suppl., 673 (1996).

Translated by R. S. Wadhwa

Coherent current states in a mesoscopic four-terminal Josephson junction

Malek Zareyan

Institute for Advanced Studies in Basic Sciences, 45195-159, Gava Zang, Zanjan, Iran

A. N. Omelyanchuk

*B. Verkin Institute for Low Temperature Physics and Engineering, National Academy of Sciences of Ukraine, 47 Lenin Ave., 310164 Kharkov, Ukraine**

(Submitted October 13, 1998)
Fiz. Nizk. Temp. **25**, 240–248 (March 1999)

A theory is offered for the ballistic 4-terminal Josephson junction. The studied system consists of a mesoscopic two-dimensional normal rectangular layer which is attached on each side to the bulk superconducting banks (terminals). A relation is obtained between the currents through the different terminals, that is valid for arbitrary temperatures and junction sizes. The nonlocal coupling of the supercurrents leads to a new effect, specific for the mesoscopic weak link between two superconducting rings: an applied magnetic flux through one of the rings produces a magnetic flux in the other ring even in the absence of an external flux through the other one. The phase dependent distributions of the local density of Andreev states, of the supercurrents and of the induced order parameter are obtained. The ''interference pattern'' for the anomalous average inside the two-dimensional region can be regulated by the applied magnetic fluxes or the transport currents. For some values of the phase differences between the terminals, the current vortex state and the two-dimensional phase slip center appear.
 [S1063-777X(99)00403-X]

1. INTRODUCTION

The Josephson multiterminal junction presents a microstructure in which the weak coupling takes place between several massive superconducting banks (terminals).[1–3] Compared with the conventional (2-terminal) Josephson junctions[4] such systems have additional degrees of freedom and a corresponding set of the control parameters. As a result, for example, the current- or voltage-biased and the magnetic flux-driven regimes can be combined in one multiterminal junction. The specific multichannel interference effects were studied theoretically and experimentally in the novel superconducting device, a 4-terminal SQUID controlled by the transport current.[5–7] Recently another system based on a Josephson 4-terminal junction was studied.[8] It consists of two superconducting rings, each interrupted by a Josephson junction, which are at the same time weakly coupled with each other. The macroscopic quantum states of such a composite system can be regulated by the difference of the magnetic fluxes applied through the rings, in analogy with the phase difference between two weakly coupled bulk superconductors. The nonlinear coupling via the Josephson 4-terminal leads to the cooperative behavior of the rings in some region of the applied magnetic fluxes, which was called[8] magnetic flux locking.

The 4-terminal junction, which was studied in Refs. 5–8, is a system of short microbridges going from a weak point to massive superconducting banks (Fig. 1a). The order parameter (both its amplitude and phase) in the common center is a function of the currents through all the microbridges. The supercurrent flowing into the ith bank is determined by the phases of the order parameter φ_i $(i=1,...4)$ in all the banks[5]:

$$I_i=\frac{\pi\Delta_0^2(T)}{4eT_c}\frac{1}{\Sigma_j 1/R_j}\sum_j\frac{1}{R_iR_j}\sin(\varphi_i-\varphi_j). \tag{1}$$

The relation (1) was obtained in the frame of the Ginzburg–Landau approach, which is valid for temperatures T close to the critical temperature T_c. As was pointed in Ref. 8, the macroscopic interference effects due to coupling of supercurrents in different terminals are not restricted by the special kind of the 4-terminal junction (Fig. 1a). In fact, any mesoscopic 4-terminal weak link will produce a coupling similar to the relation (1). In the present paper, the microscopic theory of the mesoscopic ballistic 4-terminal junction is developed. We consider a Josephson weak coupling through the two-dimensional normal layer which is connected with four bulk superconducting terminals as is shown in Fig. 1b. Such a S-2DEG-S structure was experimentally realized in Ref. 9 for the case of two terminals. It was shown in[9] that this new class of fully phase coherent Josephson junctions demonstrate the nonlocal phase dependence of mesoscopic supercurrents. We study the coherent current states in such a 4-terminal structure within the quasiclassical equations for transport-like Green's functions. The relation between the currents in the different terminals, that is valid for arbitrary temperatures and junction sizes, is obtained. The structure of current carrying states inside the mesoscopic 4-terminal junction is itself of interest. As is well known (see, e.g., Ref. 10), in ballistic Josephson junction with direct conductivity the supercurrent flows through the local Andreev levels. In the multiterminal case considered here, the

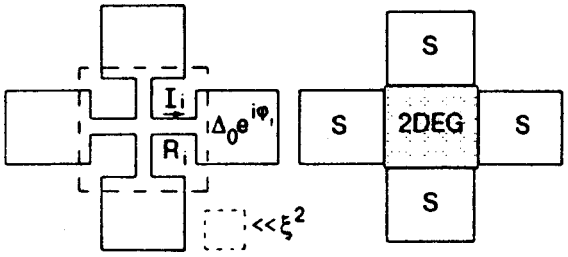

FIG. 1. The superconducting 4-terminal Josephson junction. Four coupled superconducting microbridges, going from a point to the massive superconducting banks (R_i is the normal resistance of the ith filament and $\xi(T)$ is the coherence length) (a). The mesoscopic 4-terminal Josephson junction. Four bulk superconductors are weakly coupled through a rectangular of two-dimensional electron gas (2DEG) (b).

spatial distribution of current density and of the order parameter, and hence the phase-dependent Andreev levels, are determined by the phase differences between all terminals. Thus, they can be regulated by the external control parameters, i.e., the transport currents and (or) the applied magnetic fluxes. In Section 2, we present the description of the system and formulate basic equations and boundary conditions. In Section 3 the current-phase relations analogous to (1) are derived for the cases of small (as compared to the coherence length) and also arbitrary junction sizes. The spatial distributions of the supercurrent density and of the induced order parameter are studied in Section 4.

2. MODEL AND BASIC EQUATIONS

The studied system consists of 4 bulk superconducting banks which are contacted with 4 sides of rectangular two-dimensional ($2D$) normal layer having the length L and width W (see Figs. 1b and 2). The sizes L and W are assumed to be much larger than Fermi wavelength $\lambda_F = h/p_F$. To study the stationary coherent current states in the 4-terminal ballistic junction we use the Eilenberger equations for ξ-integrated Green's functions[11]

$$\mathbf{v}_F \frac{\partial}{\partial \mathbf{r}} \hat{G} + [\omega \hat{\tau}_3 + \hat{\Delta}, \hat{G}] = 0, \tag{2}$$

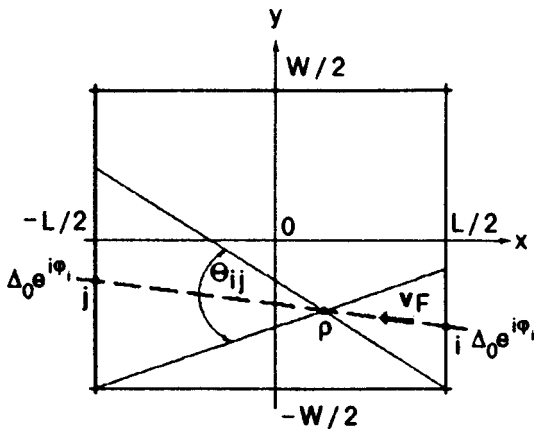

FIG. 2. Dashed line is $i \to j$ trajectory passing through the point ρ. All of this type trajectories are confined in the angle θ_{ij}. L, W are length and width of the rectangular.

where

$$\hat{G}_\omega(\mathbf{v}_F, \mathbf{r}) = \begin{pmatrix} g_\omega & f_\omega \\ f_\omega^+ & -g_\omega \end{pmatrix}$$

is the matrix Green's function, which depends on the Matsubara frequency ω, the electron velocity on the Fermi surface $\mathbf{v}_F$ and the coordinate $\mathbf{r}$;

$$\hat{\Delta} = \begin{pmatrix} 0 & \Delta \\ \Delta^* & 0 \end{pmatrix}$$

is the superconducting pair potential. For the self-consistent off-diagonal potential $\Delta(\mathbf{r})$ and current density $\mathbf{j}(\mathbf{r})$ we have the expressions

$$\Delta(\mathbf{r}) = \lambda 2\pi T \sum_{\omega>0} \langle f_\omega \rangle, \tag{3}$$

$$\mathbf{j}(\mathbf{r}) = -4\pi i e N(0) T \sum_{\omega>0} \langle \mathbf{v}_F g_\omega \rangle. \tag{4}$$

They determine the induced order parameter $\psi \equiv \Delta/\lambda$ and the $2D$ current density in the normal layer; $N(0) = m/2\pi$; $\langle ... \rangle$ is the averaging over directions of $2D$ vector $\mathbf{v}_F$; λ is the constant of electron-phonon coupling.

Equations (2) are supplemented by the values of Δ and Green's functions in bulk banks far from the *SN*-interfaces

$$\hat{\Delta}_i = \Delta_0 (\hat{\tau}_1 \cos\varphi_i - \hat{\tau}_2 \sin\varphi_i),$$

$$\hat{G}_i = \frac{\omega \hat{\tau}_3 + \hat{\Delta}_i}{(\omega^2 + \Delta_0^2)^{1/2}}, \quad i = 1,...4. \tag{5}$$

We solve Eqs. (2) by integrating over the ''transit'' trajectories of the ballistic flight of electrons from one bank to another.[12] These trajectories [characteristics of the differential Eqs. (2)] are straight lines along the direction of electron velocity (see Fig. 2). In the bulk superconducting banks the order parameter can be taken as the constant value (5) up to the *SN*-interface. In contrast to the case of $2D$ banks, these ''rigid'' conditions for Δ[1,12] are valid for arbitrary sizes L and W compared with the coherence length $\xi_0 \sim v_F/\Delta_0$, and not only for L, $W \gg \xi_0$. At the same time, the Green's function along the given transit trajectory varies in a distance of about ξ_0 when approaching the *SN*-interface.

Let us introduce the time of flight along the trajectory, $\mathbf{v}_F \partial/\partial \mathbf{r} \equiv d/dt$, $t_i < t < \infty$, where $t = t_i$ corresponds to the point on ith *SN*-boundary and $t = \infty$ to the point inside the ith bank far from the *SN*-boundary. Then the general solution of Eqs. (2) inside the ith bank satisfying the boundary conditions (5) will be

$$\hat{G}_i(t) = \frac{\omega \hat{\tau}_3 + \hat{\Delta}_i}{\Omega} + C_i [\Delta_0 \hat{\tau}_3 - (\omega \cos\varphi_i + i \,\mathrm{sign}(\mathbf{v}_F \mathbf{n}_i) \Omega \sin\varphi_i) \hat{\tau}_1 + (\omega \sin\varphi_i - i \,\mathrm{sign}(\mathbf{v}_F \mathbf{n}_i) \Omega \cos\varphi_i) \hat{\tau}_2] e^{-2\Omega(t-t_i)}. \tag{6}$$

Here $\mathbf{n}_i$ is the outer normal to the ith side of the rectangular boundary and $\Omega = (\omega^2 + \Delta_0^2)^{1/2}$. The arbitrary constants C_i must be found by matching of Green's functions at in-

coming and out-going points at *SN*-boundaries with the solution inside the normal layer along the trajectory which connects these points (see Fig. 2). We consider here the simplest case when only Andreev reflection[13] occurs at *SN*-interface. In more realistic case, when usual reflection (e.g., due to the potential barrier) or interface roughness are present, more general matching conditions must be used (see Ref. 14).

3. CURRENT-PHASE RELATIONS

Inside the normal layer ($\Delta=0$), the Eilenberger equations can be solved analytically. If we classify the electronic trajectories inside the normal layer according to the sides at which they come in and go out, then the solution of Eq. (2) can be written as

$$\begin{aligned}\hat{G}_{i\to j}(t)=&\frac{\omega}{\Omega}\hat{\tau}_3+\frac{\Delta_0}{\Omega}\{\cosh[2\omega(t-t_i)-i\varphi_i]\hat{\tau}_1\\&-i\sinh[2\omega(t-t_i)-i\varphi_i]\hat{\tau}_2\}+A_{i\to j}\{\Delta_0\hat{\tau}_3\\&-[\omega\cosh(2\omega(t-t_i)-i\varphi_i)]+\Omega\sinh[2\omega(t\\&-t_i)-i\varphi_i]\hat{\tau}_1+i[\Omega\cosh\{2\omega(t-t_i)-i\varphi_i\}]\\&+\omega\sinh[2\omega(t-t_i)-i\varphi_i]\hat{\tau}_2\},\end{aligned}\tag{7}$$

where $\hat{G}_{i\to j}(t)$ is the matrix Green's function along the trajectory originating in the ith side and extending to the jth side (see Fig. 2). We denote this trajectory by $i\to j$. Matching (7) with solution in the banks (6), the corresponding $A_{i\to j}$ is obtained:

$$A_{i\to j}=\frac{(\Delta_0/\Omega)\sinh(\omega t_{ji}+i\varphi_{ji}/2)}{\omega\sinh(\omega t_{ji}+i\varphi_{ji}/2)+\Omega\cosh(\omega t_{ji}+i\varphi_{ji}/2)},\tag{8}$$

where $t_{ji}=t_j-t_i$ and $\varphi_{ji}=\varphi_j-\varphi_i$. From (7) and (8) we have the expression for the matrix Green's function $\hat{G}_\omega(\rho,\mathbf{v}_F)$ as a function of the coordinate $\rho\in\Sigma$ (Σ is the region of $2D$ rectangular weak link) and the direction of $\mathbf{v}_F$. In fact, we can write

$$\hat{G}_\omega(\rho,\mathbf{v}_F)=\hat{G}_{i\to j},\quad\text{for}\quad\mathbf{v}_F\in\theta_{ij}(\rho),\tag{9}$$

where we have introduced $\theta_{ij}(\rho)$ as the angle in which all $i\to j$ trajectories, passing through the point ρ, are confined [see Fig. 2, Eq. (A1) in Appendix]. The diagonal and off-diagonal terms of $\hat{G}_{i\to j}(t)$ have the forms

$$\begin{aligned}g_{i\to j}=&\frac{\omega}{\Omega}+\Delta_0 A_{i\to j}\\=&\frac{\omega\cosh(\omega t_{ji}+i\varphi_{ji}/2)+\Omega\sinh(\omega t_{ji}+i\varphi_{ji}/2)}{\Omega\cosh(\omega t_{ji}+i\varphi_{ji}/2)+\omega\sinh(\omega t_{ji}+i\varphi_{ji}/2)},\end{aligned}\tag{10}$$

$$\begin{aligned}f_{i\to j}=&\left[\frac{\Delta_0}{\Omega}+(\Omega-\omega)A_{i\to j}\right]\exp[-2\omega(t-t_i)+i\varphi_i]\\=&\frac{\Delta_0\exp(\omega t_{ji}+i(\varphi_i+\varphi_j)/2)}{\Omega\cosh(\omega t_{ji}+i\varphi_{ji}/2)+\omega\sinh(\omega t_{ji}+i\varphi_{ji}/2)}\\&\times e^{-2\omega(t-t_i)}.\end{aligned}\tag{11}$$

In the limit $L,\ W\ll\xi_0$ the expressions (10) and (11) for Green's functions are simplified and we have

$$g_{i\to j}=\frac{\omega\Omega+(1/2)i\Delta_0^2\sin(\varphi_{ji})}{\omega^2+\Delta_0^2\cos^2(\varphi_{ji}/2)},\tag{12}$$

$$f_{i\to j}=\frac{\Delta_0}{\Omega\cos(\varphi_{ji}/2)+i\omega\sin(\varphi_{ji}/2)}e^{i(\varphi_i+\varphi_j)/2}.\tag{13}$$

We can obtain the retarded and advanced Green's functions, $\hat{G}^{R,A}(\varepsilon)$, by analytical continuation of Matsubara's Green's function $\hat{G}(\omega)$ [Eqs. (9)–(13)]. The poles of diagonal component of the retarded Green's function, $g^R(\varepsilon,\rho,\mathbf{v}_F)$, determine the energies of local Andreev states in the system. The local density of states in the normal layer is given by the formula

$$\mathcal{N}(\varepsilon,\rho)=N(0)\langle\mathrm{Re}\,g(\omega=-i\varepsilon,\rho,\mathbf{v}_F)\rangle.\tag{14}$$

Using the expressions (9) and (12) and the fact that $\theta_{ij}(\rho)=\theta_{ji}(\rho)$ in the case of a small junction, we obtain

$$\begin{aligned}\mathcal{N}(\varepsilon,\rho,\{\varphi_i\})=&N(0)\sum_{i\neq j}\langle\mathrm{Re}\,g(\omega=-i\varepsilon,\rho,\mathbf{v}_F)\rangle_{\theta_{ij}}\\=&N(0)\sum_{i\neq j}\theta_{ij}(\rho)\mathrm{Re}\,g_{i\to j}(\omega=-i\varepsilon)\\=&N(0)\sum_{i<j}\theta_{ij}(\rho)\mathrm{Re}[g_{i\to j}(\omega=-i\varepsilon)\\&+g_{j\to i}(\omega=-i\varepsilon)]=\pi\Delta_0N(0)\sum_{i<j}\theta_{ij}(\rho)\\&\times\left|\sin\frac{\varphi_{ji}}{2}\right|\delta\left(|\varepsilon|-\Delta_0\cos\frac{\varphi_{ji}}{2}\right).\end{aligned}\tag{15}$$

We can also use Eqs. (9) and (12) to obtain $\langle\mathbf{v}_F g\rangle$ at a point of the ith side ρ_i. Then, the resulting expression can be replaced in Eq. (4) to find the current density $\mathbf{j}(\rho_i)$. The calculation of the current density at the arbitrary point of the normal rectangular will come in the next section and the Appendix. Here we calculate the total current I_i flowing into the ith bank.

Let us start with the case of a small junction ($L,\ W\ll\xi_0$). In order to find I_i, we have to calculate the integral $I_i=\int_{(S_i)}\mathbf{j}(\rho_i)\cdot d\mathbf{s}_i$, where the integral is taken over the ith side of rectangular.

After calculation of $\mathbf{j}(\rho_i)$ from (A3) and (A5) and taking the integral over $d\mathbf{s}_i$, we obtain

$$\begin{aligned}I_i=&\frac{ep_F\Delta_0 d}{2\pi}\sum_{j=1}^{4}\gamma_{ij}\sin\left(\frac{\varphi_i-\varphi_j}{2}\right)\\&\times\tanh\left\{\frac{\Delta_0\cos[(\varphi_i-\varphi_j)/2]}{2T}\right\},\end{aligned}\tag{16}$$

where $d=\sqrt{L^2+W^2}$ and $\gamma_{ij}=\gamma_{ji}$;

$$\gamma_{13}=1-\frac{k}{\sqrt{1+k^2}};\quad\gamma_{24}=1-\frac{1}{\sqrt{1+k^2}};$$

$$\gamma_{12}=\gamma_{14}=\gamma_{23}=\gamma_{34}=\frac{1}{2}\left(\frac{1+k}{\sqrt{1+k^2}}-1\right), \tag{17}$$

are geometrical form factors that depend on the width-to-length ratio $k=W/L$. The positive sign of I_i corresponds to the direction of the current from the normal layer to the ith bank. Note that

$$\sum_{i=1}^{4} I_i=0.$$

The formula (16) for current-phase relations generalizes the expression (1) to the case of a small mesoscopic 4-terminal junction. It follows from (17) that the form factor γ_{ij} cannot be factorized, i.e., presented in the form $\gamma_{ij}=\gamma_i\gamma_j$, in contrast to the case of relation (1), where $\gamma_{ij}=(1/R_i)(1/R_j)$. This essential feature of the current-phase relations reflects the nonlocal nature of the supercurrents in the mesoscopic multi-terminal Josephson junction.

The current-phase relations (16) are valid for arbitrary temperature T. In the limiting cases of $T=0$ and temperature close to T_c the expression (16) takes the forms

$$I_i=\frac{ep_F\Delta_0 d}{2}\sum_{j=1}^{4}\gamma_{ij}\sin\left(\frac{\varphi_i-\varphi_j}{2}\right) \quad \text{for } T=0, \tag{18}$$

$$I_i=\frac{ep_F\Delta_0^2 d}{4\pi T_c}\sum_{j=1}^{4}\gamma_{ij}\sin(\varphi_i-\varphi_j) \quad \text{for } T=T_c. \tag{19}$$

In the case of arbitrary lengths L, W, we restrict the consideration for the temperature close to T_c. In this case current-phase relations similar to the expression (19) can be obtained. The difference is in geometrical form factors. In fact, we have the result

$$I_i=\frac{ep_F\Delta_0^2 d}{4\pi T_c}\sum_{j=1}^{4}\tilde{\gamma}_{ij}(k,L,W)\sin(\varphi_i-\varphi_j), \tag{20}$$

where the generalized form factors are given by

$$\tilde{\gamma}_{41}=\tilde{\gamma}_{21}=\tilde{\gamma}_{23}=\tilde{\gamma}_{43}=\frac{4}{\pi^2\sqrt{1+k^2}}\times\int_{-k/2}^{k/2}dy\int_{-\arctan((k/2)+y)}^{\pi/2}d\theta\cos\theta\times\sum_{n=0}^{\infty}\frac{\exp[-L(k/2+y)(2n+1)/(\xi_N\cos\theta)]}{(2n+1)^2},$$

$$\tilde{\gamma}_{42}=\tilde{\gamma}_{24}\equiv\frac{4}{\pi^2\sqrt{1+k^2}}\int_{-k/2}^{k/2}dy\int_{-\arctan((k/2)+y)}^{\arctan((k/2)-y)}d\theta\cos\theta\times\sum_{n=0}^{\infty}\frac{\exp[-L(2n+1)/(\xi_N\cos\theta)]}{(2n+1)^2}, \tag{21}$$

$$\tilde{\gamma}_{12}=\tilde{\gamma}_{14}=\tilde{\gamma}_{32}=\tilde{\gamma}_{34}=\tilde{\gamma}_{41}(L\to W,W\to L,k\to 1/k),$$

$$\tilde{\gamma}_{13}=\tilde{\gamma}_{31}=\tilde{\gamma}_{42}(L\to W,W\to L,k\to 1/k).$$

Here $\xi_N=v_F/2\pi T$. In the limit $L,\ W\ll\xi_0$, $\tilde{\gamma}_{ij}$ reduce to γ_{ij}.

4. SPATIAL DISTRIBUTION OF SUPERCURRENTS AND INDUCED ORDER PARAMETER

In this section we will obtain the supercurrent density and the induced order parameter at an arbitrary point of the normal layer in the case of a small junction. At the given point of the normal layer $\rho=x\mathbf{i}+y\mathbf{j}$

$$\langle\mathbf{v}_F g\rangle=\sum_{i>j}(\langle\mathbf{v}_F g\rangle_{\theta_{ij}}+\langle\mathbf{v}_F g\rangle_{\theta_{ji}})=i\sum_{i>j}\langle\mathbf{v}_F\rangle_{\theta_{ij}}\frac{\Delta_0^2\sin\varphi_{ji}}{\omega^2+\Delta_0^2\cos^2(\varphi_{ji}/2)}, \tag{22}$$

where we have used $\langle\mathbf{v}_F g\rangle_{\theta_{ij}}=\langle\mathbf{v}_F\rangle_{\theta_{ij}}g_{i\to j}$, $\langle\mathbf{v}_F\rangle_{\theta_{ji}}=-\langle\mathbf{v}_F\rangle_{\theta_{ij}}$ and $g_{j\leftrightarrow i}=g^*_{i\to j}$.

The current density is obtained by replacing (22) in the Eq. (4):

$$\mathbf{j}(\rho)=2\pi eN(0)\Delta_0\sum_{i>j}\langle\mathbf{v}_F\rangle_{\theta_{ij}}\sin\frac{\varphi_{ji}}{2}\times\tanh\left(\frac{\Delta_0\cos(\varphi_{ji}/2)}{2T}\right). \tag{23}$$

The expression (23) describes the spatial distribution of the current density inside the normal layer. In order to find the explicit expression for the coefficients $\langle\mathbf{v}_F\rangle_{\theta_{ij}}$ in Eq. (23), we have to consider four different regions in the normal rectangular and obtain $\mathbf{j}(\rho)$ in each region separately (see Appendix). This calculation has been done in the Appendix and the result for $\mathbf{j}(\rho)$ is given by (A3) and (A5). Here we write Eq. (23) in the more transparent form. Let us introduce $\hat{\theta}_{ij}(\rho)$ as the unit vector in the direction of the $i\to j$ trajectory passing through the bisector of $\theta_{ij}(\rho)$; then $\langle\mathbf{v}_F\rangle_{\theta_{ij}}$ can be written as

$$\langle\mathbf{v}_F\rangle\theta_{ij}=\int_0^{\theta_{ij}}\frac{d\theta}{2\pi}\mathbf{v}_F=\frac{v_F}{\pi}\sin\left(\frac{\theta_{ij}}{2}\right)\hat{\theta}_{ij}. \tag{24}$$

Combining Eqs. (23) and (24), we obtain

$$\mathbf{j}(\rho)=\frac{ep_F\Delta_0}{2\pi}\sum_{i<j}\sin\left(\frac{\theta_{ij}}{2}\right)\hat{\theta}_{ij}(\rho)\times\sin\left(\frac{\varphi_j-\varphi_i}{2}\right)\tanh\left[\frac{\Delta_0\sin[(\varphi_j-\varphi_i)/2]}{2T}\right]. \tag{25}$$

The distribution of the induced order parameter can be obtained in a way similar to what we have done for $\mathbf{j}(\rho)$. In this case we need to calculate the average of off-diagonal element of the matrix Green's function, $f_\omega(\mathbf{v}_F,\rho)$, in the direction of $\mathbf{v}_F$:

$$\langle f\rangle=\sum_{i\neq j}\langle f\rangle_{\theta_{ij}}=\sum_{i\neq j}\theta_{ij}(\rho)f_{i\to j}. \tag{26}$$

Replacing (26) in (3) and after the calculation, we obtain for $\psi(x,y)=\Delta(x,y)/\lambda$:

$$\psi(x,y)=\frac{\Delta_0}{\lambda}\sum_{i=1}^{4}\theta_i(x,y)e^{i\varphi_i}. \tag{27}$$

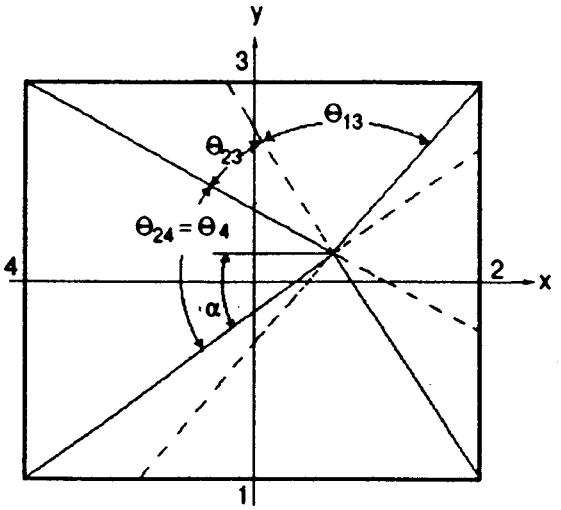

FIG. 3. The angles θ_{ij} for a point in the region II. We have just shown θ_{13}, θ_{23}, $\theta_{24}=\theta_4$ and also the angle α.

Here $\theta_i(x,y)$ is the angle by which ith side is seen from the point $\rho\equiv(x,y)$. The angles $\theta_i(x,y)$'s are given by the relations

$$\begin{aligned}\theta_1&=\pi-\alpha(x,y)-\alpha(-x,y),\\ \theta_2&=\alpha(-x,-y)+\alpha(-x,y),\\ \theta_3&=\pi-\alpha(x,-y)-\alpha(-x,-y),\\ \theta_4&=\alpha(x,y)+\alpha(x,-y),\end{aligned}\tag{28}$$

where the angle

$$\alpha(x,y)=\arctan\left(\frac{k/2+y}{1/2+x}\right)\tag{29}$$

is a function of the coordinate (normalized by L) and is shown in Fig. 3. Equation (27) expresses the fact that, inside the ballistic normal layer region, the linear superposition of four macroscopic wave functions (pair potentials) of the banks occurs, where the weight of wave function of the ith bank is determined by the geometrical factor $\theta_i(x,y)$.

5. CONCLUSIONS

The present study considers a 4-terminal microstructure based on a new class of mesoscopic Josephson junctions[9] which are fully phase coherent and have comparable width and length. The microscopic theory of the stationary coherent current states in ballistic multiterminals is developed.

We have calculated the current-phase relations (CPR), i.e., the total currents in each terminal as functions of the phases of the superconducting order parameter in all the banks. These relations describe the behavior of the system influenced by the external transport currents or the applied magnetic fluxes. The essential difference between the CPR for mesoscopic [expression (19)] and conventional (relation (1)) 4-terminals consists in the structure of the coefficients of coupling γ_{ij}. In the mesoscopic case considered here these coefficients cannot be factorized (presented in the form $\gamma_{ij}=\gamma_i\gamma_j$ for all indexes i, j and arbitrary value of the width-to-length ratio $k=W/L$. Here we only outline the new effect,

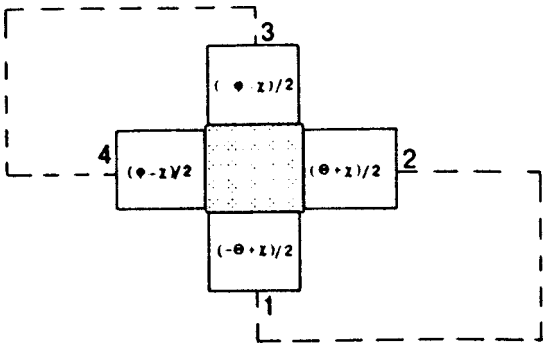

FIG. 4. A configuration of the mesoscopic 4-terminal Josephson junction. The terminals *1* with *2* and *3* with *4* are short-circuited by the superconducting rings (dashed lines). The phase differences are $\theta=\varphi_2-\varphi_1$, $\varphi=\varphi_3-\varphi_4$, $\chi=(\varphi_1+\varphi_2)/2-(\varphi_3+\varphi_4)/2$.

specific for the mesoscopic 4-terminal junction, which follows from such nonlocal coupling of the currents. Let us consider the configuration shown in Fig. 4. By using the CPR (19) with γ_{ij} given by (17), it can be shown that an applied magnetic flux through one of the rings produces magnetic flux in the other ring even in the absence of an external flux through the other one. The detailed theory of this effect will be reported in a separate publication.

The physical properties of the interior of the mesoscopic 4-terminal junction are of interest by themselves. The above calculated local density of Andreev states, the current density and the order parameter distributions depend on the phase differences between the four terminals and can be regulated by the applied magnetic fluxes. In particular, for some values of the phases φ, θ and χ (see Fig. 4) the ''vortex state'' inside the mesoscopic $2D$ weak link exists. Figures 5 and 6 present the plots for distributions of the absolute value of the induced order parameter and the supercurrent density in the case $\theta=\pi/2$, $\varphi=3\pi/2$, $\chi=0$. The studying of the structure of induced order parameter and local density of states, as well as the dynamical behavior of the system will be the object of further investigation.

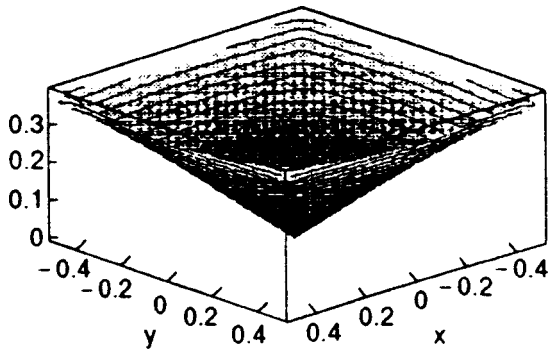

FIG. 5. Absolute value of the induced order parameter $|\psi(x,y)|$ is plotted vertically for the values of phase differences $\theta=\varphi_2-\varphi_1=\pi/2$, $\varphi=\varphi_3-\varphi_4=3\pi/2$, $\chi=(\varphi_1+\varphi_2)/2-(\varphi_3+\varphi_4)/2=0$. The lines of $|\psi(x,y)|=$const are shown.

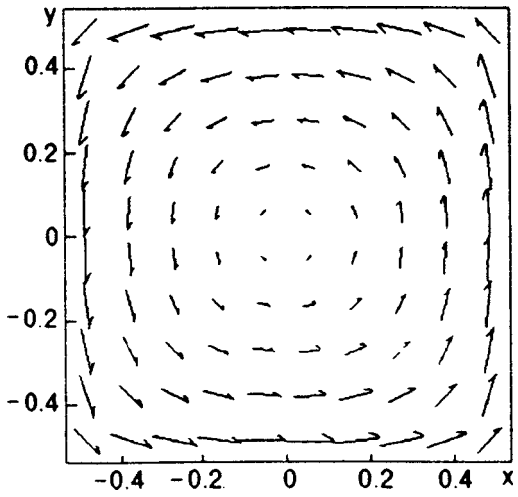

FIG. 6. Vector field plot of the supercurrent density, $\mathbf{j}(x,y)$, inside the normal layer. The values of phase differences are the same as in Fig. 5.

ACKNOWLEDGMENTS

The authors would like to acknowledge support for this research from the Institute for Advanced Studies in Basic Sciences at Zanjan, Iran. We acknowledge to R. de Bruyn Ouboter and I. O. Kulik for usefull discussions.

APPENDIX

In this Appendix we present expressions for the angles θ_{ij} and the vectors $\langle \mathbf{v}_F \rangle_{\theta_{ij}}$. Using the expressions given here, one can calculate the density of states $\mathcal{N}$ and the current density $\mathbf{j}$ [see Eqs. (15) and (23)].

According to the classification of the trajectories in term of origin and destination sides, there are 12 different types of trajectories which are $1\to2$, $1\to3$, $1\to4$, $2\to3$, $2\to4$, $3\to4$ and the corresponding reverse of these trajectories. For a given point, depending on the position, some of these trajectories do not take place. In this respect we can consider four different regions in the normal rectangular:

I, where $y<0, |y|>k|x|$, ($2\to3$, $3\to4$ and their reversed are absent);
II, where $x\geqslant 0$, $|y|\leqslant kx$ ($1\to4$, $3\to4$ and their reversed are absent),
III, where $y\geqslant 0$, $y>k|x|$ ($1\to2$, $1\to4$ and their reversed are absent)
and
IV, where $x<0$, $|y|\leqslant kx$ ($1\to2$, $2\to3$ and their reversed are absent).

At the given point ρ, for the absent trajectories we have $\theta_{ij}=0$, and consequently the corresponding term in the expressions of $\mathcal{N}$ and $\mathbf{j}$ [Eqs. (15) and (23)] will vanish. We shall calculate $\mathbf{j}$ at the given point of the region II and then introduce the exchange rules of arguments to obtain it in other regions. Consider a point in region II; the possible (non-vanishing) θ_{ij} are drawn in Fig. 6 and can be expressed in terms θ_i's (given by (28) and (29)) as

$$\theta_{12}=\tfrac{1}{2}(\theta_1+\theta_2-\theta_3-\theta_4),$$
$$\theta_{13}=\tfrac{1}{2}(\theta_1-\theta_2+\theta_3+\theta_4), \tag{A1}$$
$$\theta_{23}=\tfrac{1}{2}(-\theta_1+\theta_2+\theta_3-\theta_4), \quad \theta_{24}=\theta_4.$$

Also we can use the relation $\langle \mathbf{v}_F \rangle_{\theta_{ij}}=\int (d\theta/2\pi) v_F(\mathbf{i}\cos\theta+\mathbf{j}\sin\theta)$ to obtain

$$\langle \mathbf{v}_F \rangle_{\theta_{12}}(x,y)=\frac{v_F}{2\pi}\{\sin[\alpha(-x,-y)]-\sin[\alpha(x,y)]]\mathbf{i}+[\cos[\alpha(x,y)]-\cos[\alpha(-x,-y)]]\mathbf{j}\},$$
$$\langle \mathbf{v}_F \rangle_{\theta_{13}}(x,y)=\frac{v_F}{2\pi}\{\sin[\alpha(-x,y)]-\sin[\alpha(-x,-y)]]\mathbf{i}+[\cos[\alpha(-x,y)]+\cos[\alpha(-x,-y)]]\mathbf{j}\}, \tag{A2}$$
$$\langle \mathbf{v}_F \rangle_{\theta_{23}}(x,y)=\frac{v_F}{2\pi}\{\sin[\alpha(x,-y)]-\sin[\alpha(-x,y)]]\mathbf{i}+[\cos[\alpha(x,-y)]-\cos[\alpha(-x,y)]]\mathbf{j}\},$$
$$\langle \mathbf{v}_F \rangle_{\theta_{24}}(x,y)=\frac{v_F}{2\pi}\{-\sin[\alpha(x,y)]+\sin[\alpha(x,-y)]]\mathbf{i}+[\cos[\alpha(x,y)]-\cos[\alpha(x,-y)]]\mathbf{j}\},$$

where $\alpha(x,y)$ is given by Eq. (29). The corresponding relations, valid for other regions, can be obtained from (A1) and (A2), using the appropriate rules of index and coordinate exchange (see below). Replacing Eqs. (A1) and (A2) in (23), we obtain for current density in a point of region II

$$\mathbf{j}_{II}(x,y)=[-\mathbf{k}(x,y)+\mathbf{l}(x,y)]P_{13}+[-\mathbf{k}(-x,-y)-\mathbf{k}(x,y)]P_{12}-[\mathbf{k}(x,y)+\mathbf{l}(-x,-y)]P_{24}+[\mathbf{l}(-x,-y)-\mathbf{l}(x,y)]P_{23}, \tag{A3}$$

where

$$\mathbf{k}(x,y)=\sin\alpha(x,y)\mathbf{i}-\cos\alpha(x,y)\mathbf{j},$$
$$\mathbf{l}(x,y)=\sin\alpha(-x,y)\mathbf{i}+\cos\alpha(-x,y)\mathbf{j}, \tag{A4}$$

and $P_{ij}=(ep_F\Delta_0/2\pi)\sin(\varphi_{ji}/2)\tanh[\Delta_0\cos(\varphi_{ji}/2)/2T]$. The current density in other regions is obtained from j_{II} by applying the following rules of phase and coordinate exchange:

$$\mathbf{j}_I=\mathbf{j}_{II}(x\to -y/k, y\to x/k, k\to 1/k;\quad \mathbf{i}\to-\mathbf{j},\quad \mathbf{j}\to-\mathbf{i};$$
$$\varphi_1\to\varphi_4,\varphi_2\to\varphi_1,\varphi_3\to\varphi_2,\varphi_4\to\varphi_3),$$
$$\mathbf{j}_{III}=\mathbf{j}_{II}(x\to y/k, y\to -x/k, k\to 1/k;\quad \mathbf{i}\to\mathbf{j},\mathbf{j}\to-\mathbf{i};$$
$$\varphi_1\to\varphi_2,\varphi_2\to\varphi_3,\varphi_3\to\varphi_4,\varphi_4\to\varphi_1),$$
$$\mathbf{j}_{IV}=\mathbf{j}_{II}(x\to -x, y\to -y, k\to k;\quad (\mathbf{i}\to-\mathbf{i},\mathbf{j}\to-\mathbf{j});$$
$$\varphi_1\to\varphi_3,\varphi_2\to\varphi_4,\varphi_3\to\varphi_1,\varphi_4\to\varphi_2). \tag{A5}$$

The same relations as (A5) can be used for θ_{ij} and $\langle \mathbf{v}_F \rangle_{\theta_{ij}}$ (the phase exchanges have to be replaced by corresponding index exchanges).

*E-mail: omelyanchouk@ilt.kharkov.ua

[1] K. K. Likharev, Rev. Mod. Phys. **51**, 146 (1979).
[2] I. O. Kulik, A. N. Omelyanchouk, and E. A. Kel'man, Fiz. Nizk. Temp. **5**, 118 (1979) [Sov. J. Low Temp. Phys. **5**, 55 (1979)].
[3] E. D. Vol and A. N. Omelyanchouk, Fiz. Nizk. Temp. **20**, 107 (1994) [Low Temp. Phys. **20**, 87 (1994)].
[4] A. Barone and G. Paterno, *Physics and Applications of the Josephson Effect*, Wiley, New York (1982).
[5] R. de Bruyn Ouboter, A. N. Omelyanchouk, and E. D. Vol, Physica B **205**, 153 (1995); *ibid.* **239**, 203 (1997).
[6] B. J. Vleeming, A. V. Zakarian, A. N. Omelyanchouk, and R. de Bruyn Ouboter, Physica B **226**, 253 (1996); Czech. J. Phys. **46**, S5 2823 (1996).
[7] B. J. Vleeming, PhD thesis, Leiden University (1998).
[8] R. de Bruyn Ouboter, A. N. Omelyanchouk, and E. D. Vol, Fiz. Nizk. Temp. **24**, 1017 (1998) [Low Temp. Phys. **24**, 767 (1998)]; Los Alamos archive cond-mat/9805174.
[9] J. P. Heida, B. J. van Wees, T. M. Klapwijk, and G. Borghs, Phys. Rev. B **57**, R5618 (1998).
[10] P. F. Bagwell, R. Riedel, and L. Chang, Physica B **203**, 475 (1994).
[11] G. Eilenberger, Z. Phys. **214**, 195 (1968).
[12] I. O. Kulik and A. N. Omelyanchouk, Fiz. Nizk. Temp. **4**, 296 (1978) [Sov. J. Low Temp. Phys. **4**, 142 (1978)].
[13] A. F. Andreev, Zh. Éksp. Teor. Fiz. **46**, 1823 (1964) [Sov. Phys. JETP **19**, 1228 (1964)].
[14] A. N. Omelyanchouk, R. de Bruyn Ouboter, and C. J. Muller, Fiz. Nizk. Temp. **20**, 501 (1994) [Low Temp. Phys. **20**, 398 (1994)].

This article was published in English in the original Russian journal. It was edited by R. T. Beyer.

LOW-TEMPERATURE MAGNETISM

Resonant magnetic properties of gadolinium–gallium garnet single crystals

A. R. Bedyukh, V. V. Danilov, A. Yu. Nechiporuk, and V. F. Romanyuk

*Taras Shevchenko University, 252022 Kiev, Ukraine**

(Submitted April 28, 1998; revised October 12, 1998)
Fiz. Nizk. Temp. **25**, 249–251 (March 1999)

The results of experimental investigations of resonant magnetic properties of gadolinium–gallium garnet (GGG) single crystals at temperatures 4.2–300 K in the frequency range 1.6–9.3 GHz are considered. It is found that magnetic losses in GGG are determined by the initial splitting of energy levels for gadolinium ions in the garnet crystal lattice and by the dipole broadening. The width and shape of the electron paramagnetic resonance (EPR) line in the GGG crystal, whose asymmetry is manifested most strongly at low frequencies, can be explained by the influence of these factors. Magnetic losses in GGG increase with frequency and upon cooling. It is found that the EPR linewidth increases considerably with decreasing temperature due to the presence of rapidly relaxing impurities.
[S1063-777X(99)00503-4]

Single crystals of GGG $Gd_3Ga_5O_{12}$ are widely used as substrates for growing epitaxial films of magnetic garnets of various compositions. For instance, epitaxial films of yttrium–iron garnet (YIG) $Y_3Fe_5O_{12}$ and gallium-substituted YIG form the material basis of instruments used in spin-wave electronics in the microwave range.

In spite of the fact that the influence of magnetic properties of a GGG substrate on damping and dispersion of magnetostatic spin waves (MSW) in a wide temperature range was considered by us earlier,[1–3] a detailed complex investigation of GGG magnetic losses and their origin has not been carried out so far. In this communication, a refined information on magnetic resonant properties of indigenous GGG crystals grown by the Czochralski technique.

The permittivity and permeability of monocrystalline GGG samples were studied on the basis of the standard resonator technique. The sensitivity of the method was improved due to original instruments recording the variation of resonator parameters and allowing us to detect spontaneous variation of frequency to within 50 kHz and of the *Q*-factor to within 2%.[4] The permittivity measurements were made at a frequency of 9.3 GHz in a resonator with E_{020} type oscillations, while the permeability was measured in a resonator with H_{011} type oscillations for samples of size $2\times2\times75$ mm and $2\times1\times75$ mm.

The real component μ' of permeability of the GGG single crystal was 1.075 ± 0.001 in zero external magnetic field and 1.079 ± 0.001 for $H_0=5$ kOe; the permittivity of the GGG in the frequency range under investigation was $\varepsilon=13.1\pm0.1$.

The field dependences of magnetic losses μ'' in the frequency range $f=1.62-2.90$ GHz (see Fig. 1) were studied at room temperature on a radiospectrometer RE1301 modified for the operation in the required frequency range.

At a frequency of 9.3 GHz, the magnetic losses μ'' of the GGG single crystal were determined at room temperature and liquid nitrogen temperature, while the EPR linewidth ΔH was measured in the temperature range 4.2–300 K. The field dependences of μ'' in this frequency range are shown in Fig. 2. Figures 1 and 2 also show the $\mu''(H_0)$ dependences from Ref. 5 (curves *5* and *3* respectively). First of all, we note the presence of absorption in zero external magnetic field and clearly manifested asymmetry of absorption curves, which is observed up to frequencies of the order of 10 GHz. On the other hand, the magnetic losses at liquid nitrogen temperature are approximately four times larger than the losses at room temperature (curve *2* in Fig. 1).

DISCUSSION OF RESULTS

In order to clarify the origin of magnetic losses in GGG, we must take into account, first, the structure of energy levels of Gd^{3+} ions in the garnet crystal lattice, and second, their dipole–dipole interaction.

In spite of the fact that a free Gd^{3+} ion has zero orbital angular momentum in the ground state, the initial magnetic ($H_0=0$) splitting up to 8.5 GHz takes place in the crystal lattice of garnets due to partial mixing with other states. Naturally, the strong dipole–dipole interaction of Gd^{3+} ions in a $Gd_3Ga_5O_{12}$ crystal transforms this system of energy levels into a continuous band which is responsible for initial losses and asymmetry of the EPR line at low frequencies and small values of the applied magnetic field. Thus, dipole broadening amounting to ~3 GHz makes a significant contribution to the EPR linewidth along with the initial splitting. With increasing frequency (and hence the applied magnetic field), both these factors gradually generate a broad EPR line which is indeed observed in experiments.

The temperature dependence of the normalized EPR linewidth of a GGG plate having a size 0.5×5 mm and a

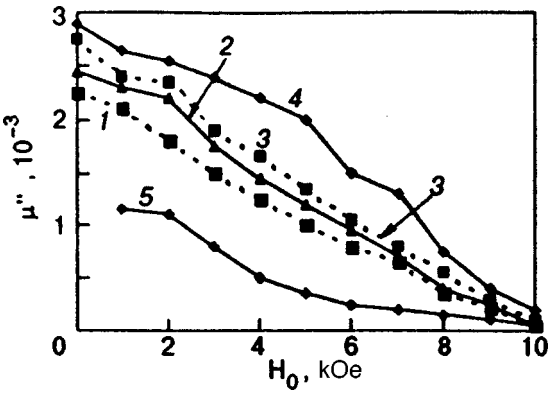

FIG. 1. Magnetic losses in GGG single crystals at room temperature at frequencies 1.62 (curve *1*), 1.89 (curve *2*), 2.25 (curve *3*), and 2.90 GHz (curve *4*); curve *5* corresponds to the results obtained in Ref. 5 (at a frequency of 2.1 GHz).

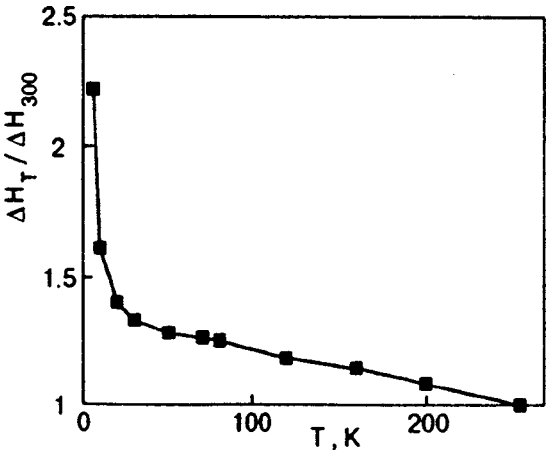

FIG. 3. Temperature dependence of normalized EPR linewidth of a GGG monocrystalline plate at a frequency of 9.3 GHz.

thickness of 400 μm is shown in Fig. 3 (the linewidth at room temperature is $\Delta H \simeq 3$ kOe). It is interesting to note that the resonant EPR field did not change in the entire temperature range and amounted to 3.1–3.2 kOe. A considerable increase in the linewidth upon cooling (approximately to $\Delta H \simeq 6.7$ kOe at liquid helium temperature) can be explained by the fact that we used gadolinium oxide with a purity of 99.5% to synthesize the GGG single crystal for our experiments. The presence of accompanying impurities of rare-earth ions creates a spin-lattice relaxation channel for Gd^{3+} ions, whose efficiency increases upon cooling.[6] The presence of impurities is apparently also responsible for slightly higher values of μ'' for the samples under investigation as compared with the data obtained by Adam et al.[5] at room temperatures.

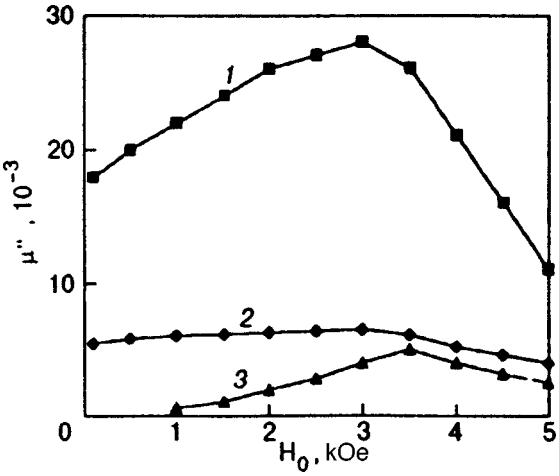

FIG. 2. Magnetic losses in GGG single crystals at a frequency of 9.3 GHz at liquid nitrogen temperature (curve *1*) and at room temperature (curve *2*) in comparison with the results obtained in Ref. 5 at room temperature (curve *3*).

In conclusion, the authors are pleased to thank S. M. Ryabchenko, Corresponding Member of the National Academy of Sciences of the Ukraine, for his help in carrying out this research and for fruitful discussions of the results.

*E-mail: chipa@boy.rpd.univ.kiev.ua

[1] V. V. Danilov, D. L. Lyfar', Yu. V. Lyubon'ko, *et al.*, Izv. Vuzov, Fizika **32**, 48 (1989).
[2] M. G. Balinskiĭ, V. V. Danilov, and A. Yu. Nechiporuk, Radiotekh. Elektron. **38**, 1319 (1993).
[3] V. V. Danilov, A. Yu. Nechiporuk, and L. V. Chevnyuk, Fiz. Nizk. Temp. **22**, 1052 (1996) [Low Temp. Phys. **22**, 802 (1996)].
[4] D. D. Pilipko, V. F. Romanyuk, and E. N. Smirnov, Pribory i Tekh. Éksp. No. 5, 150 (1983).
[5] J. D. Adam, J. H. Collins, and D. I. Cruikshank, in *Proceedings 21 Annual Conf. Magn. and Magn. Mater*, Philadelphia (1976)p. 643.
[6] A. G. Gurevich, *Magnetic Resonance in Ferrites and Ferromagnets* [in Russian], Nauka, Moscow (1973).

Translated by R. S. Wadhwa

Exotic solitons in magnets with strongly anisotropic exchange interaction

A. S. Kovalev

B. Verkin Institute for Low Temperature Physics and Engineering, National Academy of Sciences of the Ukraine, 310164 Kharkov, Ukraine[*)]

M. V. Gvozdikova

Kharkov State University, 310077 Kharkov, Ukraine

(Submitted September 18, 1998)
Fiz. Nizk. Temp. **25**, 252–262 (March 1999)

Exotic magnetic solitons (compactons and peakons) in magnets with extremely anisotropic exchange interaction are investigated on the basis of the classical Ising and XY-models. © *1999 American Institute of Physics.* [S1063-777X(99)00603-9]

INTRODUCTION

Intense studies of nonlinear dynamic physical systems during the last 40 years have resulted in the formation of a new trend in theoretical and mathematical physics, viz., the theory of solitons.[1,2] As applied to the solid state physics, the investigation of soliton dynamics in magnetically ordered media is of special interest.[3,4] Owing to a variety of structural and physical properties, magnets can exhibit nonlinear localized excitations of various types, such as magnetic solitons and vortices, domain walls, and magnetization rotation waves.[3,4] These systems are also interesting due to the fact that some models in the theory of magnetism are completely integrable, and the results of classical analysis permit a comparison with the results of investigations of some one-dimensional quantum-mechanical models.

At the same time, the objects of investigation were mainly simple $1D$ models in the long-wave limit (on the basis of differential equations). This made it possible to construct explicitly the solution for various types of magnetic solitons in ferro- and antiferromagnets, ferrites, and spin glasses, and to carry out their classification. However, the theoretical results obtained for one-dimensional models permit a comparison with experimental results only in the case of quasi-one-dimensional magnetic systems. A large number of such compounds have been synthesized recently, among which the traditional quasi-one-dimensional ferromagnet $CsNiCl_3$,[5] new one-dimensional ferromagnets $[(CH_3)_3NH]NiCl_3\cdot 2H_2O$, $(C_9H_7NH)NiCl_3\cdot 1.5H_2O$,[6] layered antiferromagnets $(CH_2)_n(NH_3)_2MnCl_4$, $(C_nH_{2n+1})\times(NH_3)_2MnCl_4$,[7–11] and most of HTSC compounds in the stoichiometric phase and their isostructural analogs are worth mentioning. In view of an anomalously weak interaction between layers, every magnetically ordered plane in the latter case of layered compounds can be regarded as an effective spin and the array of layers as a model $1D$ spin system with a weak exchange interaction.

However, actual low-dimensional magnets possess, as a rule, peculiar physical properties differing from the magnetic properties of $3D$ compounds. Above all, a large number of such magnets are essentially discrete in a magnetic respect, and their description on the basis of differential equations, i.e., systems with distributed parameters, is unjustified. The discreetness of a magnetic subsystem is determined by the relation between the exchange interaction energy ($E_{ex}\sim JS^2/a^2$, where J is the exchange interaction constant, S the unit cell spin, and a the atomic spacing) and the one-ion anisotropy energy ($E_a\sim\beta S^2$, where β is the one-ion anisotropy constant). This relation involves the so-called ''magnetic length'' $l_0=\sqrt{J/\beta}$ determining the characteristic size of the region of nonuniform distribution of magnetization. In the case of a weak exchange interaction (or large anisotropy), the value of l_0 becomes of the order of atomic spacing a: $l_0\sim a(J\sim\beta a)$, and the system becomes essentially discrete in magnetic respect. The ratio $J/\beta a$ for the above compounds can attain values of the order of or much smaller than unity (e.g., $J/\beta a\sim 1$ for HTSC compounds, where J is the interlayer exchange[12]), while this ratio for compounds investigated in Refs. 7–11 attains the value of 10^{-2} for large numbers n. It was proved in Refs. 13–15 that the structure and dynamics of nonlinear localized excitations (solitons and domain walls) in such discrete systems changes significantly: they become compact and assume a collinear form.

On the other hand, low-dimensional magnets in some cases exhibit a considerable anisotropy of exchange interaction (g-factor anisotropy), while most theoretical (classical) models take into account, as a rule, only one-ion or weak exchange anisotropy. The actual anisotropy of exchange can be of the order of the exchange interaction itself. For example, the g-factor anisotropy in the compounds $KDy(MoO_4)_2$ and $KEr(MoO_4)_2$ is of the order of 10^1.[16,17] In this case, we can introduce several magnetic lengths $l_i=\sqrt{J_i/\beta}$ associated with intensities of exchange interaction for different spin components. In extremely anisotropic cases, when some components of this interaction vanish, we arrive at the classical Ising model or the XY model. It was proved by us earlier[4,18,19] that the structure of magnetic solitons and domain walls in this limit also changes considerably. Among other things, their ''compactization'' and the formation of exotic nonlinear local excitations (compactons and peakons) also become possible.

In spite of the apparent difference between the above

two circumstances, they possess the following property in common: the dispersion of elementary excitations (spin waves) may become anomalously small in systems with exchange interaction comparable with one-ion anisotropy as well as in systems with an anisotropy of exchange interaction comparable with the exchange itself. In a narrow sense of the word, dispersion is defined as $D=d^2\omega(k)/dk^2$, where $\omega=\omega(k)$ is the energy-momentum relation for elementary excitation. It was found that $D\sim J$ for systems with an isotropic exchange interaction, $D\sim J_x=J_y\ll J_z$ for an Ising magnet with the preferred z-axis, while $D\sim\sqrt{J_x}J_z k$ ($J_z\ll J_x,J_y$) in the XY model with the same symmetry. Thus, the dispersion of linear waves becomes weak for J, $J_i<\beta$.

It is well known that the reason behind the existence of nonlinear localized excitations is the competition of the system nonlinearity and its spatial dispersion.[2] For this reason, the form of the energy-momentum relation $\omega=\omega(k)$ for linear waves affects significantly the properties of soliton states. Rosenau[20,21] was the first to pay attention to the relation between the existence of compact solitons and the absence of dispersion of linear waves. He proposed a new version of the Korteweg–de Vries (KdV) equation with a nonlinear dispersion term and obtained compact soliton solutions with a stationary profile. At the same time, Kosevich[22,23] also considered compact envelope solitons in nondispersve media. Later, Holm and Kamassa (1994) proposed their own modification of the KdV equations permitting for a certain value of velocity (corresponding to the vanishing of dispersion) a soliton solution with a peculiar exotic profile, which was called a peakon. A semiclassical interpretation of exotic solitons (compactons and peakons) was proposed by us recently.[18,19]

In this paper, we consider a uniaxial ferromagnet with one-ion and exchange anisotropies in the limit of strong exchange anisotropy (Ising and XY magnets) and of one-ion anisotropy of the easy-axis and easy-plane type on the basis of the classical one-dimensional Heisenberg model. All possible types of solutions for compactons and peakons are obtained for domain walls, dynamic magnetic solitons, and magnetization rotation waves.

1. FORMULATION OF THE MODEL AND EQUATIONS OF MAGNETIZATION DYNAMICS

Let us consider a uniaxial ferromagnet with exchange and one-ion anisotropies of the same symmetry, whose energy density in the $1D$ case has the form[3]

$$E=\frac{J}{2}\left(\frac{\partial\mathbf{M}}{\partial x}\right)^2+\frac{J_1}{2}\left(\frac{\partial M_z}{\partial x}\right)^2-\frac{\beta}{2}M_z^2, \tag{1}$$

where $\mathbf{M}$ is the magnetization vector, $J_x=J_y=J$, $J_z=J+J_1$ are the exchange interaction constants along the corresponding axes, and β is the constant of one-ion anisotropy associated with the z-axis ($\beta>0$ for an easy-axis ferromagnet and $\beta<0$ for an easy-plane ferromagnet).

The equations of magnetization dynamics (Landau–Lifshitz equation) in the angular variables θ and φ specifying the orientation for the vector $\mathbf{M}=M_0$ ($\sin\theta\cos\varphi$, $\sin\theta\sin\varphi$, $\cos\theta$) have the form[3]

$$\sin\theta\frac{\partial\theta}{\partial t}=-\frac{2\mu_0}{\hbar M_0}\frac{\delta E}{\delta\varphi},\quad \sin\theta\frac{\partial\varphi}{\partial t}=\frac{2\mu_0}{\hbar M_0}\frac{\delta E}{\delta\theta}, \tag{2}$$

where M_0 is the nominal magnetization and μ_0 Bohr's magneton. In fact, Eqs. (2) are Hamilton equations for canonically conjugate quantities φ and M_z.

For the special case of uniaxial ferromagnet with the energy density (1), Eqs. (2) assume the form

$$[l^2+(L^2-l^2)\sin^2\theta]\frac{\partial^2\theta}{\partial x^2}-\left[\sigma+l^2\left(\frac{\partial\varphi}{\partial x}\right)^2-(L^2-l^2)\times\left(\frac{\partial\theta}{\partial x}\right)^2\right]\sin\theta\cos\theta+\frac{1}{\omega_0}\sin\theta\frac{\partial\varphi}{\partial t}=0, \tag{3}$$

$$l^2\frac{\partial}{\partial x}\left(\sin^2\theta\frac{\partial\varphi}{\partial x}\right)-\frac{1}{\omega_0}\sin\theta\frac{\partial\theta}{\partial t}=0, \tag{4}$$

where we have introduced the notation for the homogeneous ferromagnetic resonance frequency $\omega_0=2\mu_0 M_0|\beta|/\hbar$; $l^2=J/\beta$; $L^2=(J+J_1)/\beta$ and the sign coefficient σ equal to $+1$ or -1 for the easy-axis and easy-plane cases, respectively.

The system of equations (3) and (4) can be written in the form of a single equation in the complex quantity $\Psi=(M_x+iM_y)/M_0$:

$$i\frac{\partial\Psi}{\partial t}-l^2m\frac{\partial^2\Psi}{\partial x^2}+L^2\Psi\frac{\partial^2 m}{\partial x^2}+\sigma m\Psi=0, \tag{5}$$

where $m=\sqrt{1-|\Psi|^2}$ is the dimensionless z-component of magnetization, and time is measured in the units of $1/\omega_0$.

It should be noted that we have used the phenomenological expression for energy (1), which implies that the long-wave approximation ($\partial/\partial x\ll 1/a$) is valid for static solutions if the inequalities $J_x,J_z\gg\beta a^2$ ($l,L\gg a$) are satisfied. However, we proceed from the discrete Hamiltonian with the exchange interaction $E_{\mathrm{ex}}=-\Sigma_{i,n}J_i M_i^n M_i^{n+1}/a^2$, where n is the number of the lattice site spin, we must substitute $\beta-(J_x-J_z)/a^2$ for β in Eq. (1) in the long-wave limit. In this case, the long-wave approximation is valid when the inequalities $J_x,J_z\gg\beta a^2-(J_x-J_z)$ are satisfied. In other words, in extremely anisotropic cases with $J_x=J_y=0$ (Ising's limit) and $J_z=0$ (the XY limit), this approximation holds for close values of one-ion anisotropy and nonzero exchange interaction component. (Conversely, in the case of an isotropic exchange interaction the system becomes essentially discrete (see above), and the long-wave approach is inapplicable.)

Equations (3)–(5) and their soliton solutions were analyzed completely only for a ferromagnet with an isotropic exchange interaction for which $L=l$. In this case, the system becomes completely integrable[3,4] both in the easy-axis and the easy-plane cases, and all soliton solutions of Eq. (5) have an explicitly analytic form: domain walls and dynamic magnetic solitons can exist in an easy-axis ferromagnet, while dynamic solitons and magnetization rotation waves can be observed in an easy-plane ferromagnet.[3,4] In the general case for $L\neq l$, soliton solutions for an easy-axis ferromagnet can be presented implicitly in terms of elliptic integrals[3] or analyzed numerically.[24] To our knowledge, soliton states with $L\neq l$ in the easy-plane case have not been investigated.

2. MAIN TYPES OF SOLITON EXCITATIONS IN A FERROMAGNET

The classification of soliton excitations of a uniaxial ferromagnet is determined essentially by the type of one-ion anisotropy since the nature of the ground state of the system changes with its sign. The ground state of an easy-axis ferromagnet is doubly degenerate and corresponds to a configuration with $m=\pm 1$, while the ground state in an easy-plane ferromagnet, which corresponds to $m=0$, is degenerate continuously in the phase of the complex function Ψ. As a result, the spectra of spin waves in these two cases differ significantly.

In an easy-axis magnet ($\sigma=1$), the spectrum of nonlinear spin waves with $\Psi \simeq \exp[i(\omega t-kx)]$ has the form

$$\omega = m(1+k^2l^2). \tag{6}$$

The dispersion of these waves is $D=2ml^2$. We see that the dispersion of spin waves in the Ising limit ($J_x=J_y=0$, $l=0$) vanishes. On the other hand, in the limit of the XY model ($J_z=0$) the dispersion vanishes (together with frequency) at a definite amplitude of the spin wave $\Psi_0=1$ ($m=0$). In a reference frame moving with the group velocity $V=2mkl^2$, the energy-momentum relation for linear waves (with $m=1$), i.e.,

$$\tilde{\omega} = 1-\frac{V^2}{4l^2} \tag{7}$$

defines the range of soliton solutions on the $(\tilde{\omega},V)$ plane: $\omega<\tilde{\omega}(V)$. In the Ising limit ($l=0$), this region collapses into a line $\omega<1, V=0$, and hence only stationary domain walls (as in the case of an isotropic exchange interaction) and stationary magnetic solitons exist. On the other hand, the region of existence of solitons in the XY model ($L=0$) is the same as for an isotropic exchange, but the line $\tilde{\omega}<0, V=0$ becomes singular (the dispersion vanishes on it).

In the isotropic case ($L=l$), domain walls correspond to the point $\omega=0, V=0$, and the relevant solution is well known:

$$m = \tanh\frac{x}{l}, \tag{8}$$

while the simplest solution for a stationary magnetic soliton ($V=0$) has the form[3,4]

$$m = 1-\frac{2(1-\omega)}{\omega\sinh^2(x/l\sqrt{1-\omega})+1}, \quad \omega>0,$$

$$m = 1+\frac{2(1-\omega)}{\omega\cosh^2(x/l\sqrt{1-\omega})-1}, \quad \omega<0. \tag{9}$$

In the case of an easy-plane one-ion anisotropy ($\sigma=-1$), linear spin waves have the following energy-momentum relation:

$$\omega = lk\sqrt{1+L^2k^2}. \tag{10}$$

With such a dispersion relation, the group velocity and dispersion have the form

$$V = l(1+2L^2k^2)(1+L^2k^2)^{-1/2},$$

$$D = L^2lk(3+2L^2k^2)(1+L^2k^2)^{-3/2}.$$

It can be seen that the dispersion vanishes in the Ising ($l=0$) and XY ($L=0$) limits. Besides, the group velocity also vanishes in the Ising limit. In a reference frame moving with the group velocity, the dispersion relations $\tilde{\omega}=\tilde{\omega}(V)$ for linear waves can be written implicitly in the form

$$\tilde{\omega} = -lL^2\frac{k^3}{\sqrt{1+L^2k^2}}, \quad V = l\frac{1+2L^2k^2}{\sqrt{1+L^2k^2}}. \tag{11}$$

The parabolas

$$\tilde{\omega} \simeq -(2/3)^{3/2}(V-l)^{3/2}/L\sqrt{l}$$

corresponding to (11) and the segment ($\tilde{\omega}=0$, $|V|<l$) bound the region of existence of dynamic magnetic solitons on the $(\tilde{\omega},V)$ plane. It follows from (11) that in the Ising limit this region ''collapses'' into a line ($V=0$, $\omega<0$), and hence only stationary solitons exist. The range of dynamic solitons in the XY model is bounded by the straight lines ($\omega=0$, $|V|<l$) and ($V=\pm l$, $\omega<0$).

In the case of an isotropic exchange interaction ($L=l$), the segment ($\tilde{\omega}=0$, $|V|<l$) corresponds to magnetization rotation waves for which the solution has the form[3,4]

$$\Psi = \tanh\xi + i(V/l)\frac{1}{\cosh\xi}, \quad m = \frac{\sqrt{1-V^2/l^2}}{\cosh\xi}, \tag{12}$$

where $\xi=\sqrt{1-V^2/l^2}(x-Vt)/l$.

Solutions for dynamic solitons exist in the entire range of parameters under parabolas (11) and the line of magnetization rotation waves, and are cumbersome even in the case of a stationary center of mass of such a wave[3,4]:

$$m = \frac{2\sinh(\kappa x/l)\sin\omega t(\kappa^2-1)}{(\kappa^2-1)\sinh^2(\kappa x/l)+\kappa^2-\sin^2\omega t},$$

$$\Psi = \frac{(\kappa^2-1)\sinh^2(\kappa x/l)-\kappa^2+\sin^2\omega t}{(\kappa^2-1)\sinh^2(\kappa x/l)+\kappa^2-\sin^2\omega t} + i\frac{2\kappa\sqrt{\kappa^2-1}\sinh(\kappa x/l)\cos\omega t}{(\kappa^2-1)\sinh^2(\kappa x/l)+\kappa^2-\sin^2\omega t}, \tag{13}$$

where $|\omega|=\kappa\sqrt{\kappa^2-1}$.

Let us consider the transformation of magnetic solitons, domain walls, and magnetization rotation waves in ferromagnets with extremely anisotropic exchange interaction.

3. EXOTIC SOLITONS IN AN EASY-PLANE FERROMAGNET

3.1. Compactization of localized excitations in an easy-axis Ising magnet

The magnetization dynamics in an easy-axis ferromagnet with anisotropic exchange interaction is described by the system of equations (3) and (4) with $\sigma=+1$. For soliton solutions of the general form

$$\theta = \theta(x-Vt), \quad \varphi = \Psi(x-Vt)+\tilde{\omega}t \tag{14}$$

Eq. (4) is integrable. Using the relation between Ψ and θ and integrating Eq. (3) we obtain[3]

$$\frac{d\theta}{dx}\sqrt{l^2+(L^2-l^2)\sin^2\theta}$$

$$=2\tan\frac{\theta}{2}\sqrt{\cos^4(\theta/2)-(V/2l)^2-\tilde{\omega}\cos^2(\theta/2)}. \quad (15)$$

This first-order equation permitting the integration in quadratures and analysis on the phase plane can be conveniently written in terms of the variable m:

$$\left(\frac{dm}{dx}\right)^2=(1-m)^2\frac{(1+m)(1-2\tilde{\omega}+m)-(V/l)^2}{(L^2-l^2)(1-m^2)+l^2}. \quad (16)$$

In the case of an isotropic exchange interaction ($L=1$), Eq. (16) can be reduced to

$$l^2\left(\frac{dm}{dx}\right)^2=(1-m)^2\left[(1+m)^2-2\tilde{\omega}(1+m)-\left(\frac{V}{l}\right)^2\right]. \quad (17)$$

The phase profile of this equation is shown in Fig. 1a. The standard separatrix loop *1* here corresponds to a solution of the general form (in particular, solution (9) for $\tilde{\omega}>0$), separatrices *2* and *2′* correspond to solution (8) for a domain wall with $\omega=0, V=0$, while separatrix loop 3 corresponds to solution (9) for a magnetic soliton with negative frequency.

In the limit of Ising ferromagnet for which $l\to 0$ (it was proved above that $V\to 0$ and $V/l\to 0$ in this case), Eq. (16) is transformed as follows:

$$(1-m^2)\left[L^2\left(\frac{dm}{dx}\right)^2+(m-\omega)^2-(1-\omega)^2\right]=0. \quad (18)$$

Its phase profile differs significantly from the same for Eq. (17) and is presented in Fig. 1b. It consists of ellipse *1* for positive-frequency solitons, half an ellipse *2* or *2′* for domain walls of different signs with $\omega=0$, and a part of an ellipse and a segment of the straight line $m=-1$ (loop *3*) for negative-frequency solitons. (It should be noted that the amplitudes of a stationary soliton in a ferromagnet with an isotropic exchange interaction and in an Ising magnet coincide: $m(x=0)=-1+2\omega$. It follows from (15) that in the general case this quantity is independent of the parameter L and l also for $V=0$.)

The solution of Eq. (18) for positive-frequency solitons ($\omega>0$) has the simple form[4]

$$m=\omega-(1-\omega)\cos(x/L), \quad |x|<\pi L,$$

$$m=1, \quad |x|>\pi L, \quad (19)$$

and its profile is shown in Fig. 2a.

Comparing this soliton solution with solution (9), we see that the amplitude is proportional to the quantity $(1-\omega)$ as before, which is typical of dynamic solitons, but the localization region is now independent of frequency and fixed: $\Delta=2\pi L$.

The most interesting property of the obtained solution is that $m\equiv 1$ in the regions $|x|>\pi L$, and all variations of the magnetization field are concentrated in a finite region of space. Later, such solutions were called ''compactons.''[20,21] The physical reason behind the existence of such exotic excitation is as follows: since the dispersion of linear waves is

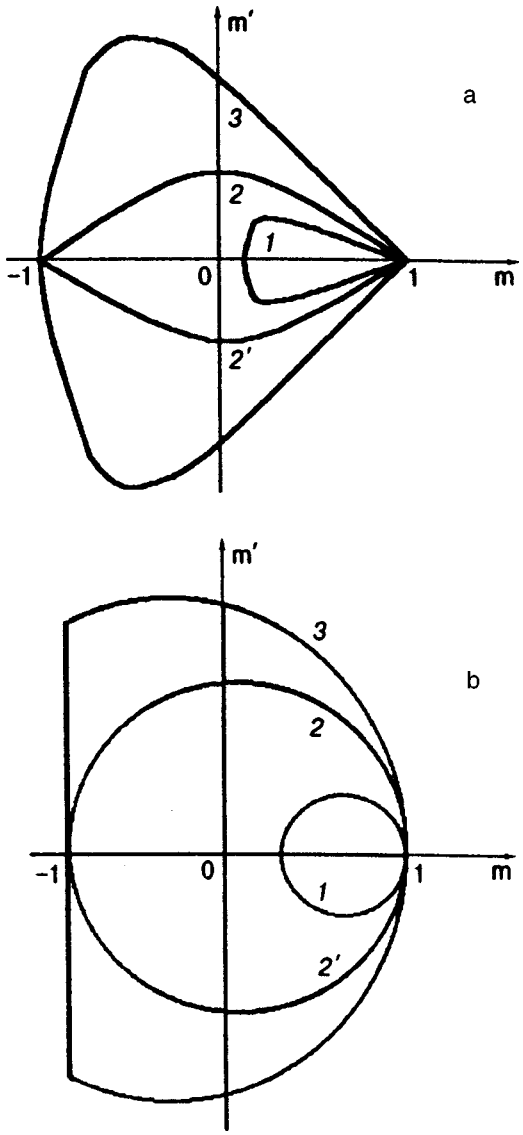

FIG. 1. Phase profiles of dynamic solitons and domain walls in the case of an easy-axis magnet with an isotropic exchange interaction (a) and an easy-axis magnet with Ising exchange interaction (b). Curves *1*, *2* and *3* correspond to positive-frequency solitons, domain walls, and negative-frequency solitons respectively.

equal to zero in the limiting case under investigation, the asymptotes of a localized solution with $m\to 0$ at infinity (for $|x|\to\infty$) can only be identically equal to zero. However, at the center of a localized excitation, where the amplitude differs from zero, nonlinear dispersion terms in the equation are responsible for the dispersion of a nonlinear wave.

The following two circumstances should be noted in this connection. First, the compacton solution (19) can be expressed in terms of a trigonometric function which is usually a solution of the linear equation. (Indeed, the factor in brackets in (18) is the integral of the linear equation $L^2m_{xx}+m=\omega$.) However, the amplitude of the solution is not arbitrary, but is a certain function of frequency, as is usually the case in nonlinear equations.

Second, although solution (19) is ''sewn'' from several function and is a piecewise solution, the function $m(x)$ itself and its first derivative are continuous function. Moreover,

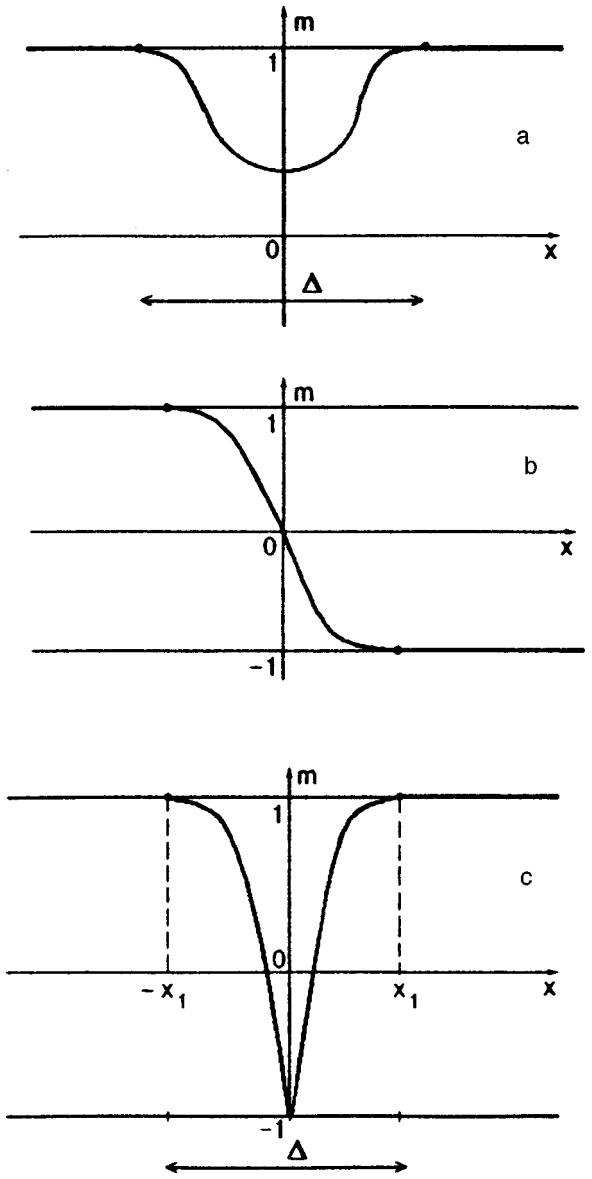

FIG. 2. Profiles for a dynamic compacton with positive (a) and negative (c) frequencies and for a compact domain wall (b) in an Ising easy-axis magnet.

solution (19) is a limit (for $l\to 0$) of the analytic function without any singularities. For example, a small-amplitude soliton with $1-m\ll 1$ in a magnet with $l/L\ll 1$ and $V=0$ can be described by the approximate equation

$$4L^2\left(\frac{du}{dx}\right)^2=u^2\frac{2(1-\omega)-u^2}{l^2/2L^2+u^2} \tag{20}$$

for the function $u=\sqrt{1-m}$. Solution (20), which is analytic in the entire region of space, has the following implicit form[18,19]:

$$\frac{x}{L}=\frac{1}{\sqrt{A}}\ln\frac{\sqrt{A}-f}{\sqrt{A}+f}-\arcsin\frac{f^2-1}{f^2+1}, \tag{21}$$

where $A=(2L/l)^2(1-\omega)$ and

$$f=\left[\frac{4L^2(1-\omega)-2L^2(1-m)}{l^2+2L^2(1-m)}\right]^{1/2}.$$

In the limit $\omega=0$, the soliton solution (19) is transformed into the solution for a domain wall[4]:

$$\begin{aligned} &m=1, \quad x>\pi L/2,\\ &m=\sin(x/L), \quad |x|<\pi L/2,\\ &m=-1, \quad x<-\pi L/2 \end{aligned} \tag{22}$$

(see Fig. 2b). This solution also has the form of a compacton, but a topological one. It corresponds to separatrices *2* and *2′* in Fig. 1b. A solution of this type was recently obtained by Remussine *et al.* for the mechanical model proposed by them. It can be seen from (19) and (22) that the width of a compact domain wall is equal to half the width of a dynamic compacton.

Finally, for negative frequencies of magnetization precession in a soliton, the solution also has the compacton form:

$$\begin{aligned} &m=-|\omega|-(1+|\omega|)\cos[(x+x_0)/L], \quad 0<x<x_1,\\ &m=1, \quad x>x_1, \end{aligned} \tag{23}$$

where $x_0=\arccos[(1-|\omega|)/(1+|\omega|)]$, $x_1=L\pi-x_0$ and $m(x)=m(-x)$ (see Fig. 2c).

In this case, however, solution (23) has a derivative jump at the center of a soliton. But the amplitude of the solution is not arbitrary and is equal to a quite definite value of $m=-1$, the value $m=-1$ being a solution of the nonlinear equation (18). Nevertheless, the derivative of the angular variable θ at zero has a singularity: $d\theta/dx\approx 4\sqrt{|\omega|}/\sqrt{Lx(1+|\omega|)}$, and the long-wave approach becomes meaningless at this point. However, solution (23) is the limit of the analytic solution of Eq. (16) with $l\ll L$ for $l\to 0$ as in the previous case. Such a behavior is typical of so-called peakons (see below), and hence negative-frequency solitons in the Ising limit are combinations of a compacton and a peakon.

In contrast to positive-frequency solitons, the region of localization in negative-frequency solitons is not fixed and depends on frequency: $\Delta=2L(\pi-\arccos[(1-|\omega|)/(1+|\omega|)])$. As $|\omega|\to\infty$, the solution is transformed to the point-like singularity. At large frequencies, the frequency dependence of the soliton width $\Delta\simeq 4L/\sqrt{|\omega|}$ is the same as in the case of an isotropic magnet for which $\Delta\simeq 4l/\sqrt{|\omega|}$.

Finally, let us consider the relation between integrals of motion of compactons. Besides the energy (1) which has the form

$$E=\frac{\beta}{2}\int_{-\infty}^{\infty}dx\left(L^2\left(\frac{dm}{dx}\right)^2-(m^2-1)\right), \tag{24}$$

in the Ising limit, the system possesses an additional integral of motion, viz., the total number of spin deviations

$$N=\int_{-\infty}^{\infty}dx(1-m). \tag{25}$$

The frequency dependence of the compacton energy and the number of bound magnons in the compacton are described by the formulas

$$E=\beta\pi L(1-\omega^2), \quad \omega>0, \tag{26}$$

$$E=\beta L\left[(1-\omega^2)\left(\pi-\arccos\frac{1-|\omega|}{1+|\omega|}\right)+2(1+|\omega|)\sqrt{|\omega|}\right],$$

$$\omega<0$$

and

$$N=2\pi L(1-\omega),\quad \omega>0, \tag{27}$$

$$N=2L(1+|\omega|)\left[\pi-\arccos\frac{1-|\omega|}{1+|\omega|}-\frac{2\sqrt{|\omega|}}{1+|\omega|}\right],$$

$$\omega<0.$$

These formulas lead to the relation $dE/dN=\beta\omega$ typical of soliton solutions, and the dependences $E=E(\omega)$ and $N=N(\omega)$ resemble qualitatively the same dependences for magnets with isotropic exchange.[3] However, in contrast to conventional solitons in magnets with an isotropic exchange interaction, for which the value of N increases indefinitely as $\omega\to 0$, the value of $N(\omega=0)=2\pi L$ in the given case remains finite (as in the case of magnets with biaxial one-ion anisotropy). The relation between integrals of motion has the following simplest form for positive-frequency compactons:

$$E=\beta N-\frac{\beta}{4\pi L}N^2. \tag{28}$$

This dependence is unusual and differs from the standard relation $E=\beta N-O(N^3)$ for small-amplitude solitons. However, corrections to energy quadratic in the number N are typical of anharmonic oscillators. Thus, compactons possess certain properties of such an isolated anharmonic oscillator in view of their extraordinarily strong localization. (For negative-frequency solitons, formulas (26) and (27) lead to the asymptotic dependence $E=E(N)$ for large values of $|\omega|$: $E\simeq 14\beta L^2/N$, which is in qualitative agreement with a similar asymptotic form for solitons in a magnet with an isotropic exchange: $E\propto\beta l^2/N$.)

3.2. Localized excitations in an easy-axis *XY* ferromagnet

Let us consider the other limiting case of anisotropy of exchange interaction of the XY-type, for which $L=0$. In this case, Eq. (16) can be simplified as follows:

$$l^2m^2\left(\frac{dm}{dx}\right)^2=(1-m)^2[m^2+2m(1-\tilde\omega)+(1-2\tilde\omega-(V/l)^2)]. \tag{29}$$

For small deviation of the soliton parameters from the dispersion relation for linear waves, the small-amplitude soliton has the standard form

$$m\approx 1-[1+(V/2l)^2]\frac{\xi}{2\cosh^2(\sqrt{\xi}(x-Vt)/l)}, \tag{30}$$

where $\xi=1-(V/2l)^2-\tilde\omega$. However, the solution is modified significantly in the vicinity of the parabola $\tilde\omega=1/2-V^2/(2l^2)$ on which m vanishes at the center of the soliton.

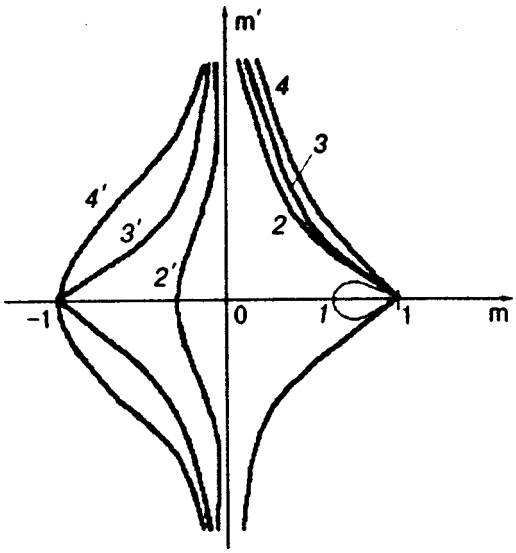

FIG. 3. Phase profiles of dynamic solitons and domain walls in an easy-axis XY ferromagnet for $\tilde\omega>1/2$ (curve *1*), $0<\tilde\omega<1/2$ (curves *2,2′*), $\tilde\omega=0$ (curves *3,3′* for a domain wall), and $\tilde\omega<0$ (curves *4,4′*).

On this curve, the function $m(x)$ has a singularity at zero: $m(x)\approx[3|x|\sqrt{1-\tilde\omega}/(\sqrt{2}l)]^{2/3}$, although the quantity Ψ remains smooth: $1-\Psi^2\sim(|x|/l)^{4/3}$. In the entire range of parameters $\tilde\omega<1/2-V^2/(2l^2)$, the profile of the soliton solution has singularities at the points $\pm x_*$, where the quantity m vanishes: $m\approx\pm[2\sqrt{2\tilde\omega-1}|x-x_*|/l]^{1/2}$. In this case, the function $\Psi(x)$ exhibits a jump at these points in the derivative: $\Psi\approx 1-\sqrt{2\tilde\omega-1}|x-x_*|/l$. Let us analyze qualitatively this solution on the curve ($V=0$, $\tilde\omega<1/2$), i.e., for stationary solitons. The phase profile of the system is depicted in Fig. 3, where the separatrix loop *1* corresponds to the soliton solution with $\tilde\omega>1/2$, while solutions with $0<\tilde\omega<1/2$, $\tilde\omega=0$, and $\tilde\omega<0$ correspond to curves *2,2′*, *3,3′*, and *4,4′*, respectively. The profiles of the functions $m(x)$ and $\Psi(x)$ are shown in Fig. 4. It can be seen that the solution with $\tilde\omega=0$ corresponds to a 180° domain wall. However, the profile of this wall in the case under consideration is unusual. Equation (5) in this limit has the following simple form:

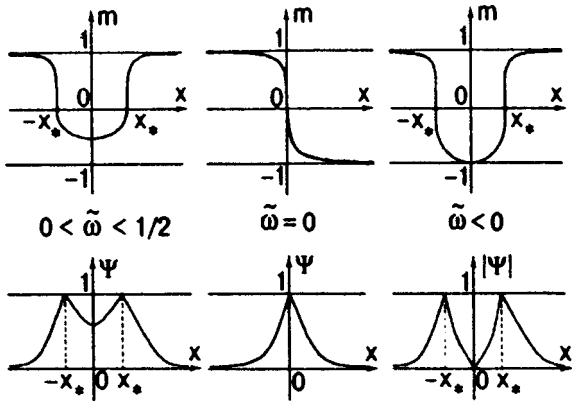

FIG. 4. Profiles of the functions $m(x)$ and $\Psi(x)$ for a domain wall and dynamic solitons with different frequencies in an easy-axis magnet in the XY model.

$$\sqrt{1-\Psi^2}\left(l^2\frac{d^2\Psi}{dx^2}-\Psi\right)=0. \tag{31}$$

The phase profile of this equation for domain walls is a peculiar separatrix in the form of a triangle $\Psi'=\pm\Psi/l$, $\Psi=1$. Such a phase picture is typical of peakon states (see Refs. 18 and 19). In this case, the solution has the form

$$\Psi(x)=\exp(-|x|/l), \tag{32}$$

typical of peakons. As in the case of compactons, the solution can be expressed in terms of the function (exponential in the given case) which is usually a solution of the linear equation. However, in the case of a peakon the nonlinearity is manifested in that the amplitude is not arbitrary but fixed. It can be seen from Fig. 4 that a soliton solution of the general type with $\tilde{\omega}<1/2$ is a bound state of two peakons (like an ordinary magnetic soliton which is the bound state of two domain walls). However, in the general case $\tilde{\omega}\neq 0$, the solution cannot be expressed in terms of exponential functions. For example, in the limit $|\tilde{\omega}|\gg 1$, the soliton solution can be represented in the implicit form

$$\mathrm{Arctanh}\frac{\sqrt{m+1}}{\sqrt{2}}-\sqrt{2}\sqrt{m+1}=\sqrt{|\tilde{\omega}|}\frac{x}{l}. \tag{33}$$

This formula shows that the solution is smooth at the center of the soliton, where $m=-1$, and has a vertical tangent at the points $x_*=\pm l(\mathrm{Arctanh}(1/\sqrt{2})-\sqrt{2})/\sqrt{|\tilde{\omega}|}$ where $m=0$.

4. EXOTIC SOLITONS IN AN EASY-PLANE FERROMAGNET

4.1 Magnetization rotation waves in an easy-plane Ising magnet

In an easy-plane ferromagnet with anisotropic exchange interaction, the magnetization dynamics is described by Eqs. (3) and (4) with $\sigma=-1$, but solutions for dynamic solitons do not have the simple form (14) as in the easy-axis case, which follows from the explicit form of solution (13) even in the case of isotropic exchange. For this reason, we consider only the limiting case of an Ising ferromagnet with an easy-plane one-ion anisotropy. For $l=0$, Eq. (4) implies that $\theta=\theta(x)$ and is independent of time. This is in accord with the conclusion concerning the absence of mobile excitations, which follows from the dispersion relation (11) for linear magnons in the limit $l=0$. Moreover, it follows from Eq. (3) that the variable φ can only be a linear function of time, which is impossible for localized excitations with a fixed orientation of magnetization in the easy plane at infinity (for $x\to\pm\infty$).

Thus, In the limit of an Ising magnet, only one type of localized excitations is possible, i.e., stationary magnetization rotation waves. However, for this type of excitations Eq. (3) is solvable in the general case of an arbitrary anisotropy of exchange interaction also. For $\varphi=\mathrm{const}$, after the first integration we have

$$L^2\left(\frac{dm}{dx}\right)^2=m^2\frac{1-m^2}{1-m^2+(l/L)^2m^2}. \tag{34}$$

In the Ising limit, this equation can be reduced to the following trivial equation:

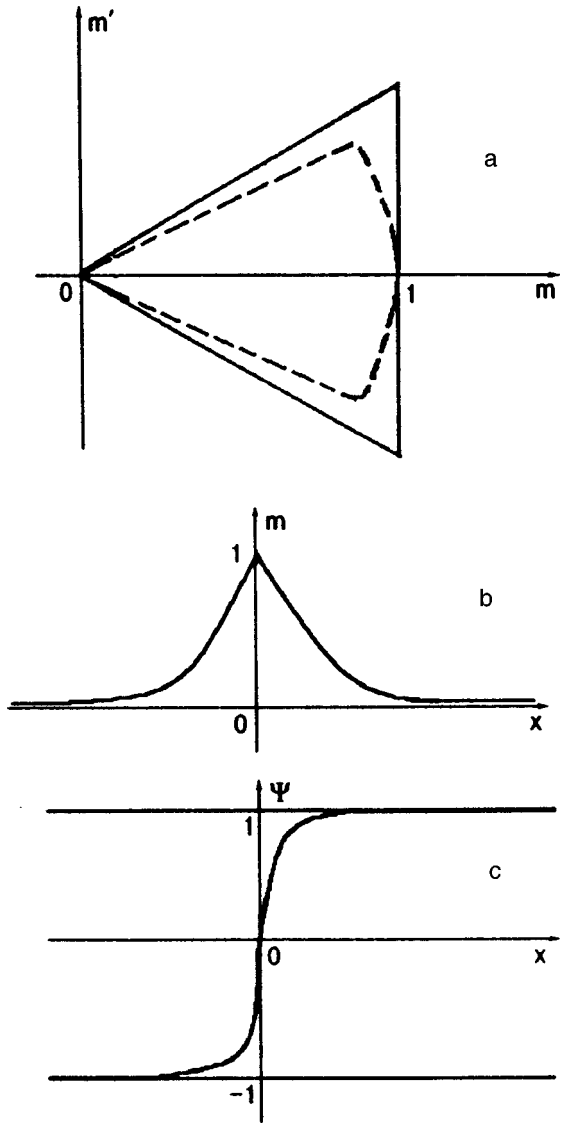

FIG. 5. Phase picture (a) and profiles of the coordinate dependence for different magnetization components (b and c) corresponding to a magnetization rotation wave of the peakon type in an easy-plane Ising ferromagnet. The dashed curve corresponds to the phase picture of a localized wave taking into account weak exchange interaction between the X- and Y-components of the spins.

$$(1-m^2)\left[L^2\left(\frac{dm}{dx}\right)^2-m^2\right]=0. \tag{35}$$

The phase profile of the separatrix loop on the plane $(dm/dx,m)$ in this case degenerates into the triangle $L(dm/dx)=\pm m$, $m=1$ (see solid triangle in Fig. 5a). As in the case of compactons in an easy-axis Ising magnet, Eq. (35) is again connected with the first integral of motion of a linear equation (in the brackets), but with the factor $(1-m^2)$ which just determines the nonlinearity of the solution. It can be expressed in terms of exponential functions (as in the case of a linear equation):

$$m=\exp(-|x|/L), \tag{36}$$

but the amplitude of the solution is fixed: $m(0)=1$. Since

Eq. (35) has an additional solution $m \equiv 1$, the exponential functions can be sewn at the center of the magnetization rotation wave.

Solution (36) has a typical for of an exotic soliton (peakon) and is presented in Fig. 5b. In contrast to the magnetization rotation wave (12) in an isotropic magnet with $m = 1/\cosh(x/l)$, the peakon width depends on the magnetic length L, ant it has a ''peak'' at the center. The function $\Psi(x)$ in this case is defined as $\Psi = \pm\sqrt{1-\exp(-2|x|/L)}$ and has an infinite derivative at zero in contrast to the solution $\Psi = \tanh(x/l)$ for an isotropic magnet (see Fig. 5c). Although the peakon solution has a singularity at zero, it is a limit of an analytic function. It can be seen from Eq. (34) that the separatrix loop corresponding to a soliton for $l \neq 0$ is smooth on the phase plane (dashed curve in Fig. 5a), and solution (34) can be written in an analytic, although implicit, form:

$$\frac{x}{L} = \ln\left(\frac{1-G}{1+G}\right) - B\ln\left[\left(\frac{1}{G}-B\right)^2(1-m^2)\right], \tag{37}$$

where $B = \sqrt{1-l^2/L^2}$ and $G = \sqrt{(1-m^2)/(1-B^2m^2)}$.

A comparison of Figs. 4 and 5 shows that the profiles of the domain wall in an easy-axis XY magnet and magnetization rotation waves in an Ising magnet have the same appearance under the substitution $l \leftrightarrow L$ and $\Psi \leftrightarrow m$. In other words, there exists an ''invariance'' associated with simultaneous change in the symmetry of exchange and one-ion anisotropy.

4.2. Compact waves of magnetization rotation in an easy-plane *XY* magnet

Let us consider the case of an easy-plane ferromagnet with exchange anisotropy of the XY type ($L = 0$). Apparently, dynamic solitons with $\tilde{\omega} < 0, V < l$ and magnetization rotation waves with $\tilde{\omega} = 0, V < l$ exist in this limit. However, we could not find the corresponding solutions even under the simplifying assumption that the rotation of magnetization vector occurs, as in the isotropic case, in a fixed plane for a rotation wave and in a rotating plane for a soliton (see solution (13)).

An exception is the limit of a stationary magnetization rotation wave for which Eq. (5) acquires the trivial form

$$m\left(l^2\frac{d^2\Psi}{dx^2} + \Psi\right) = 0, \tag{38}$$

differing from formula (31) in the sign of Ψ.

Equation (38) has a compact solution:

$$\Psi = 1, \quad x > \pi l/2,$$

$$\Psi = \sin\frac{x}{l}, \quad |x| < \pi l/2, \tag{39}$$

$$\Psi = -1, \quad x < -\pi l/2.$$

(In the case of isotropic exchange interaction, the corresponding solution for a magnetization rotation wave has the form $\Psi = \tanh(x/l)$.

Thus, we see that there exists a symmetry of properties of exotic solitons in the case of simultaneous change in the type of exchange and one-ion anisotropy. Compact domain walls and dynamic solitons exist in an easy-axis Ising ferromagnet, while compact waves of magnetization rotation are observed in the XY model of an easy-plane magnet. On the other hand, magnetization rotation waves of the peakon type exist in an easy-plane Ising magnet, and the same peakon domain walls and dynamic solitons can exist in an easy-axis ferromagnet with exchange anisotropy of the XY type.

*)E-mail: kovalev@ilt.kharkov.ua

[1] V. E. Zakharov, S. V. Minakov, S. P. Novikov, and A. P. Pitaevskii, *The Theory of Solitons*, Consultants Bureau, 1984.
[2] A. M. Kosevich and A. S. Kovalev, *Introduction to Nonlinear Physical Mechanics* [in Russian], Naukova Dumka, Kiev (1989).
[3] A. M. Kosevich, B. A. Ivanov, and A. S. Kovalev, *Nonlinear Magnetization Waves. Dynamic and Topological Solitons* [in Russian], Naukova Dumka, Kiev (1983).
[4] A. M. Kosevich, B. A. Ivanov, and A. S. Kovalev, Phys. Rep. **194**, 117 (1990).
[5] A. Achiva, J. Phys. Soc. Jpn. **27**, 561 (1969).
[6] A. G. Anders, V. G. Borisenko, and S. V. Volotskii, Fiz. Nizk. Temp. **15**, 39 (1989) [Sov. J. Low Temp. Phys. **15**, 12 (1989)].
[7] M. I. Kobets, A. A. Stepanov, and A. I. Zvyagin, Fiz. Nizk. Temp. **7**, 1473 (1981) [Sov. J. Low Temp. Phys. **7**, 714 (1981)].
[8] A. I. Zvyagin, M. I. Kobets, V. N. Krivoruchko *et al.*, Zh. Éksp. Teor. Fiz. **89**, 2298 (1985) [Sov. Phys. JETP **62**, 1328 (1985)].
[9] A. I. Zvyagin, V. N. Krivoruchko, V. A. Pashchenko *et al.*, Zh. Éksp. Teor. Fiz. **92**, 311 (1987) [Sov. Phys. JETP **65**, 177 (1987)].
[10] A. A. Stepanov, V. A. Pashchenko, and M. I. Kobets, Fiz. Nizk. Temp. **14**, 550 (1988) [Sov. J. Low Temp. Phys. **14**, 304 (1988)].
[11] A. A. Stepanov, V. A. Pashchenko, and M. I. Kobets, Fiz. Nizk. Temp. **14**, 1114 (1988) [*sic*].
[12] M. M. Bogdan and A. S. Kovalev, Fiz. Nizk. Temp. **16**, 321 (1990) [Sov. J. Low Temp. Phys. **16**, 176 (1990)].
[13] A. N. Goncharuk, A. A. Stepanov, and D. A. Yablonskii, Fiz. Tverd. Tela (Leningrad) **31**, 132 (1989) [Sov. Phys. Solid State **31**, 2099 (1989)].
[14] M. V. Gvozdikova, A. S. Kovalev, and Yu. S. Kivshar', Fiz. Nizk. Temp. **24**, 635 (1998) [Low Temp. Phys. **24**, 479 (1998)].
[15] M. V. Gvozdikova and A. S. Kovalev, Fiz. Nizk. Temp. **24**, 1077 (1998) [Low Temp. Phys. **24**, 808 (1998)].
[16] A. M. Pshisukha, A. I. Zvyagin, and A. A. Stepanov, Fiz. Tverd. Tela (Leningrad) **13**, 3128 (1971) [Sov. Phys. Solid State **13**, 2630 (1971)].
[17] A. M. Pshisukha, A. S. Chernyi, and A. I. Zvyagin, Fiz. Nizk. Temp. **1**, 473 (1975) [Sov. J. Low Temp. Phys. **1**, 233 (1975)].
[18] A. S. Kovalev, in *Nonlinear Physics: Theory and Experiment* (ed. by E. Alfinito, M. Boiti, L. Martina, and F. Pempinelli), World Scientific, Singapore (1997).
[19] A. S. Kovalev and M. V. Gvozdikova, Fiz. Nizk. Temp. **24**, 641 (1998) [Low Temp. Phys. **24**, 484 (1998)].
[20] P. Rosenau and J. Hyman, Phys. Rev. Lett. **70**, 564 (1993).
[21] P. Rosenau, Phys. Rev. Lett. **73**, 1737 (1994).
[22] Yu. A. Kosevich, Phys. Lett. A **176**, 257 (1993).
[23] Yu. A. Kosevich, Phys. Rev. B **47**, 3138 (1993).
[24] J. Tjon and J. Wright, Phys. Rev. B **15**, 3470 (1977).

Translated by R. S. Wadhwa

Chaotic regimes of antiferromagnetic resonance in a quasi-two-dimensional easy-axis antiferromagnet $(NH_3)_2(CH_2)_4MnCl_4$

M. M. Bogdan, M. I. Kobets, and E. N. Khats'ko

B. Verkin Institute for Low Temperature Physics and Engineering, National Academy of Sciences of the Ukraine, 310164 Kharkov, Ukraine)*

(Submitted October 23, 1998)
Fiz. Nizk. Temp. **25**, 263–276 (March 1999)

Chaotic regimes of the microwave energy absorption are observed experimentally and analyzed for two-dimensional metallorganic antiferromagnet $(NH_3)_2(CH_2)_4MnCl_4$ at low temperatures under the conditions of nonlinear antiferromagnetic resonance. Relaxation oscillations of energy absorption are investigated in detail. Their frequency spectra, frequency–amplitude characteristics, and dependences of absorbed power on driving power and static magnetic field are studied. It is shown that the dynamics of relaxation oscillations undergoes a transition to chaos by ''irregular periods.'' Peculiarities of the transition are described consistently. Among other things, the conditions for the emergence of energy absorption regimes with a spike-like and a saw-tooth signal structure are determined, and the characteristics of chaotic oscillations such as the dimensions of strange attractors are calculated. The chaotic dynamics is found to be high-dimensional with a large contribution from noise which is of deterministic origin in the antiferromagnet under investigation. [S1063-777X(99)00703-3]

INTRODUCTION

Chaotic resonant phenomena in magnets have become an object of intense experimental studies in the last decade.[1–19] These investigations were stimulated by the progress made in the mathematical theory of chaos, predicting the universal character of chaotic phenomena irrespective of the character of the physical object being studied and demonstrating a nonlinear behavior.[20–22]

Magnetic compounds possessing the properties required for the emergence of nonlinear oscillations include first of all the crystals exhibiting an extremely weak relaxation of spin excitations. Yttrium–iron garnet (YIG) with a low threshold for a parametric excitation of spin waves even at room temperature has been studied most thoroughly.[1,5,8,9,11–13] Since YIG behaves as a ferromagnet in magnetic respects, nonlinear chaotic effects were studied, as a rule, under the conditions of ferromagnetic resonance (FMR) in transverse as well as longitudinal driving fields.

The total number of investigated nonlinear magnets is not large, and some of them exhibit nonlinear properties only at low temperatures of the order of a few kelvins, at which phonons are frozen out, and their interactions with magnons becomes very weak.

The effective dimensionality of crystals plays an important role for the suppression of relaxation processes. Stepanov *et al.*[14–18] investigated the class of metallorganic compounds that are quasi-two-dimensional ferro- and aniferromagnets in the magnetic respect. It was found that low-dimensional magnets at low temperatures go over to a state with an anomalously low spin–lattice relaxation virtually with a threshold, which makes it possible to excite spin waves parametrically at microwave pumping power of the order of a few milliwatts.[18] Among other things, it was found that in addition to YIG, nonlinear ferromagnetic crystals include metallorganic compounds with a structure similar to the $(CH_3NH_3)_2CuCl_4$ crystal.[19] On the other hand, it was established that chaotic oscillations are generated in the crystals $CuCl_2 2H_2O$,[2] $CsMnF_3$,[6,10] $(CH_2NH_3)_2CuCl_4$.[9] under the conditions of antiferromagnetic resonance (AFMR).

The range of nonlinear effects that have been discovered and thoroughly investigated in ferro- and antiferromagnets is quite large. These include spin-wave instabilities (Suhl instabilities of the first and second order),[23] auto-oscillations of absorbed microwave power,[24,25] and the observation of three known scenarios of a transition to chaos: by period doubling (Feigenbaum scenario), quasiperiodicity, and intermittency.[20–22]

Apart from the interpretation of these nonlinear effects and the determination of the conditions for their observation, it was found that real magnetic crystals can demonstrate a more complex pattern of transition to chaotic regimes in resonance experiments. None of the known scenarios is realized in pure form in such cases,[26] and we must consider new mechanisms of chaotization.[3,5,27]

Hartwik *et al.*[28] were the first to discover long ago the so-called relaxation chaotic oscillations of microwave power in YIG with which a new scenario of a transition to chaos by irregular periods has been associated in last decade.[3,8,9,29] This effect lies in the emergence, instead of purely periodic auto-oscillations, of irregular chaotic bursts of absorbed power in the form of spike-like peaks or pulses with a steep leading front and relaxing rear front under certain conditions of magnetic resonance upon an increase in the pumping power. Theoretical approaches to the description of such

oscillations and mechanisms of their formation were made in Refs. 9, 29, and 30, but a systematic analysis of temporal series of experimental signals as well as of the results of numerical simulation of relaxation oscillations was carried out only recently.[31,32]

In this work, we study experimentally the regimes of chaotic behavior of the microwave power absorbed in a two-dimensional easy-axis antiferromagnet $(NH_3)_2(CH_2)_4MnCl_4$ under the AFMR conditions. This compound is a typical representative of the family of layered Heisenberg antiferromagnets $[NH_3\text{-}(CH_2)_m\text{-}NH_3]MnCl_4$(2CmMn), studied by Stepanov *et al.*[14–18] The structure of these metallorganic crystals is formed by almost quadratic layers of magnetic ions in the octahedral environment of chlorine ions between which long chains of alkylene–ammonia molecules are located. The small value of interlayer exchange associated with a large separation between the spins of adjacent layers leads to a quasi-two-dimensional behavior of these systems. At the temperature $T_N = 42.6\,\mathrm{K}$,[33] the compound 2C4Mn is transformed into antiferromagnetic states with the easy magnetization axis directed at right angles to the planes of the layers. A detailed analysis of linear antiferromagnetic resonance in 2C4Mn revealed[16] that this compound has a four-sublattice noncollinear antiferromagnetic structure with a weak ferromagnetic moment. The antiferromagnetism vector of each layer is deflected successively from the normal to the plane of a layer through an angle of $\pm 16°$ so that the total vector is perpendicular to the layer, and the weak antiferromagnetism vector lies in the layer. According to estimates, the strength of interaction between the layers (26 Oe) is extremely small as compared to both the intralayer exchange ($2H_e \simeq 1360\,\mathrm{kOe}$) and the intralayer uniaxial anisotropy ($H_a \simeq 0.8\,\mathrm{kOe}$) so that 2C4Mn can be regarded as an almost two-dimensional antiferromagnet.

At low temperatures (of the order of a few kelvins), the related compound $(NH_3C_2H_5)_2MnCl_4$(1C2Mn) revealed a number of interesting nonlinear phenomena in the behavior of the absorbed microwave power, e.g., the emergence of periodic auto-oscillations and chaos.[18] Here we carry out a systematic analysis of chaotic regimes of antiferromagnetic resonance in a 2C4Mn crystal. For a driving power below 5 mW at a temperature below 2.18 K, we observed a nonlinear absorption of the microwave field and the emergence of relaxation oscillations with typical (extremely low) average frequencies of the order of a few hertz. These oscillations were recorded and analyzed as temporal series of data with the help of an analog-digital device and computer programs, which made it possible to describe in detail the scenario of a transition to chaos by irregular periods. As a result, we have analyzed qualitative changes in the behavior of temporal series of absorbed power as a function of variation of the parameters of static and varying magnetic fields and carried out the Fourier analysis, obtained the spectra of oscillations, studied the structure of strange attractors of chaotic regimes, and calculated the quantities characterizing chaotic dynamics, i.e., dependences of frequencies of auto-oscillations on the driving power (in particular, we determined their period doubling threshold) and the dimension of chaotic attractors, and discussed the origin and role of noise in relaxation oscillations as well as a possible theoretical model for describing relaxation oscillations in $2D$ antiferromagnets.

EXPERIMENTAL TECHNIQUE

Single crystals of $(NH_3)_2(CH_2)_4MnCl_4$ were grown at room temperature from a saturated aqueous solution in the form of thin rectangular plates with clearly manifested lateral faces and with a typical size $5\times5\times0.3\,\mathrm{mm}$. The compound $(NH_3)_2(CH_2)_4MnCl_4$ possesses a monoclinic symmetry of crystal lattice with the space group $P2_1/b$.[34] Organic chains of $NH_3(CH_2)_4NH_3$ separate two-dimensional, almost square layers of octahedra Mn-Cl_6. The unit cell parameters are $a = 10.77\,\text{Å}$, $b = 7.177\,\text{Å}$, $c = 7.307\,\text{Å}$. Experiments were carried out on a reflection spectrometer with a pumping frequency 70.39 GHz at a temperature below 2.18 K. We used a cylindrical resonator with the Q- factor ~ 1000. The sample was placed in the resonator region with predominant parallel polarization of external static and rf fields $H \| h$.

In resonance experiments, the field is usually applies along the easy axis of the crystal. With such an orientation, the splitting of AFMR branches follows the law

$$\omega_{\pm} = \gamma\{\sqrt{(2H_E + H_A H_A} \pm H\}. \tag{1}$$

For the frequency mentioned above, the resonance conditions are satisfied for the lower frequency branch ω_-, which was observed in our experiments. The maximum power of the source was 5 mW. The applied magnetic field was scanned along the contour of the AFMR line, and the driving power was varied from 0 to $-20\,\mathrm{dB}$. The magnetic field orientation relative to the anisotropy axis and equilibrium directions of antiferromagnetism vectors in adjacent planes also varied. It was found that the most intense absorption corresponds to the symmetric orientation of the field along the crystallographic axis b.

In all experiments, low-frequency modulation of electromagnetic field of frequency 50 Hz was observed. This frequency had to play the role of the reference frequency in our experiments. It was found later that these oscillations participated in all nonlinear processes, and the emergence of their higher harmonics was regarded as a natural criterion of the emergence of nonlinearity in resonance effects. The reflected signal after detection in an analog-digital device PC ADDA-14 with a 14-bite resolution was transformed into a computer data file. These temporal series were subsequently analyzed by using the standard and original packets of programs created for a quantitative analysis of chaotic phenomena.

DISCUSSION OF MAIN RESULTS

A typical form of resonant curves for the antiferromagnet 2C4Mn at $T = 1.8\,\mathrm{K}$ are shown in Fig. 1. For a low (less than $-15\,\mathrm{dB}$) microwave field power, a typical pattern from a linear AFMR is observed, i.e., two lines from two centers (neighboring planes). The separation between the peaks on the resonant curve can vary depending on the orientation of the static magnetic field, and the lines can coincide when the field is directed along the crystallographic axis b. For a power exceeding $-15\,\mathrm{dB}$, free relaxation oscillations are

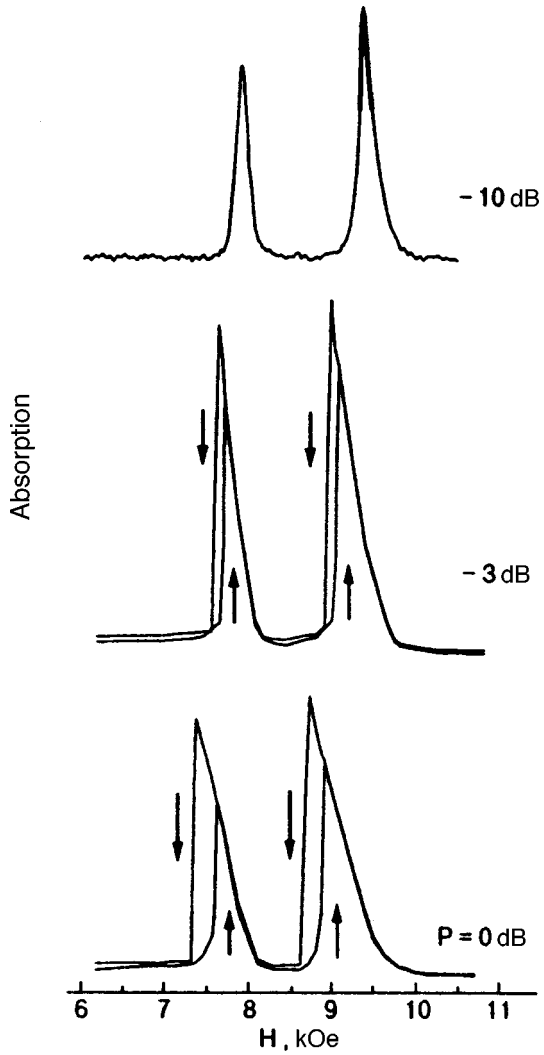

FIG. 1. Amplitude–field dependences of nonlinear antiferromagnetic resonance for a 2C4Mn crystal for different values of driving power. The bold segment on the upper curve in the vicinity of the high-field peak denotes the range of relaxation oscillations. The hysteresis loop observed for a power exceeding -5 dB increases with driving power.

generated in the range of external magnetic fields near the peak of the high-field line above as well as below the resonant field $H=9.34$ kOe (this region is shown by the bold line on the upper curve in Fig. 1). The amplitude of these oscillations increases with power until they become chaotic. We shall consider this regime in detail later, and now we pay attention to another effect associated with instability of resonance at high pumping levels. As the driving power increases above -5 dB (see two lower curves in Fig. 1), a jump and a discontinuity of both resonant lines are observed with a considerable hysteresis in the static magnetic field as we move towards higher and lower fields, respectively.

This phenomenon is well known in the theory of nonlinear resonance and is associated with the dependence of the frequency of nonlinear oscillations on their amplitude. In magnets, this effect is manifested in that the resonant curve must become asymmetric and multiple-valued for a pumping field h exceeding the critical value, i.e., the peak must be inclined towards lower or higher fields depending on the type of interaction between magnons. In actual experiments, instability is observed upon a change in the static magnetic field, and the resonant curve experiences a discontinuity or a jump. This effect was observed for the first time in disks of yttrium-iron garnet single crystals by Weiss.[35]

It follows from Fig. 1 that the jump is observed in strong fields in an increasing field, while discontinuity takes place in weaker fields in a decreasing field. With increasing power, the hysteresis loop increases, and the steepness of lines decreases (the scales of conditional units for absorbed power in Fig. 1 are different for the three resonant curves: it decreases with increasing amplitude of pumping).

It was noted above that oscillations of observed power on the segment of the resonant curve near 9.34 kOe appear even at very low driving powers of the order of -15 dB. The criterion of a transition to the nonlinear regime is the emergence of the second harmonic peak in reference oscillations with frequency 100 Hz. At the point of maximum on the resonant curve, this peak exceeds the background noise for a power $P>-15$ dB, and first spike-like peaks of absorbed power appear at the same instant.

In the case of a resonant curve with spaced peaks, an increase in the driving power induces relaxation oscillations in the vicinity of the second peak also. As the peaks converge, the mutual effect of the centers increases, which is noticeably reflected in the form of oscillations of absorbed power. In the cases of closely spaced peaks for the value of the field $H_m=8.37$ kOe corresponding to a local minimum at the center of the resonant curve, relaxation oscillations become irregular even for a low driving power. As the power increases, the oscillations become more and more chaotic. The time dependence of the signal typical of the entire series of these measurements and its spectrum for the maximum value of power are shown in Fig. 2a.

In order to find out whether such a dependence is a consequence of additive or dynamic noise, stochastic process, or is due to a determinate chaos, we varied in the experiments the orientation of magnetic field and its magnitude. The variations affected strongly the type of oscillations.

It was found that oscillations become less chaotic for the minimum deviation of the magnitude of magnetic field from the extremal value H_m. By way of an example, Fig. 2b shows the time behavior and spectrum of oscillations for $H=8.4$ kOe and the maximum driving power.

It also turned out that the degree of chaotization of a signal decreases considerably, and its shape changes qualitatively when the magnetic field is directed along the crystallographic axis b, when the resonant lines from two centers coincide. In this case, the characteristic pattern of the emergence and transformation of relaxation oscillations upon a change in the driving power is of the form shown in Fig. 3 for $H=8.4$ kOe (small deviation of the field from the resonant value) and the power P varying from -10 to 0 dB. First spikes of absorbed power appear against the background of almost linear oscillations of frequency 50 Hz. For small pumping amplitudes, the frequency corresponding to the emergence of spike-like peaks is low, and the intervals between them are quite large and vary with an obvious periodicity. For a driving power of the order of -6 dB, the signal

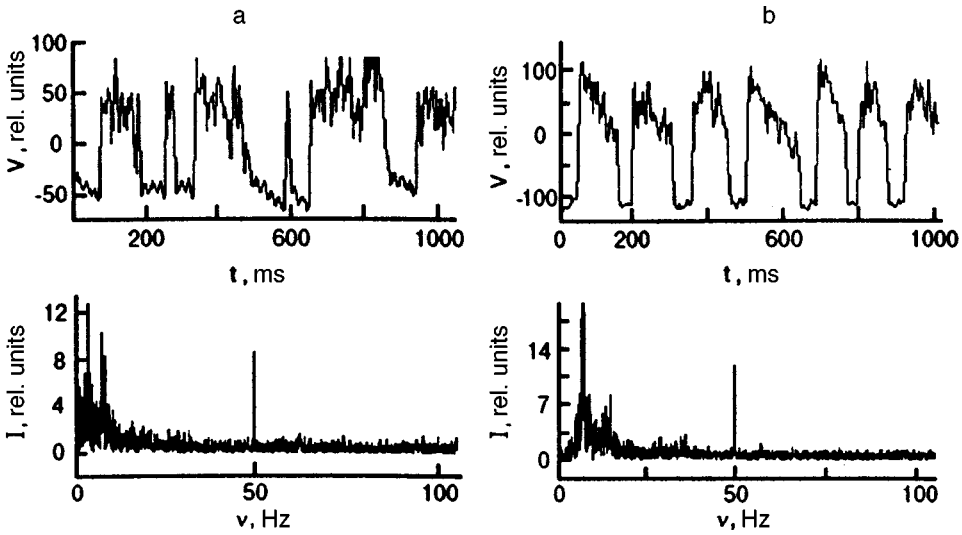

FIG. 2. Chaotic oscillations of absorbed power and their frequency spectrum for a driving power of 5 mW for a resonant curve with closely spaced peaks in fields $H_m = 8.37$ kOe (a) and 8.4 kOe (b).

has the form of a periodic structure of spike-like closely spaced peaks. As the pumping amplitude increases further to power values of the order of -3 dB, the frequency corresponding to the emergence of spike-like peaks changes insignificantly, and subsequently decreases rapidly and becomes virtually equal to half the previous value. In this region, the shape of the signal changes qualitatively from the spike- like to the saw-tooth, i.e., the change in the regime of chaotic oscillations takes place. Figure 4 shows the dependence of the fundamental frequency of these oscillations on the driving power in the range from -6 to 0 dB (dark circles). The doubling of the period of relaxation oscillations can be seen clearly in the figure. In order to plot this dependence, we analyzed the spectra of oscillations for fixed pumping levels. It should be noted that doubling of this period does not indicate the emergence of subharmonics of the fundamental frequency as is usually the case in the Feigenbaum scenario, and corresponds to a change from one oscillatory mode to another mode, their fundamental frequencies differing by a factor of two. It was proved that this effect is preserved for other values of magnetic field which naturally affects the values of frequencies themselves. It should also be noted that apart from the main peaks and multiple harmonics, all spectra contain a large contribution from noise responsible for the ''grass-like'' continuous spectrum. In the subsequent analysis, we shall analyze in detail the dynamic and spectral structure of these oscillations and the origin of their stochastic form.

When the power changes in the opposite direction, i.e., the amplitude of pumping decreases (light circles in Fig. 4), the frequency–amplitude dependence exhibits a hysteresis with a displacement of the region of period doubling towards lower powers (saw-tooth pulses exist up to -4.5 dB). The existence of essentially chaotic modes near a certain fixed values of power, in particular upon an increase in the driving power for $P=-1$, -2.25, and -2.75 dB is an interesting feature of the observed transient process.

For this reason, it was natural to analyze oscillations for these selected pumping levels, but in a wide range of applied magnetic field near the resonance point. We chose the pumping level of -1 dB and studied the variation of the shape of the absorbed power signal and its spectrum upon a change in the static magnetic field within a few ten oersteds near the resonant value $H_r = 8.37$ kOe. The direction of the field was maintained along the crystallographic axis b.

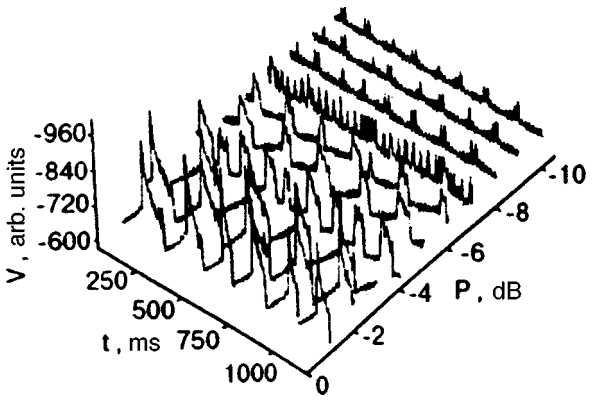

FIG. 3. Evolution of time dependences of absorbed power for a change in the microwave power level from -10 to 0 dB for a static magnetic field $H = 8.4$ kOe.

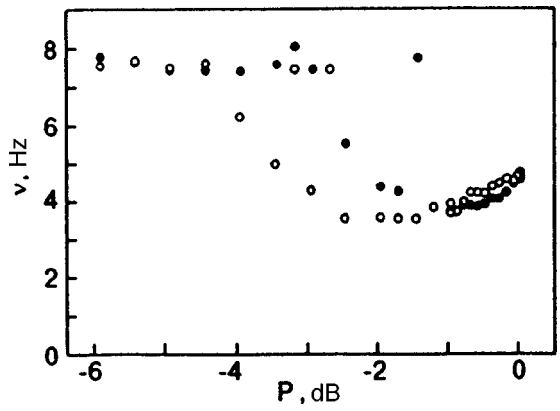

FIG. 4. Frequency of relaxation oscillations as a function of driving power. Dark and light circles correspond to an increase and decrease in the driving power, respectively. The threshold effect of oscillation period doubling is of the hysteresis type.

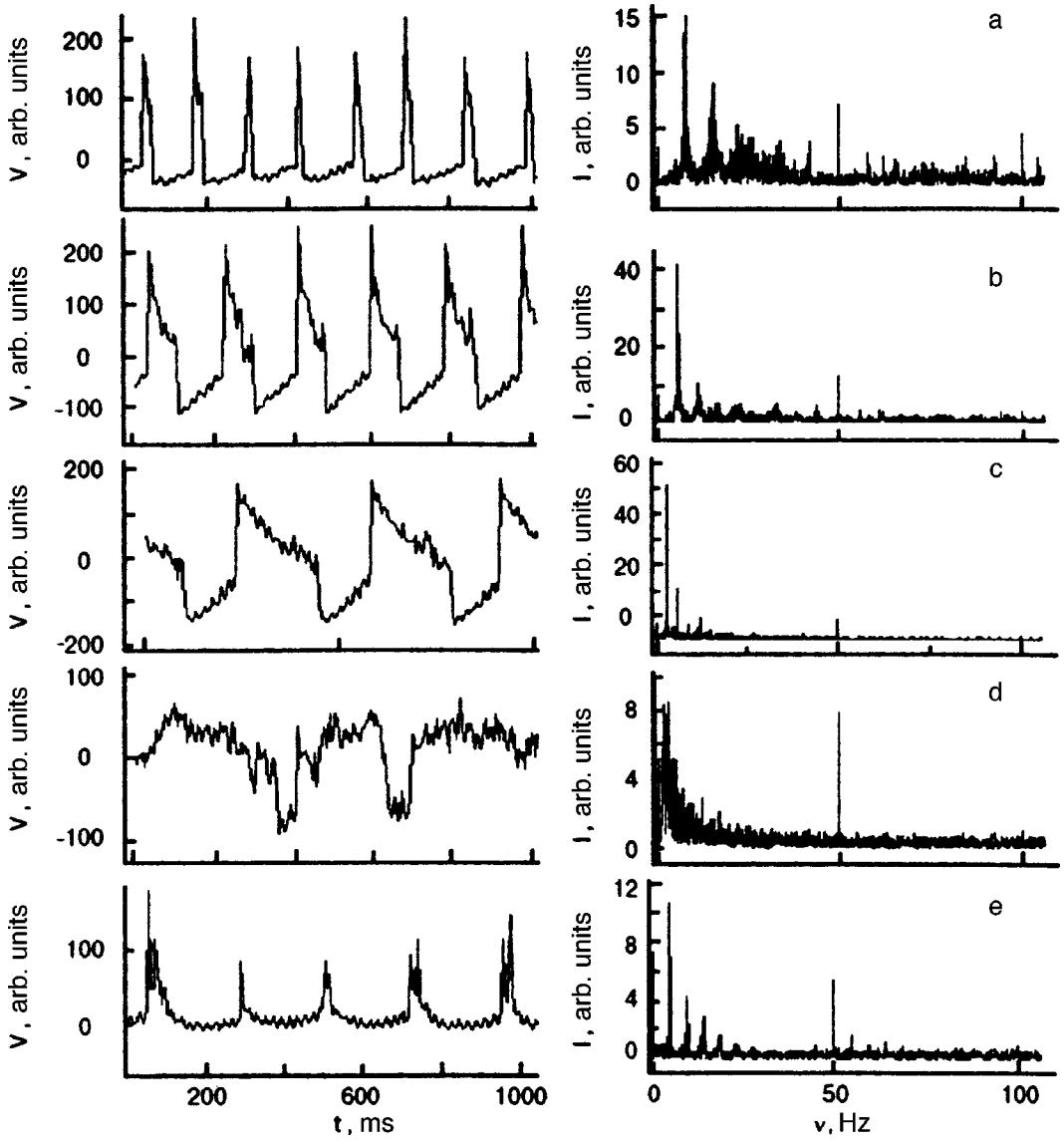

FIG. 5. Temporal series of absorbed power and their spectra for different values of static magnetic field for the driving power $P=-1$ dB; (a) $H=8.51$ kOe, relaxation oscillations with a spike-like structure and a high stochastization level; (b) $H=8.47$ kOe, the result of transformation of spike-like signals into saw-tooth signals; (c) $H=8.44$ kOe, saw-tooth relaxation oscillations with linearly increasing and decreasing segments; (d) $H=8.39$ kOe, chaotic temporal series with an intense ''grass-like'' frequency spectrum; (e) $H=8.34$ kOe, nearly regular anharmonic oscillations of absorbed power of a spike-like shape. All the spectra contain the peak of the fundamental frequency of relaxation oscillations of the order of several hertz and its higher harmonics as well as the peak of the reference frequency 50 Hz and combination frequencies.

The corresponding results are presented in Fig. 5. It should be noted that relaxation oscillations occur against a background of a considerable average absorbed power that must make a contribution to the frequency spectrum in the form of a large central peak at zero frequency. In all calculations of the spectra analyzed here, this average value was subtracted, and hence the given huge contribution to the central peak is absent, which allows us to see the detailed structure of relaxation oscillations proper. It should also be noted that frequency spectra are given in the form of frequency dependences of the amplitude of the Fourier transform of the signal and not as logarithmic spectra of power in order to improve detailization.

Another feature in common with all the spectra considered below is the presence of oscillations of frequency $\nu_0=50$ Hz. These low-frequency oscillations were present as a source of reference frequency, but they became involved in free oscillations in view of the nonlinearity of the medium. This follows from the presence of second harmonic with frequency $\nu=100$ Hz and the peaks that are algebraic sums of frequencies of fundamental harmonics of relaxation oscillations and the reference frequency.

Far away from the resonant field, the absorbed power is virtually constant if we disregard extremely low background noise in which, however, oscillations with frequency $\nu_0=50$ Hz were always manifested (in the frequency spectrum) in our measurements. As the field approaches the resonant level, these small-amplitude oscillations become weakly nonlinear (a second harmonic appears in the spectrum), and nearly periodic spike-like peaks of absorbed power corresponding to peaks of the order of a few hertz in the frequency spectrum and clearly distinguishable against the

''grass-like'' background noise appear almost simultaneously.

A typical example of such a behavior of absorbed power is shown in Fig. 5a for the field value $H=8.51$ kOe. It can be seen that periodic relaxation oscillations with a spike-like structure have been formed completely. Small anharmonic modulation of peak amplitudes is manifested in the frequency spectrum in the form of higher harmonics of the fundamental frequency. All the remaining peaks can be identified as algebraic sums of these harmonics and frequencies ν_0 and $2\nu_0$.

As we approach the resonant field further, the shape of absorbed power peaks experiences rapid qualitative changes. Figure 5b shows the result of transformation of spike-like signals into typical saw-tooth temporal series for $H=8.47$ kOe. In addition to the increase in the amplitude and relative height of frequency peaks, the emergence of linearly increasing and decreasing segments on the time dependence of absorbed power is also worth noting. It is remarkable that such oscillations are almost indistinguishable from classical relaxation oscillations that are frequently encountered in electrical engineering.

A subsequent decrease in the field leads to the tendency to the formation of periodic rectangular pulses of absorbed power. Signals of such a shape are shown in Fig. 5c for $H=8.44$ kOe. It should be noted that the amplitude of oscillations does not increase any longer, while the periodicity is enhanced, which is manifested in the frequency spectrum.

Relaxation oscillations become completely chaotic for field values close to resonance. Figure 5d shows the corresponding temporal series of absorbed power and a typical ''grass-like'' frequency spectrum for $H=8.39$ kOe. It can be seen that the amplitudes of oscillations are much smaller than those in Fig. 5c, and the frequency distribution of oscillations has become almost continuous with a sharp decrease in the maximum peak heights to the amplitude of the 50-Hz peak of the fundamental harmonic.

As the field decreases further from the resonant value, relaxation oscillations again acquire the spike-like shape, being essentially nonlinear. Figure 5e shows for $H=8.34$ kOe the temporal series for such anharmonic oscillations of absorbed power and their frequency spectrum with clearly manifested peaks of multiple harmonics. A distinguishing feature of these oscillations is that their fundamental frequency is almost half the frequency of similar spike-like oscillations presented in Fig. 5a. The frequency of relaxation oscillations in general decreases as the field decreases to the resonant value, and starts increasing after the passage of the resonance peak.

In the magnetic field scanning in the opposite direction (i.e., upon its increase), the regimes described above appear in the reverse order, but a hysteresis loop takes place in complete accord with the picture shown in Fig. 1.

It was mentioned above that the selection of other values of power (for example, the maximum power $P=0$ dB) followed by scanning in the static magnetic field results in chaotic nonlinear oscillations whose frequency structure contains higher harmonics of the fundamental frequency as well as subharmonics against the background of a high-intensity continuous noise spectrum (see Figs. 2a and b).

A comparison of temporal series also leads to the conclusion concerning clearly manifested temperature dependence of the degree of stochastization of oscillations. The higher the temperature, the higher the noise level in the oscillatory spectra and the extent of their nonregularity, and vice versa. At low temperatures, we could observe relaxation oscillations in the form of nearly rectangular pulses (such a mode was realized for $P=5$ mW, $H=8.3$ kOe, and $T=1.7$ K).

Another interesting feature is the observation of the regime of an abrupt and virtually complete disappearance of free oscillations with simultaneous doubling of the period of nonlinear reference oscillations and the emergence of their subharmonic at a frequency 25 Hz. We can try to explain the latter effect from the point of view of the theory of chaos control and the emergence of higher (multiple) resonances. However, we shall not consider this problem here and analyze the structure of chaotic attractors of relaxation oscillations.

ANALYSIS OF EXPERIMENTAL RESULTS

The method of a nonlinear analysis of experimental temporal series has been worked out intensely during the last decade and is described in detail in a number of reviews and monographs.[19,36–38] We shall use this method which involves the determination of the linear autocorrelation function for temporal series, the determination of ''time delay,'' the construction of phase portraits of attractors in the corresponding ''time delay'' coordinates, the construction of a sequence of interspike intervals, and their analysis, computation of the correlation dimension of attractors, the determination of the noise contribution to temporal series, the source of the noise and possibilities of its reduction, and the discussion of theoretical models of the observed chaotic oscillations.

The temporal series is a discrete set of values of the physical quantity (the absorbed power $V(t_n)$ in our case), measured in equal intervals of time. A traditional characteristic of temporal series of signals is the linear autocorrelation function[37]

$$C_L(\tau)=\frac{\frac{1}{N}\Sigma_{m=1}^{N}[s(m+\tau)-\overline{s}][s(m)-\overline{s}]}{\frac{1}{N}\Sigma_{m=1}^{N}[s(m)-\overline{s}]^2}, \tag{2}$$

where the average value of the signal $s(m)$ is defined in the standard manner: $\overline{s}=(1/N)\Sigma_{m=1}^{N}s(m)$.

Since we usually subtract the average value of the series from the initial series in an analysis of spectra, we calculated autocorrelation function for time dependences presented in Fig. 3 for modified series $\overline{s}=0$. As a function of τ, it exhibits qualitatively identical behavior for all values of power: this is an oscillating function with a slowly decreasing amplitude. The period of these oscillations coincides with the fundamental period of oscillations of the signal being measured. In an analysis of nonlinear signals, autocorrelation function is also useful for estimating ''time delay.'' It is chosen[19,37] equal to the value of τ for which the autocorrelation function

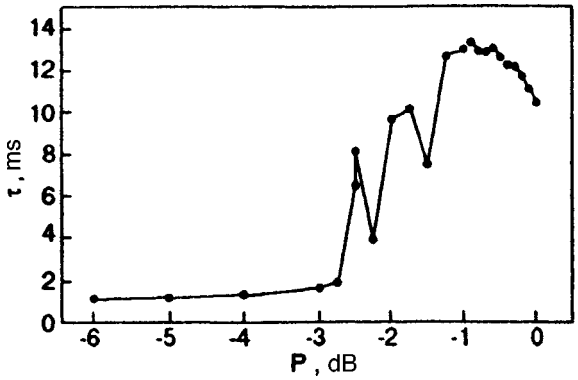

FIG. 6. Dependence of ''time delay'' τ on the pumping power P. The value of τ is measured in units of the temporal series period $\Delta t = 4.9$ ms.

vanishes for the first time. In our measurements, this time delay is approximately equal to a quarter of the fundamental period of observed oscillations.

Figure 6 shows the dependence of time τ on the driving power P. (The unit of measurements of τ is the principal interval $\Delta t = 4.9$ ms of our temporal series.) It can be seen that this dependence obviously correlates with the dependence of the frequency of oscillations on the driving power presented in Fig. 4 and confirms the existence of a threshold transition from one regime of chaotic oscillations to another. It should be noted that the period of the correlation function corresponds to oscillations of frequency 50 Hz for low powers and to the fundamental period of saw-tooth oscillations for the maximum power.

The obtained value of τ can now be used for plotting phase portraits of nonlinear oscillations. For this purpose, we shift the temporal series by τ and plot the dependence of $V(t_n+\tau)$ on $V(t_n)$. These functions are just the time delay coordinates. For the temporal series corresponding to the maximum power in Fig. 3, the phase picture is shown in Fig. 7a (the value of τ is chosen equal to 49 ms, and the average value of absorbed power is subtracted from the given series). It can be seen that the process is periodic on the whole and occurs in several stages with their own characteristic times. In order to obtain a more detailed concept of the attractor structure, we constructed a $1D$ mapping from the sequence of minimum values of the Poincaré sections of the given attractor. These values were determined as negative values of $V(t_m+\tau)$ taken at instants t_m for which $V(t_m)=0$. This dependence is shown in Fig. 7b and demonstrates the existence of the internal structure of the attractor and an obviously large contribution of noise.

A detailed analysis of the time dependence $V(t)$ indicates that the noise contribution is not additive. Indeed, irregular amplitude jumps as well as periodic oscillations of frequency 50 Hz have different values at different stages of variation of the function $V(t)$. This indicates a nonlinear enhancement of both factors and their participation in the chaotic process.

In order to describe the chaotic behavior of relaxation oscillations and the effect of noise on them quantitatively, we consider a sequence of time intervals between adjacent peaks of the signal and the sequence of maximum values of

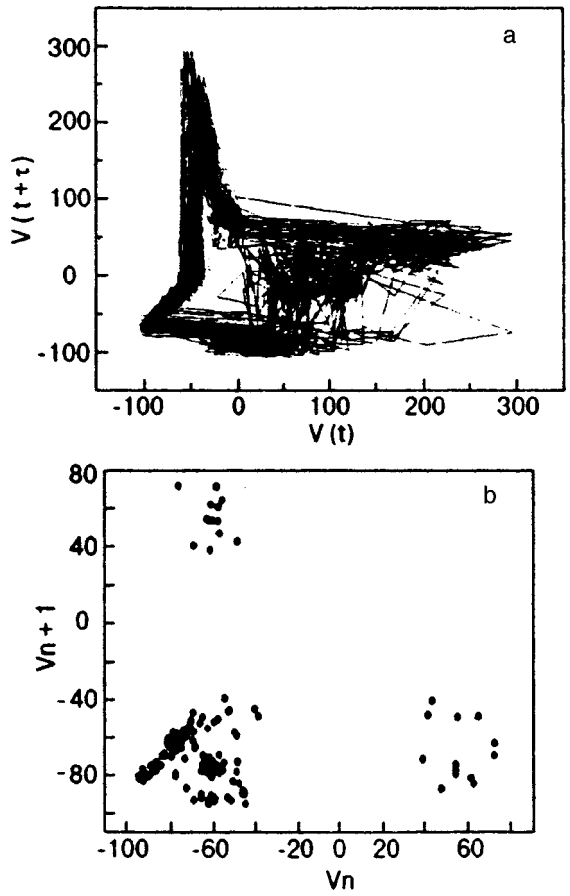

FIG. 7. Dynamic characteristics of relaxation oscillations for the driving power $P=0$ dB and $H=8.4$ kOe, whose time dependence is shown in Fig. 3: (a) phase portrait in the time delay coordinates ($\tau=49$ ms) and (b) one-dimensional mapping constructed from the sequence of minimum values of the Poincarè cross section of the phase picture taken at the instants of time t_m at which $V(t_m)=0$.

peak amplitudes as characteristics of this process.

These dependences of amplitude peaks and interspike intervals for the series under investigation are compared with the relevant sequences for the series shown in Fig. 5a. It can be seen that the amplitude peaks of oscillations of the absorbed power (Figs. 8a and b) behave quite chaotically in the vicinity of a resonance and far away from it. At the same time, the interspike intervals (Figs. 8c and d) exhibit a clearly manifested tendency to a quasiperiodic mode far away from the resonance (Fig. 8d), but random forces acting on the system result in the chaotization of oscillations, which is accompanied by chaotic jumps in the period of oscillations between its four principal values.

We can try to determine whether a noise is stochastic or dynamic by calculating the correlation dimension D of the attractor under investigation. This quantity is defined through the pair correlation integral:

$$C_m(r)=\frac{2}{N(N-1)}\sum_{i\neq j}^{N}\Theta(r-|y_m(j)-y_m(i)|), \qquad (3)$$

where N is the number of measurements, r the correlation radius, $y_m(i)$ the vector of dimensions m in the embedding space, whose coordinates are $\{V(t),V(t_i+\tau),\ldots$

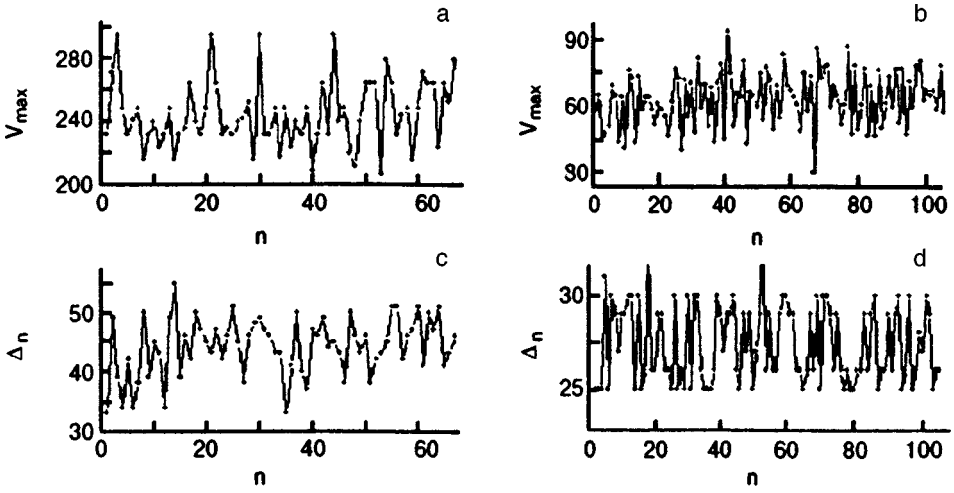

FIG. 8. Amplitude peaks and interspike intervals for relaxation oscillations for driving power $P=1$ dB and $H=8.4$ kOe (see Fig. 3) (a,c) and $P=-1$ dB, $H=8.51$ kOe (see Fig. 5a) (b,d).

$V[t_i+(m-1]\tau\}$; and $\theta(r)$ is the theta function. This function in fact determines the number of pairs of vectors in the m-dimensional space, the separation between which is smaller than the preset distance r. While determining the distance, we presume that the cells into which the phase space is divided have the cubic shape.[39] The dimension D is the limit of the expression

$$D=\lim_{m\to\infty}\frac{d\ln C_m(r)}{d\ln r} \tag{4}$$

and is usually calculated on the interval r in which the values of the correlation function are not very small.

The sequence of calculated correlation functions for the initial temporal series corresponding to the maximum power in Fig. 3 is presented in Fig. 9 on logarithmic scale (the curves correspond to the variation of m from 1 to 9 from top to bottom). Numerical differentiation reveals a flat segment according to which the dimension of a strange attractor can be estimated. It was found that it is slightly larger than two (2.25 ± 0.1), but the strong effect of dynamic noise following from the characteristic increase in the steepness of the curves for $\ln(r)<2.5$ does not allow us to establish the existence of the exact limit. We are inclined to interpret the latter quantity as the dimension of a regular attractor. On the other hand, the slope of the curves in the region $1<\ln(r)<2.5$ also demonstrates the tendency to a limit that can be estimated as 4.9 ± 0.1. Such a limiting value can be regarded as the total dimension of the attractor, containing the contribution from a regular attractor and a deterministic noise. A slight increase in the dimension for large values of m for small r is associated with the contribution of ''white'' instrumental noise. The above comparative analysis of functional dependences of temporal series and their spectra also confirms this conclusion. Thus, the analysis of the correlation dimension leads to the conclusion concerning the dynamic nature of noise in the relaxation oscillations under investigation and indicates a multidimensional chaotic dynamics and, generally speaking, multimode excitations in the resonance system in question. The extent of its stochastization is quite high, which follows from the estimate of correlation dimension in the range of small r. It should be noted that recent investigations of parametric resonance in a related metallorganic antiferromagnet[31] also confirms the deterministic origin of noise in these compounds.

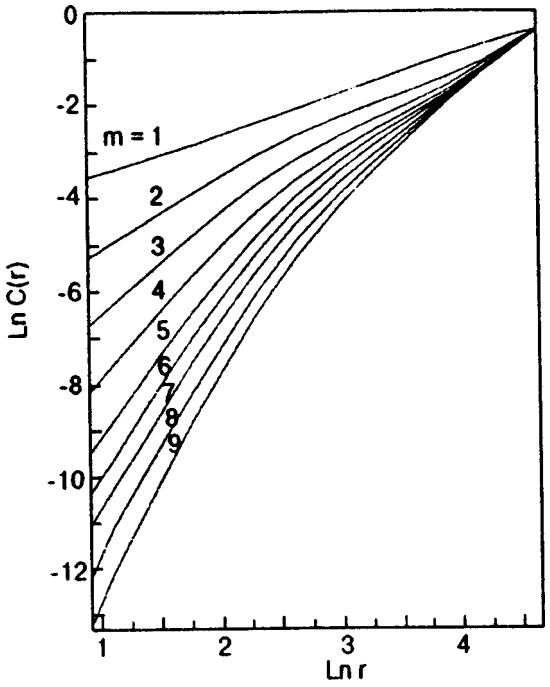

FIG. 9. Dependences of logarithms of correlation integrals on the logarithm of the distance between vectors in the m-dimensional embedding space calculated from the initial integral data for the attractor presented in Fig. 7.

The existing theories of relaxation oscillations[3,8,9,29,32] make it possible to describe the emergence of a high-dimensional chaos on the basis of multimode models. The main idea behind the mechanism of emergence of relaxation oscillations can be demonstrated even by using a two-mode model in which it is assumed that the resonance excitation conditions are satisfied for one mode and are not observed for the other mode. Under the action of pumping, such a pair of coupled nonlinear oscillators reproduces quantitatively the behavior of relaxation oscillations. A quantitative theory of this effect for antiferromagnets has not been developed as yet. However, a theoretical description of this phenomenon

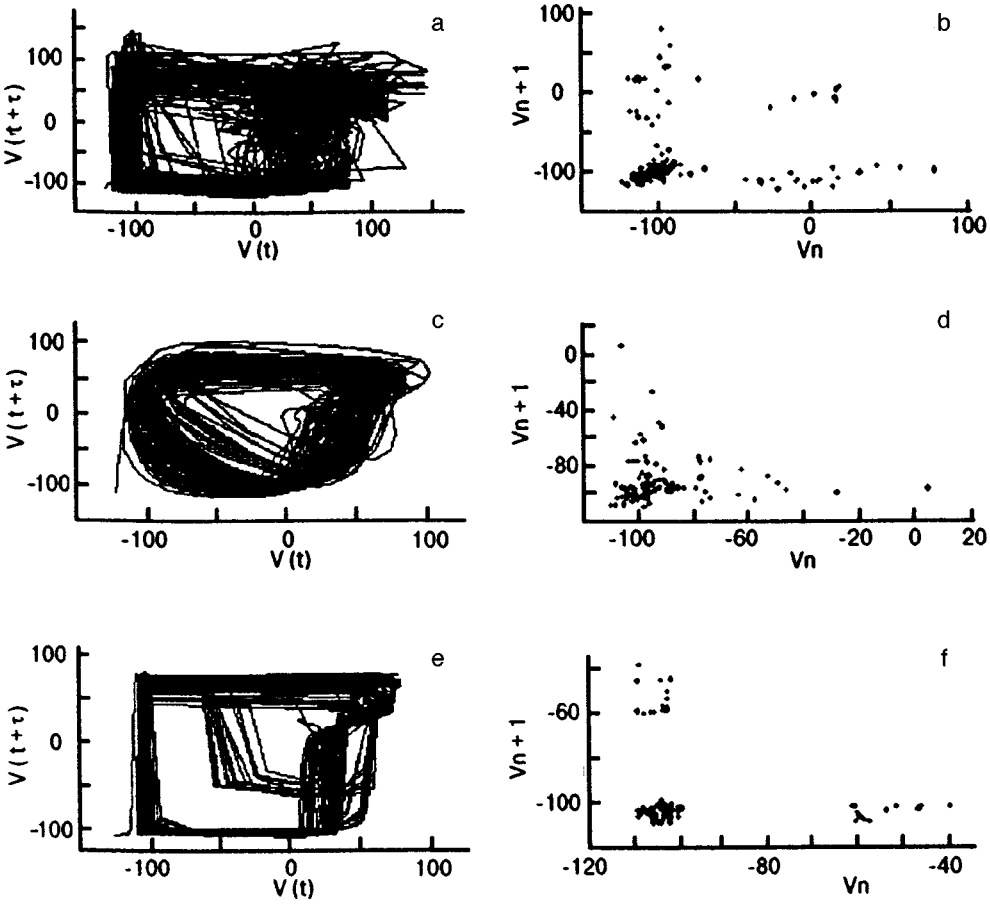

FIG. 10. Phase portraits and one-dimensional mapping for relaxation oscillations for the driving power 5 mW in the field $H=8.4$ kOe in the case of closely spaced peaks on the resonant curves (see Fig. 2b) for original data on temporal series (after the subtraction of the average value) (a,b), for doubly averaged data for five nearest neighbors (c,d), and for data ''improved'' by the optimized method of noise suppression as a result of ten iterations (e,f).

in the approximation of two spins simulating the sublattices subjected to resonant transverse and longitudinal pumping appears as promising. Consequently, chaotic relaxation oscillations can be described qualitatively as the dynamics of a nonlinear oscillator under resonance conditions, but under the action of certain random forces (the inclusion of the effect of the second oscillator). Such a system may have at least two stable states the transition between which can lead to the emergence of spike-like and saw-tooth time dependences of absorbed power. The features and diversity of existing chaotic modes are obviously determined by the time of residence of the system in the equilibrium states and the rate of transient processes. Such a system can obviously have a high degree of stochastization, an attempt to create regular attractors in it will lead to regimes in which such attractors coexist with a well-developed dynamic noise. However, a quantitative theory of such chaotic oscillations should apparently be constructed on the basis of a multimode model according to the numerical analysis carried out by Moser *et al.*[32]

The theorem on dimensionality that has been formulated recently for systems with a dynamic noise indicates in its simplified formulation the additivity of the dimension of a regular attractor and a noise.[40] In this sense, these can be separated, and the question of elimination of noise from a signal, noise reduction, and isolation of a regular signal from the data on temporal series appears as justified.

There are effective methods of noise reduction in the useful signal.[38] These methods are extremely effective for suppressing external additive noise, but their application in the case of a dynamic noise should be verified in each specific case. The algorithm of purification of a signal in the simplest form can be described as follows. In the chosen embedding space whose dimension is larger than the sum of the predicted dimension of the regular attractor and dynamic noise, the nearest neighbors of the preferred vector of state are selected, and its central coordinate is averaged over the values of relevant coordinates of the found neighbors. The obtained sequence of new data is the result of one iteration that can be repeated. Such an algorithm can be optimized as well as the choice of required parameters (correlation radius, dimension, etc.; see Ref. 38). Such an algorithm will be used below for analyzing the chaotic temporal series measured by us.

On the other hand, the above algorithm in the simplest form includes the conventional method of data averaging over nearest and next to nearest neighbors in the series. In this case, the dimension of the embedding space is equal to unity, and the number of neighbors is fixed. It can easily be verified that, in spite of its very simple form, the procedure operates as a high-frequency filter and does not change the complex low-frequency spectrum of chaotic oscillations. We shall apply this procedure also to analyze the results.

We chose the object of investigation in the form of a chaotic attractor obtained from the temporal series presented in Fig. 2b. The results of analysis are shown in Fig. 10 (it should be noted that the average value is subtracted from the terms of the series). Figures 10a and b show the phase por-

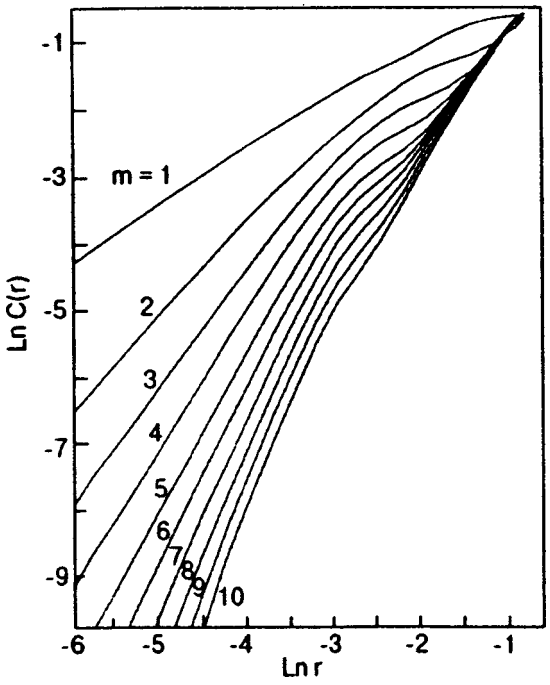

FIG. 11. Dependences of logarithms of correlation functions on the logarithm of the distance between vectors in the m-dimensional embedding space calculated for data ''improved'' by the optimized method (see Figs. 10e and f).

trait on the plane $\{V(t), V(t+\tau)\}$, where $\tau = 29.5$ ms, and simultaneously the mapping for the data on the Poincaré cross section (see above), while Figs. 10c, d, e, and f contain the dependences for the data ''corrected'' by the method of averaging and the optimized method of noise reduction described above respectively (averaging was carried out twice over five points, and tenfold iterations were used in the optimized method).

Figures 10e and f clarify the internal structure of a regular attractor. After the effect of noise becomes weaker, its phase portrait resembles a strange multiband attractor. The analysis of correlation dimension makes it possible to characterize quantitatively both the regular attractor as well as the residual contribution of deterministic noise. The results of analysis are presented in Fig. 11. It should be noted that, prior to calculation of correlation functions for the temporal series under consideration, we initially normalized all values to a unit interval by the formula $V(t_n) = [V(t_n) - V_{\min}]/(V_{\max} - V_{\min})$, where $V_{\min}$ and $V_{\max}$ are the minimum and maximum values of the signal in the series. It was found that the dimensionality of a regular attractor can be estimated as 2.15 ± 0.05, and the total dimensionality with the contribution of deterministic noise as 3.25 ± 0.05. Spectral analysis of these ''improved'' results also indicate that the quantitative contribution of noise remained quite large, and the resultant attractor possesses a high dimensionality as before.

Thus, chaotic dynamics in the nonlinear antiferromagnetic resonance in low-dimensional antiferromagnets is high-dimensional, the extent of stochastization of oscillations is high, and noise has a deterministic origin and serves as a decisive factor in nonlinear dynamics of these magnets.

Finally, we formulate the following conclusions following from our analysis.

(1) Peculiarities of a transition to chaos by ''irregular periods'' in a $2D$ metallorganic antiferromagnet with an ''easy axis'' type anisotropy are experimentally observed and studied in detail under conditions of nonlinear antiferromagnetic resonance.
(2) It is shown that relaxation oscillations of absorbed power are generated for very low energy levels of microwave field and have a low frequency of fundamental harmonic (of the order of a few hertz). No multiple harmonics are observed experimentally at kilohertz and higher frequencies.
(3) Relaxation oscillations at low values of driving power exist in the form of generally periodic sequence of spike-like peaks of absorbed power. The frequency spectrum contains components of fundamental frequency corresponding to the emergence of spikes as well as multiple harmonics, which demonstrates the nonlinear nature of the process.
(4) As the pumping amplitude increases, the phenomenon of period doubling is observed in the time dependence of absorbed energy of microwave field. The shape of the signal is simultaneously transformed from the spike-like to the saw-tooth type having segments with linearly increasing and linearly decreasing absorption. An analysis of the frequency-amplitude dependence of oscillations and their linear autocorrelation function gives quantitative characteristics of this transition.
(5) A similar effect is observed at a fixed level of pumping, but upon a change in the value of static magnetic field near its resonant value.
(6) With increasing power, relaxation oscillations become chaotic. The spectrum of such oscillations is continuous and has a ''grass-like'' form, but the peaks of fundamental harmonics are still distinguishable. The phase portrait of these oscillations has the form of a strange attractor experiencing a strong influence of noise. Stochastization of oscillations, however, is not a result of influence of an additive instrumental noise.
(7) The quantitative characteristics of such a strange attractor are calculated. The one-dimensional mapping corresponding to the given attractor demonstrates a tendency to regular movement in spite of chaotic time dependence of relaxation oscillations. An analysis of correlation dimension indicates the high-dimensional chaos dynamics and the deterministic nature of noise in the magnetic system under investigation. The possibility of formal separation of the regular movement and the noise contribution with the help of nonlinear methods of noise reduction being developed is considered.
(8) The applicability of the theoretical model of finite number of coupled spins under the action of the parametric and transverse pumping to the construction of a quantitative theory of the scenario of transition to chaos by ''irregular periods'' is discussed briefly. The transition can be regarded as a universal phenomenon in low-

dimensional ferro- and antiferromagnets under nonlinear resonance conditions.

The authors are grateful to S. V. Volotskiĭ for fruitful discussions and to H. Kantz, R. Hegger, and Th. Schreiber for valuable advice and help in carrying out a number of calculations.

*)E-mail: bogdan@ilt.kharkov.ua

[1] G. Gibson and C. Jeffries, Phys. Rev. A **29**, 811 (1984).
[2] H. Yamazaki, J. Phys. Soc. Jpn. **53**, 1155 (1984).
[3] F. Waldner, R. Badii, D. R. Barberis *et al.*, J. Magn. Magn. Mater. **54-57**, 1135 (1986).
[4] H. Yamazaki and M. Warden, J. Phys. Soc. Jpn. **55**, 4477 (1986).
[5] F. M. de Aguiar and S. M. Rezende, Phys. Rev. Lett. **56**, 1070 (1986).
[6] A. I. Smirnov, Zh. Éksp. Teor. Fiz. **90**, 385 (1986) [Sov. Phys. JETP **63**, 222 (1986)].
[7] H. Yamazaki, M. Mino, H. Nagashima, and M. Warden, J. Phys. Soc. Jpn. **56**, 742 (1987).
[8] P. Bryant, C. Jeffries, and K. Nakamura, Phys. Rev. A **38**, 4223 (1988).
[9] M. Warden and F. Waldner, J. Appl. Phys. **64**, 5386 (1988).
[10] A. I. Smirnov, Zh. Éksp. Teor. Fiz. **94**, 185 (1988) [Sov. Phys. JETP **67**, 969 (1988)].
[11] T. L. Carrol, L. M. Pecora, and F. J. Rachford, J. Appl. Phys. **64**, 5396 (1988).
[12] H. Benner, F. Rodelsperger, H. Seitz, and G. Wiese, J. Phys. C **8**, 1603 (1988).
[13] P. E. Wigen, H. Doetsch, Y. Ming *et al.*, J. Appl. Phys. **63**, 4157 (1988).
[14] A. A. Stepanov, M. I. Kobets, and A. I. Zvyagin, Fiz. Nizk. Temp. **9**, 764 (1983) [Sov. J. Low Temp. Phys. **9**, 391 (1983)].
[15] A. I. Zvyagin, M. I. Kobets, V. N. Krivoruchko *et al.*, Zh. Éksp. Teor. Fiz. **89**, 2298 (1985) [Sov. Phys. JETP **62**, 1328 (1985)].
[16] A. A. Stepanov, V. A. Pashchenko, and M. I. Kobets, Fiz. Nizk. Temp. **14**, 550 (1988) [Sov. J. Low Temp. Phys. **14**, 304 (1988)].
[17] A. A. Stepanov, V. A. Pashchenko, and M. I. Kobets, Fiz. Nizk. Temp. **14**, 1212 (1988) [Sov. J. Low Temp. Phys. **14**, 669 (1988)].
[18] A. A. Stepanov, A. I. Zvyagin, S. V. Volotskii *et al.*, Fiz. Nizk. Temp. **15**, 100 (1989) [Sov. J. Low Temp. Phys. **15**, 57 (1989)].
[19] H. Yamazaki and M. Mino, Prog. Theor. Phys. Suppl. **No. 98**, 400 (1989).
[20] J.-P. Eckmann, Rev. Mod. Phys. **53**, 643 (1981).
[21] M. Feigenbaum, Usp. Fiz. Nauk **141**, 343 (1983) [*sic*].
[22] J.-P. Eckmann and D. Ruelle, Rev. Mod. Phys. **57**, 617 (1985).
[23] V. E. Zakharov, V. S. L'vov, and S. S. Starobinets, Usp. Fiz. Nauk **114**, 609 (1974) [Sov. Phys. Usp. **17**, 896 (1974)].
[24] V. V. Zautkin, V. S. L'vov, and S. S. Starobinets, Zh. Éksp. Teor. Fiz. **63**, 182 (1973) [Sov. Phys. JETP **36**, 96 (1974)].
[25] V. V. Zautkin, V. S. L'vov, and S. S. Starobintes, Fiz. Tverd. Tela (Leningrad) **16**, 446 (1974) [Sov. Phys. Solid State **16**, 286 (1974)].
[26] H. Benner, F. Roedelsperger, and G. Wiese, in *Nonlinear Dynamics in Solids* (ed. by H. Thomas), Springer, Berlin, Heidelberg (1992) p. 129.
[27] F. M. de Aguiar, A. Azevedo, and S. M. Rezende, Phys. Rev. B **39**, 9448 (1989).
[28] T. S. Hartwick, E. R. Peressini, and M. T. Weiss, J. Appl. Phys. **32**, 223S (1961).
[29] F. Waldner, D. R. Barberis, and H. Yamazaki, Phys. Rev. A **31**, 420 (1985).
[30] F. Waldner, J. Phys. C **21**, 1243 (1988).
[31] M. Warden, Phys. Rev. E **48**, R639 (1993).
[32] H. R. Moser, P. F. Meier, and F. Waldner, Phys. Rev. B **47**, 217 (1993).
[33] H. Arend, K. Tichy, K. Baberschke, and F. Rys, Solid State Commun. **18**, 999 (1976).
[34] K. Tichy, J. Benes, R. Kind, and H. Arend, Acta Crystallogr., Sect. B: Struct. Crystallogr. Cryst. Chem. **36**, 1355 (1980).
[35] M. T. Weiss, Phys. Rev. Lett. **1**, 239 (1958).
[36] N. Gershenfeld, in *Directions in Chaos*, vol. 2 (ed. by Hao Bai-lin), World Scientific, Singapore (1988) p. 310.
[37] H. D. I. Abarbanel, R. Brown, J. J. Sidorowich, and L. Sh. Tsimring, Rev. Mod. Phys. **65**, 1331 (1993).
[38] H. Kantz and Th. Schreiber, *Nonlinear Time Series Analysis*, Cambridge Univ. Press, Cambridge (UK) (1997).
[39] I. S. Aranson, A. M. Reiman, and V. G. Shekhov, in *Nonlinear Waves. Dynamics and Evolution* (ed. by A. V. Gaponov-Grekhov and M. I. Rabinovich), [in Russian], Nauka, Moscow (1989).
[40] M. R. Muldoon, D. S. Broomhead, J. P. Huke, and R. Hegger, *Dynamics and Stability of Systems* **13**, 175 (1998).

Translated by R. S. Wadhwa

ELECTRONIC PROPERTIES OF METALS AND ALLOYS

Nonlinear electromagnetic waves in metals under strong magnetism of conduction electrons

V. G. Peschanskiĭ[1,2]

[1]*B. Verkin Institute for Low Temperature Physics and Engineering, National Academy of Sciences of the Ukraine, 310164 Kharkov, Ukraine* and Kharkov State University, 310077 Kharkov, Ukraine*[2]

D. I. Stepanenko[2]

[2]*Kharkov State University, 310077 Kharkov, Ukraine*

(Submitted September 28, 1998)
Fiz. Nizk. Temp. **25**, 277–281 (March 1999)

Wave processes in noncompensated metals in a quantizing magnetic fields are investigated theoretically. It is shown that small-amplitude nonlinear electromagnetic waves can propagate when the magnetic susceptibility is close to $1/4\pi$. Nonlinear solutions of the system of Maxwell equations are obtained under the conditions of strong magnetism of conduction electrons.
 [S1063-777X(99)00803-8]

Weakly attenuating electromagnetic waves of frequency ω much lower than the cyclotron frequency Ω of conduction electrons can propagate in pure metals at liquid helium temperatures in a strong magnetic field $\mathbf{H}_0$.[1,2] In classically strong magnetic fields $\Omega\tau \gg 1$, where τ is the electron mean free time, the nonlinearity region in metals is difficult to create in actual practice. High electrical conductivity hampers the creation of a strong electric field, while nonlinear effects caused by the influence of the magnetic field $\tilde{\mathbf{H}}$ of the wave are suppressed by the external field $\mathbf{H}_0$ and are significant only when $\tilde{\mathbf{H}}$ is comparable with $\mathbf{H}_0$. However, nonlinearity can be significant even for small-amplitude waves at low temperatures at which charge carrier quantization levels in a magnetic field must be taken into account. If the separation $\Delta\varepsilon \approx \hbar\Omega$ between the Landau levels is much larger than their width $\hbar/\tau$ and than the temperature of charge carriers, the quantum oscillating component of magnetic susceptibility χ can attain values of the order of unity ($\hbar$ is Planck's constant). In this case, the difference between the magnetic field **H** and magnetic induction **B** is significant even in conductors without any magnetic ordering, and the inclusion of magnetism is a self-consistent problem. Quantum energy levels of charge carriers in a metal are determined by the value of the microscopic field **H** averaged over regions of the order of the Larmor radius for electron, and hence the magnetization **M** is a function of the magnetic induction $\mathbf{B}=\mathbf{B}_0+\tilde{\mathbf{B}}(\mathbf{r},t)$, where $\mathbf{B}_0$ is its uniform component and $\tilde{\mathbf{B}}(\mathbf{r},t)$ is the field of the wave. For $\kappa^2 \equiv |1-4\pi\chi(\mathbf{B}_0)| \ll 1$, the linear term of the expansion of the magnetic field $\mathbf{H}=\mathbf{B}-4\pi\mathbf{M}$ into a power series in $\tilde{\mathbf{B}}(\mathbf{r},t)$ may be of the same order of magnitude as nonlinear terms, and Maxwell's equations will be essentially nonlinear.

The influence of strong magnetism of conduction electrons on wave processes in compensated metals was studied in Ref. 3. In this communication, we consider the propagation of nonlinear waves in noncompensated metals with different numbers of electrons (n_e) and holes (n_h) under the following conditions

$$\omega\tau \ll 1, \quad kr_0 \ll 1,$$

$$k_z l \ll 1, \quad 0 < 1-4\pi\chi \ll 1,$$

where $\mathbf{k}=(0,\ k\sin\theta,\ k\cos\theta)$ is the wave vector, r_0 the radius of curvature of the electron trajectory in the uniform field $\mathbf{B}_0=(0,0,\mathbf{B}_0)$, $l=v_F\tau$, v_F being the Fermi velocity.

A varying electromagnetic field in an infinite metal is defined by the system of Maxwell's equations

$$\operatorname{curl}\mathbf{B}=\frac{4\pi}{c}\mathbf{J}, \quad \operatorname{curl}\mathbf{E}=-\frac{1}{c}\frac{\partial\mathbf{B}}{\partial t}, \quad \operatorname{div}\mathbf{B}=0, \tag{1}$$

supplemented with constitutive relations for the current density and magnetization. Here $\mathbf{J}=\mathbf{j}+c\operatorname{curl}\mathbf{M}$ is the density of total current including the conduction current **j** and the current $\mathbf{j}'=c\operatorname{curl}\mathbf{M}$ induced by the magnetic field, c being the velocity of light.

In the quasi-stationary case $\omega\tau \ll 1$, the system of conduction electrons has time to tune itself to the instantaneous values of varying fields, and we can use static expressions for **j** and **M** substituting into them the values of the fields **E** and $\tilde{\mathbf{B}}$ at the given instant of time. For $k_z l \ll 1$, we can neglect spatial dispersion in the expression for **j** and write the conduction current density in the form

$$j_i=\sigma_{ik}(B_0)E_k, \tag{2}$$

where $\sigma_{ik}(B_0)$ is the static conductivity tensor in uniform fields. In the semiclassical approximation in which the separation between Landau levels is much smaller than the Fermi energy ε_F, quantum corrections to the electrical conductivity of a metal proportional to $(\hbar\Omega/\varepsilon_F)^{1/2}$ are usually small.[4] Their inclusion does not affect the existence of natural oscil-

lations of electromagnetic field and is reduced to a change in the damping decrement of the wave. Since the ultraquantum limit $\hbar\Omega \gtrsim \varepsilon_F$ is attainable only in semimetals of the bismuth type, the semiclassical description of electron phenomena in metals with the number of charge carriers of the order of one carrier per atom is valid in a wide range of actually attainable magnetic fields. In the further analysis, we shall use the expression for the conductivity tensor in classically strong magnetic fields.

Using the local form of current density (2), we can easily obtain from the system of equations (1) the vector equation for the components of the transient field $\tilde{\mathbf{B}}(\mathbf{r},t)$:

$$\frac{\partial \tilde{\mathbf{B}}}{\partial t} = -\frac{c^2}{4\pi}\operatorname{curl}(\hat{\rho}\operatorname{curl}\mathbf{H}), \tag{3}$$

where $(\rho \operatorname{curl}\mathbf{H})_k = \rho_{ki}(\operatorname{curl}\mathbf{H})_i$, $\mathbf{H} = \mathbf{B} - 4\pi\mathbf{M}(\mathbf{B})$.

In noncompensated metals, the diagonal components of the resistivity tensor $\rho_{ki}(\sigma^{-1})_{ki}$ have the same order of magnitude. Without any loss of generality in the analysis of wave processes, we assume that all of them are the same, equal to $\rho_0 = 1/\sigma_0$, where $\sigma_0 \approx \omega_p^2\tau/4\pi$ is the static electrical conductivity of the metal in zero magnetic field and ω_p is the frequency of plasma oscillations of charge carriers. This allows us to reduce Eq. (3) to the form

$$\frac{\partial \tilde{\mathbf{B}}}{\partial t} = -\frac{c^2}{4\pi}(\mathbf{b}\cdot\nabla)\operatorname{curl}\mathbf{H} - \frac{c^2}{4\pi}\rho_0(\operatorname{grad}\operatorname{div}\mathbf{H} - \Delta\mathbf{H}), \tag{4}$$

where $b_j = (1/2)\varepsilon_{jki}\rho_{ki}$ is the vector dual to the tensor ρ_{ki}. If we take into account the difference between ρ_{ii}, Maxwell's equation retains the form (4) under appropriate transformation of coordinate axes. The largest component of the vector $\mathbf{b}$ is b_z determined by the Hall component of the resistivity tensor $\rho_{xy} = B_0/ce(n_e - n_h)$. If $\Omega\tau\cos\theta \gg 1$, the remaining components of vector $\mathbf{b}$ in the first term on the right-hand side of (4) can be neglected for any type of the electron energy spectrum, and the asymptotic expression for the vector $\mathbf{b}$ have the following form accurate to an insignificant dimensionless factor of the order of unity: $\mathbf{b} = (0,0,\Omega\tau\rho_0)$.

The density $\mathbf{j}'$ of the current induced by the magnetic field is mainly determined by the magnetization component M_z since the vector $\mathbf{M}$ is directed predominantly along $\mathbf{B}_0$, and $M_x, M_y \ll M_z$. We write the expansion of the induced current density into a power series in $\tilde{\mathbf{B}}(\mathbf{r},t)$ and its derivatives in the form[3,5]

$$j_x' = c(\operatorname{curl}\mathbf{M})_x = c\chi(B_0)\frac{\partial \tilde{B}_z}{\partial y} - c\xi\frac{\partial \tilde{B}_z^3}{\partial y} + c\alpha r_0^2\frac{\partial^3 \tilde{B}_z}{\partial y^3}, \tag{5}$$

where $\xi = (\beta/B_0^2)(\varepsilon_E/\hbar\Omega)^2$, and α and β are dimensionless coefficients of the order of unity. The second and third terms in formula (5) are determined by the nonlinear and nonuniform correction to magnetization.

After simple transformations, we obtain the following equation for $\tilde{B}_z(y,z,t)$:

$$\left(\frac{\omega_p^2}{c^2\Omega}\right)^2\frac{\partial^2 \tilde{B}_z}{\partial t^2} + \frac{\partial^2}{\partial z^2}\left(\frac{\partial^2 \tilde{H}_z}{\partial y^2} + \frac{\partial^2 \tilde{B}_z}{\partial z^2}\right) = \frac{1}{\Omega\tau}\frac{\omega_p^2}{c^2\Omega}\Delta\frac{\partial \tilde{B}_z}{\partial t} + \frac{1}{\Omega\tau}\left(\frac{\omega_p^2}{c^2\Omega}\frac{\partial}{\partial t} - \frac{1}{\Omega\tau}\Delta\right) \times\left(\frac{\partial^2 \tilde{H}_z}{\partial y^2} + \frac{\partial^2 \tilde{B}_z}{\partial z^2}\right). \tag{6}$$

In the linear approximation, this equation describes waves of the helicoid type with frequency

$$\omega_l = \frac{k^2c^2\Omega}{\omega_p^2}\cos\theta\sqrt{\kappa^2\sin^2\theta + \cos^2\theta}, \tag{7}$$

differing from the frequency of a helicon in a classically strong magnetic field by the factor $\sqrt{\kappa^2\sin^2\theta + \cos\theta}$. It can easily be seen that, for $\kappa^2 \ll 1$ and $\cos\theta \sim \kappa$, linear and nonlinear terms in $\tilde{B}_z$ are quantities of the same order of magnitude, and the wave process is essentially nonlinear. The attenuation length

$$l_d \simeq \kappa(\omega\tau)^{-1/2}(\Omega\tau\cos\theta)^{3/2}\frac{c}{\omega_p} \simeq \kappa k^{-1}\Omega\tau\cos\theta \tag{8}$$

in this case must be considerably larger than the wavelength, which is observed under the condition

$$\kappa\Omega\tau\cos\theta \gg 1.$$

Inclusion of the term proportional to $\tilde{B}_z^3$ in the expression for

$$\tilde{H}_z = \kappa^2\tilde{B}_z + 4\pi\xi\tilde{B}_z^3 - 4\pi\alpha r_0^2\frac{\partial^2 \tilde{B}_z}{\partial y^2} \tag{9}$$

leads to the emergence of elliptic functions in the solution of Eq. (6) which has the following form in the dimensionless variables $u = \tilde{B}_z/b_0$, $y_1 = y/L$, $z_1 = \kappa z/L$, $t_1 = (\kappa^2/L^2)\times(c^2\Omega/\omega_p^2)t$:

$$\frac{\partial^2 u}{\partial t_1^2} + \frac{\partial^2}{\partial z_1^2}\left(\frac{\partial^2 W(u)}{\partial y_1^2} + \frac{\partial^2 u}{\partial z_1^2}\right) = \frac{\gamma}{\kappa^2}\Delta_1\frac{\partial u}{\partial t_1} + \gamma\left(\frac{\partial}{\partial t_1} - \frac{\gamma}{\kappa^2}\Delta_1\right) \times\left(\frac{\partial^2 W(u)}{\partial y_1^2} + \frac{\partial^2 u}{\partial z_1^2}\right). \tag{10}$$

Here

$$W(u) = \left(u + u^3 - \delta\frac{\partial^2 u}{\partial y_1^2}\right);$$

$$\gamma = \frac{1}{\Omega\tau}; \quad \delta = \frac{4\pi\alpha r_0^2}{L^2\kappa^2};$$

$$b_0 = B_0\sqrt{\kappa^2/4\pi\xi} \simeq \kappa B_0(\hbar\Omega/\varepsilon_F);$$

$$\Delta_1 = \frac{\partial^2}{\partial y_1^2} + \kappa^2\frac{\partial^2}{\partial z_1^2},$$

where L and $\kappa^{-1}L$ are the characteristic scales of nonuniformity of the nonstationary field in the y- and z-directions. Dissipative terms on the right-hand side of Eq. (10) are small when the inequality $\Omega\tau\kappa^2 \gg 1$ is satisfied. In this case, Eq. (10) in the zeroth approximation in the small parameter

$\eta=\gamma/\kappa^2$ has a wave solution, and the function $u(\mathbf{r}_1,t)$ can be sought in the form $u=u(\psi)$, where $\psi=n_1y_1+n_2z_1-Vt_1$.

Substituting this expression into Eq. (10) and neglecting terms of the order of η, we obtain

$$\frac{V^2}{n_2^2}\frac{d^2u}{d\psi^2}+\frac{d^2}{d\psi^2}\left(s^2u+n_1^2u^3-n_1^4\delta\frac{d^2u}{d\psi^2}\right)=0, \tag{11}$$

where $s^2=n_1^2+n_2^2$.

In the case of large wavelengths, the solution of this equation can be written in a simple parametric form. If $L\propto k^{-1}$ is quite large and $\delta\sim(kr_0/\kappa)^2\ll 1$, the last term in the parentheses can be neglected. Integrating thrice the obtained equation with respect to ψ and putting $u=u(w)$, where $w=\int u\,d\psi$, we obtain after transformations the following equation connecting u and w:

$$\frac{V^2}{n_2^2}w^2=C^2-s^2u^2-\frac{3}{2}n_1^2u^4, \tag{12}$$

where C^2 is the integration constant. This leads to the implicit dependence $u(\psi)$:

$$d\psi=\frac{dw}{u}=-\frac{n^2}{V}\frac{(s^2+3n_1^2u^2)du}{(C^2-s^2u^2-3/2n_1^2u^4)^{1/2}}. \tag{13}$$

Transforming this expression, we put $u=\nu^{-1}(\sqrt{1+2\nu^2A^2}-1)^{1/2}\cos\varphi$, $A\equiv C/s$, $\nu\equiv\sqrt{3}n_1/s=[3\kappa^2\sin^2\theta/(\kappa^2\sin^2\theta+\cos^2\theta)]^{1/2}$, which gives

$$\frac{V}{n_2s}\frac{d\psi}{(1+2\nu^2A^2)^{1/4}}=2\sqrt{1-\mu^2\sin^2\varphi}\,d\varphi-\frac{d\varphi}{(1-\mu^2\sin^2\varphi)^{1/2}},$$

$$\mu^2=\frac{1}{2}\left(1-\frac{1}{(1+2\nu^2A^2)^{1/2}}\right).$$

Introducing the notation $a\equiv Vn_2^{-1}s^{-1}(1+2\nu^2A^2)^{-1/4}$ and going over from the variables y_1,z_1,t_1 to the variables y,z,t, we can write the solution of Eq. (6) in parametric form:

$$\tilde{B_z}=\tilde{B_m}\cos\varphi(\Theta(\mathbf{r},t)), \tag{14}$$

$$\Theta(\mathbf{r},t)\equiv k_yy+k_zz-\omega_Nt+\Theta_0=2E(\varphi,\mu)-K(\varphi,\mu), \tag{15}$$

where

$$\omega_N=(1+2\nu^2A^2)^{1/4}\omega_l;$$

$$k_y\equiv k\sin\theta=an_1/L;\quad k_z=k\cos\theta=\kappa an_2/L;$$

$$\tilde{B_m}=(b_0/\nu)(\sqrt{1+2\nu^2A^2}-1)^{1/2}; \tag{16}$$

$$K(\varphi,\mu)=\int_0^{\varphi}\frac{d\varphi}{(1-\mu^2\sin^2\varphi)^{1/2}};$$

$$E(\varphi,\mu)=\int_0^{\varphi}(1-\mu^2\sin^2\varphi)^{1/2}d\varphi$$

are elliptic integrals of the first and second kind and Θ_0 is the initial phase. Equation (15) defines implicitly φ as a function of $\Theta(\mathbf{r},t)$.

Using the property

$$K\left(n\frac{\pi}{2},\mu\right)=nK\left(\frac{\pi}{2},\mu\right)\equiv nK(\mu),$$

$$E\left(n\frac{\pi}{2},\mu\right)=nE\left(\frac{\pi}{2},\mu\right)\equiv nE(\mu)$$

of elliptic integrals, where n is an integer, we can easily verify that the magnetic field of the wave is a periodic function of the variable Θ with the period $4f(\mu)$, where $f(\mu)=2E(\mu)-K(\mu)$. With variation of Θ, the function $B_z^{\sim}(\Theta)$ oscillates, assuming the maximum value $+B_m^{\sim}$ and the minimum value $-B_m^{\sim}$ at the points $\Theta_+=4nf(\mu)$ and $\Theta=2(2n+1)f(\mu)$ respectively and vanishing at $\Theta=(2n+1)f(\mu)$.

The varying field $B_z^{\sim}(\mathbf{r},t)$ depends on the arbitrary parameter A having the following physical meaning: the product b_0A is the amplitude of a linear wave. The extent of nonlinearity of the wave process is characterized by the quantity ν^2A^2. If $\nu^2A^2\ll 1$, the functions $\mu(A,\theta)$ and $B_m^{\sim}(A,\theta)$ can be expanded into power series in ν^2A^2:

$$\mu^2=\frac{1}{2}\nu^2A^2\left(1-\frac{3}{2}\nu^2A^2\right),$$

$$\tilde{B_m}=b_0A\left(1-\frac{1}{4}\nu^2A^2\right). \tag{17}$$

In the main approximation in ν^2A^2, we have $\varphi(\mathbf{r},t)=\Theta(\mathbf{r},t)$, and formula (14) is transformed into a harmonic wave with amplitude b_0A. The range of values $\cos^2\theta\gg\kappa^2$ corresponds to a weakly nonlinear mode. In this case, $\nu^2\sim\kappa^2/\cos^2\theta$, and we can easily obtain from (14) and (15) the following expression for values of A of the order of unity (accurate to ν^2A^2):

$$\tilde{B_z}(\mathbf{r},t)=\tilde{B_m}\left\{\left(1+\frac{3}{16}\mu^2\right)\right\}\cos\Theta_1(\mathbf{r},t)-\frac{3}{16}\mu^2\cos 3\Theta_1(\mathbf{r},t)\Bigg\}, \tag{18}$$

where

$$\Theta_1(\mathbf{r},t)=\left(1+\frac{3}{4}\mu^2\right)\Theta(\mathbf{r},t).$$

As the value of $\cos\theta$ decreases, a transition is made to the nonlinearity region. The wave process is essentially nonlinear for $\cos\theta\sim\kappa$ for waves with amplitude $B_m^{\sim}$ of the order of $\kappa B_0(\hbar\Omega/\varepsilon_F)$. For example, for values of $B_0\sim 10^4$ G, $\hbar\Omega/\varepsilon_F\sim 10^{-4}-10^{-3}$, $\kappa^2\sim 10^{-1}$, nonlinear distortions of the wave profile are observed for $B_m^{\sim}\sim 1$ G.

In order to take dissipations into account, we can use the standard theory of perturbations, assuming that the solution of Eq. (6) in the zeroth approximation in the small parameter η has the form (14) and (15), the only difference being that the parameter A is a slowly varying function of time. The explicit form of the function $A(t)$ is difficult to determine in view of a complex dependence of $B_z^{\sim}$ on A. However, we can easily derive simple analytic expressions for $A(t)$ in the limiting case of $t\gg\Omega\tau\cos\theta/\omega_l$. Dissipation leads to a decrease in the wave amplitude with time, and the function A is

a solution of the linearized problem for $t \gg \Omega\tau\cos\theta/\omega_l$. Neglecting nonlinear terms in Eq. (6), we obtain

$$A(t) = A(0)\mathrm{e}^{-\omega' t}, \tag{19}$$

where

$$\omega' = \frac{1}{2}\gamma\frac{k^2c^2\Omega}{\omega_p^2}(1+\kappa^2\sin^2\theta+\cos^2\theta)$$

is the damping decrement for the linear wave.

The determination of the remaining components of electromagnetic field is reduced to elementary operations of integration and differentiation. In the main order in η, the electromagnetic field of the wave has the following structure:

$$\tilde{B_y} = -\tilde{B_z}\cot\theta,$$

$$\tilde{B_x} = -\frac{\omega_N\omega_p^2}{k^2c^2\Omega\sin\theta\cos\theta}\tilde{B_m}\sin\varphi(1-\mu^2\sin^2\varphi)^{1/2},$$

$$\mathbf{E} = -\frac{c\Omega}{\omega_p^2}(\mathbf{e}_z\times\mathrm{curl}\,\mathbf{H}(\mathbf{B})), \tag{20}$$

where $\mathbf{e}_z = (0,0,1)$ is the unit vector directed along the z-axis, and the function $\varphi(\Theta)$ is defined by formula (15). In the linear approximation, the varying field is a helicoid wave.

We have considered the effect of strong magnetism of conduction electrons on the propagation of electromagnetic waves for $0 < 1-4\pi\chi \ll 1$. For $\chi > 1/4\pi$, the transient field $\tilde{B_z}$ is described by Eq. (6) where $\kappa^2 \to -|\kappa|^2$. Linearizing this equation and assuming that $\tilde{B_z} \propto \exp(-i\omega t + i\mathbf{k}\cdot\mathbf{r})$, we can easily find that the dispersion equation for $|\kappa|\sin\theta > \cos\theta$ has purely imaginary roots, and the magnetic induction distribution is unstable. The field will increase until this process is compensated by the nonlinear term. Ultimately, the evolution of instability leads to the emergence of a steady-state domain structure.[6] If dissipative effects are weak, i.e., $\Omega\tau$ is quite large, the stabilization of a steady-state domain structure must apparently be accompanied by weakly attenuating oscillations of electromagnetic field. The amplitude and wave number k_y are not independent parameters any longer, but are determined by the quantity $|\kappa|^2 \equiv 1 - 4\pi\chi|$. Equation (6) for $\chi > 1/4\pi$ is not integrable in the known elementary and transcendental functions. However, we can explain qualitatively the behavior of the system in the limiting case $t \to \infty$. On account of weak dissipative effects, the frequency and wave vector are slowly varying functions of time, such that $\omega \to 0$ and $k_z \to 0$ for $t \to \infty$. As a result, Eq. (6) is transformed into the time-independent equation $\partial H_z(B_z)/\partial y = 0$ which can easily be integrated and determines the steady-state nonuniform distribution of magnetic induction.

*E-mail: vpeschansky@ilt.kharkov.ua

[1] O. V. Konstantinov and V. I. Perel', Zh. Éksp. Teor. Fiz. **38**, 161 (1960) [Sov. Phys. JETP **11**, 117 (1960)].
[2] E. A. Kaner and V. G. Skobov, Zh. Éksp. Teor. Fiz. **45**, 610 (1963) [Sov. Phys. JETP **18**, 419 (1963)].
[3] V. G. Peschanskiĭ and D. I. Stepanenko, Zh. Éksp. Teor. Fiz. **112**, 1841 (1997) [JETP **85**, 1007 (1997)].
[4] E. N. Adams and T. D. Holstein, J. Phys. Chem. Solids **10**, 254 (1959).
[5] I. A. Privorotskiĭ, Zh. Éksp. Teor. Fiz. **52**, 1755 (1967) [Sov. Phys. JETP **25**, 1167 (1967)].
[6] J. Condon, Phys. Rev. **145**, 526 (1965).

Translated by R. S. Wadhwa

LOW-DIMENSIONAL AND DISORDERED SYSTEMS

Atomic structure of interfaces between amorphous and crystalline phases in tungsten

A. S. Bakaĭ, I. M. Mikhaĭlovskiĭ, E. V. Sadanov, T. I. Mazilova, and E. I. Lugovskaya

*National Scientific Center ''Kharkov Institute of Physics and Technology,'' 310108 Kharkov, Ukraine**
(Submitted September 21, 1998; revised November 5, 1998)
Fiz. Nizk. Temp. **25**, 282–289 (March 1999)

The atomic structure of the interfaces in amorphous–crystalline tungsten obtained *in situ* by ultrafast quenching to low temperatures from the liquid phase are investigated by the methods of field ion microscopy. A high degree of localization of imperfections and interfacial incoherence is established. The coordinates of atoms at interfaces correspond either to the crystalline or to the amorphous phase. Transition regions with intermediate positions of atoms were observed only in the vicinity of boundary regions between closely packed crystallographic planes and paraplanes. © *1999 American Institute of Physics.* [S1063-777X(99)00903-2]

INTRODUCTION

Amorphous–crystalline materials possess unique electrical, magnetic, and mechanical properties which are interesting both from the scientific and technological points of view. Peculiar physical properties of crystalline–amorphous materials are associated to a considerable extent with the presence of a developed network of interfaces in them.[1,2] The regularities of the formation of these materials by nanocrystallization of metallic glasses are essentially determined by processes on the interfaces between the amorphous and crystalline phases.[2,3] However, the interfaces in strongly disordered systems have not been investigated practically in spite of the application of the entire arsenal of high-resolution microscopic methods in view of the difficulties of deciphering microdiffractograms. In this communication, we use the methods of field ion microscopy to obtain for the first time the information on the structure of interfaces between the amorphous and the crystalline phases on atomic level.

EXPERIMENTAL TECHNIQUE

The experiments were made on a two-chamber field ion microscope with sample cooling to liquid hydrogen temperature. Helium under a pressure of 10^{-3} Pa was used as the image gas. The residual gas pressure in the working chamber of the microscope was 10^{-5}–10^{-7} Pa. Needle-shaped tungsten samples with a radius of curvature 10–15 nm and the cone angle 2–10° were prepared by electrochemical etching from a tungsten wire of purity 99.98%. After sample fixation in the microscope, the surface was polished by low-temperature field evaporation[4,5] until the formation of an atomically smooth hemispherical tip with a radius of curvature in the interval 15–50 nm. Amorphization of needle-shaped samples was carried out directly in the working chamber of the microscope by ultrafast quenching from the liquid phase,[6] created by local melting of the tip of needle-shaped samples. Amorphous and crystalline–amorphous samples were created with the help of pulse generators with a pulse duration in the interval 2×10^{-8}–5×10^{-8} s and an amplitude 5–70 kV. Pulse generators were connected in series with a high-voltage (0–25 kV) dc generator. The method of obtaining amorphous microtips by ultrafast quenching from the liquid phase in a strong electric field was described and discussed by Zaitsev and Suvorov.[6,7]

Field ion microscopic images of crystalline-amorphous samples were analyzed by using the geometrical method of computer simulation of the images.[3] In the approximation of the model of thin envelope, it was assumed that the contribution to the formation of the ion-microscopic image comes from atoms located in a surface layer of a certain finite thickness δ. The amorphous state was simulated by specifying random displacement in the limits typical of the crystalline state of compact polyhedra. Repeated random displacements was performed in the case of overlapping of atoms. It was taken into account that the thickness of the envelope image δ_a for amorphous tungsten was smaller than the corresponding parameter δ_c for samples in the crystalline state.[8] The geometrical model of field ion images is simplified and cannot ensure, among other things, a correct description of the surface radial distribution function in the amorphous state. At the same time, it will be shown below that this model satisfactorily reflects the main regularities of variation of atomic configurations at the interfaces in crystalline–amorphous metals. The simultaneous observation of the crystalline and amorphous phases allows us to determine local magnification to a high degree of accuracy (with an error up to 2–5%), which eliminates difficulties in the interpretation of field emission images of amorphous metals considered by Nordentoft.[9]

Characteristic atomic displacements at internal interfaces in solids normally occur in the range up to 0.1 nm,[1] which is beyond the standard resolution of the field ion microscope (0.27 nm). However, In accordance with the analysis carried out by Mikhailovskij,[10] subatomic displacements can also be detected during the passage of the interface in the vicinity of

poles of crystallographic planes with low Miller indices with the help of indirect magnification method. This method can be applied for an analysis of the atomic structure of interfaces in the boundary regions between closely packed crystallographic planes and paraplanes in the amorphous phase. In this case, the component of the displacement vector **T** normal to the crystallographic plane can be determined:

$$\mathbf{T}\cdot\mathbf{n}=r\Delta r/R+pd_{hkl}, \tag{1}$$

where **n** is the unit vector of the normal to the crystallographic plane, r the radius of an atomic step in the crystalline phase, R the radius of sample curvature at the tip, d_{hkl} the separation between the planes, and p the integral part of the ratio $\mathbf{T}\cdot\mathbf{n}/d_{hkl}$. Here Δr corresponds to the difference in the radii of atomic steps on the boundary region between the crystallographic plane and the paraplane.

Relation (1) shows that the minimum value of atomic displacements normal to the surface is

$$(\mathbf{T}\cdot\mathbf{n})_{\min}=r\varepsilon/R, \tag{2}$$

where ε is the resolution of the microscope. In the course of field evaporation, the radius of an atomic step decreases, and the resolution of the indirect magnification method increases accordingly. However, the radius of the atomic step cannot be smaller than

$$r_{\min}=(Rd_{hkl}/2)^{1/2}. \tag{3}$$

due to the effect of collective evaporation of atoms on closely packed faces.[11] Relations (2) and (3) show that the minimum displacement in the $[HKL]$ direction recorded on (hkl) faces by ion microscopy is given by

$$\Delta\mathbf{T}_{\min}=\varepsilon(h^2+k^2+l^2)^{1/2}(H^2+K^2+L^2)^{1/2}\times[d_{hkl}/(2R)]^{1/2}/(hH+kK+lL). \tag{4}$$

Only the paraplanes that are analogs of the most closely packed crystallographic planes {110} with $d_{hkl}=0.22$ nm are formed in the amorphous phase. Accordingly, the displacement on interfaces between the crystalline and amorphous phases in typical samples with $R=50$ nm is $\Delta\mathbf{T}_{\min}=1.1\times10^{-2}$ nm. Expression (1) can also be used for determining the displacement of individual atoms relative to the crystallographic plane in incoherent segments of interfaces in amorphous–crystalline materials. In this case, Δr corresponds to the difference between the radius of an atomic step on a crystallographic face and the distance to the pole of the face of the atom being analyzed in the amorphous phase. A geometrical analysis shows that the accuracy of the measurements of atomic displacements on incoherent segments of interfaces with the help of indirect magnification method is slightly lower. While estimating the minimum resolution of atomic displacement, we must take into account the indeterminacy in the position of atoms along the normal to the surface within the thickness of the envelope image: $\Delta\mathbf{T}_{\min}=(\mathbf{T}\cdot\mathbf{n})_{\min}+\delta_a$, where δ_a is the thickness of the envelope image in the amorphous phase. In this case, however, no limitations associated with the effect of collective field evaporation are absent, and the thickness of the envelope image is relatively small (see above). Thus, the minimum resolvable displacements along the normal to the surface at interfaces of crystalline–amorphous materials in the indirect magnification method lie in the interval $(1-2)\times10^{-2}$ nm.

DISCUSSION OF RESULTS

A. Amorphization of needle-shaped microcrystals

Our experiments proved that melting of tips of needle-shaped microcrystals by pulses of duration approximately equal to half the amplitude $(4-5)\times10^{-8}$ s with the voltage drop time $\sim10^{-8}$ s is optimal for obtaining amorphous and crystalline–amorphous structure. As the duration of pulsed increases, the melting of needle-shaped samples leads to an increase in the radius of curvature by more than an order of magnitude, which complicates their ion-microscopic analysis. The optimum amplitude of pulses was varied from 5 to 30 kV depending on the radius of curvature and was chosen so that the electric field strength was 15–25% higher than the threshold voltage of low-temperature evaporation. The threshold voltage of the evaporating field of tungsten at 21 K amounts to 5.8×10^8 V/cm. A comparison with the data presented in Ref. 12 shows that the ponderomotive forces emerging in this case exceed considerably the ultimate strength of the metal.[4] As a result, most of samples were destroyed under pulse loading. The observations in field microscope (mass analyzer),[13] the detachment of the tips of the samples was accompanied by a strong increase in the current of multiply charged ions. Most of atoms evaporated in the form of 2–4-fold ions, but 5–6-fold ionized atoms were also observed. The ion current of density $(2-5)\times10^6$ A/cm^2 flowing at the sample tip resulted in a vacuum breakdown, melting of the tip of the needle-shaped sample, and an increase in its radius of curvature by an order of magnitude and higher. The estimates of the time of cooling of a conical tip show that it does not exceed 10^{-8} s due to the emergence of high temperature gradients. The cooling rate of tips can be as high as $10^{10}-10^{11}$ deg/s, which is considerably higher than the quenching rate during the stabilization of the amorphous state in macroscopic volumes.[14] The structure obtained as a result of ultrafast quenching is stable at least at 21–78 K. The stabilization of the amorphous state can be associated with microscopic doping of surface layers during the vacuum breakdown accompanied by an intense mass transfer between the electrodes.[15]

As a result of pulse melting and ultrafast quenching, the tips of more than 80% of the samples were smoothed to the radii of curvature at the tip from the interval 10^2-10^4 nm and did not ensure the level of field strength required for the ionization of the image gas for the maximum working voltage. As a result of competing action of surface tension and electric field strength, microtips[7] were formed on the surface of the samples. The radii of curvature of a part of the tips were smaller than 50 nm, which ensured the obtaining of stable ion-microscopic images. Most of microtips has the crystalline structure under optimal conditions of pulse treatment, but approximately 10% of newly formed microtips were in the amorphous or amorphous–crystalline states. Figures 1a and b show typical ion-microscopic images of needle-shaped samples before and after the transition to the

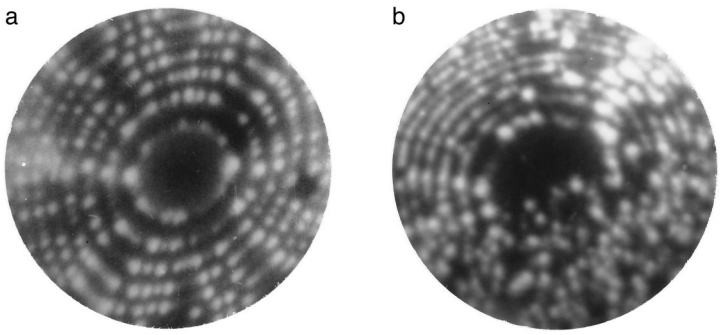

FIG. 1. Field-ion microscopic images of a tungsten sample before (a) and after (b) transition to the amorphous–crystalline state.

amorphous–crystalline state respectively. The images of the amorphous phase are characterized by almost complete lack of regularity in the arrangement of atoms in the surface layer and are described satisfactorily on the basis of the geometrical model (Fig. 2). As in the case of amorphous alloys of the transition metal–metalloid type,[9,16] a decrease in the concentration of surface atoms contributing to the formation of ion-microscopic images is observed. Figure 3 shows the distributions of f_ρ over local concentrations ρ of surface atoms in the amorphous (curve *1*) and crystalline (curve *2*) phases. The ratio of half-widths of distributions for the crystalline and amorphous phases is 2.8. The average density of atomic images in the crystalline state is 2.2 times higher than the corresponding value in the amorphous state. This confirms the conclusion on the comparatively small thickness of the atomic layer in the amorphous phase, participating in the formation of the field ion image.[9] According to our results, the thicknesses δ_a and δ_c of envelope images in a computer simulation of field ion images were assumed to be equal to 8×10^{-3} and 2×10^{-2} nm, respectively.

Microtopography of interfaces

An analysis of the morphology of interfaces in crystalline–amorphous tungsten revealed their structural and topographic nonuniformity. Microtopography of interfaces reconstructed from the series of ion-microscopic images obtained during field evaporation was characterized by alternation of extended plane regions (see Fig. 1b) and microscopically rough regions with nanosteps having a height 1–5 nm and width 2–15 nm (Fig. 4). Crystallogeometric analysis proved that extended plane regions are oriented along planes with low Miller indices. For example, a fragment of a plane region of the interface presented in Fig. 1b is oriented along the closely packed plane {101}. An important feature of microtopography of interfaces in crystalline–amorphous tungsten and grain boundaries in the initial crystalline material is the perfect atomic smoothness of extended plane regions of interfaces. Under ordinary working conditions of field ion microscopes, which correspond to the field strength of the best image,[4] the contribution to image formation comes only from 25–30% of surface atoms in view of the above-mentioned small thickness δ of the surface layer image (especially in the amorphous phase). This complicates the nanotopographic analysis of interfaces. However, an analysis of a series of micrographs obtained under controllable evaporation shows that traces of interfaces are strictly rectilinear, indicating the atomic smoothness of the extended plane interface.

In microscopically rough regions, no tendency to preferential orientation along low-index planes was observed. As a rule, planes cannot be identified in view of a small length of nanosteps. However, the presence of a broad and nearly continuous spectrum of angles between the traces of the

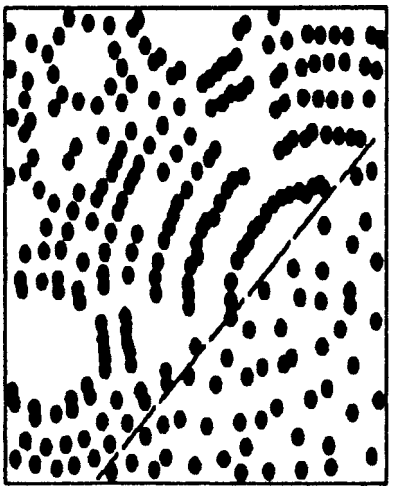

FIG. 2. Computer model of an ion-microscopic image of crystalline–amorphous tungsten formed by low-temperature field evaporation.

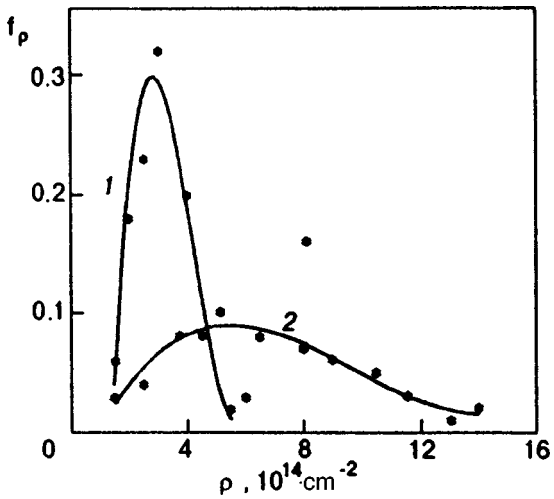

FIG. 3. Distribution of concentration of surface atoms in the amorphous (curve *1*) and crystalline (curve *2*) phases in crystalline–amorphous tungsten.

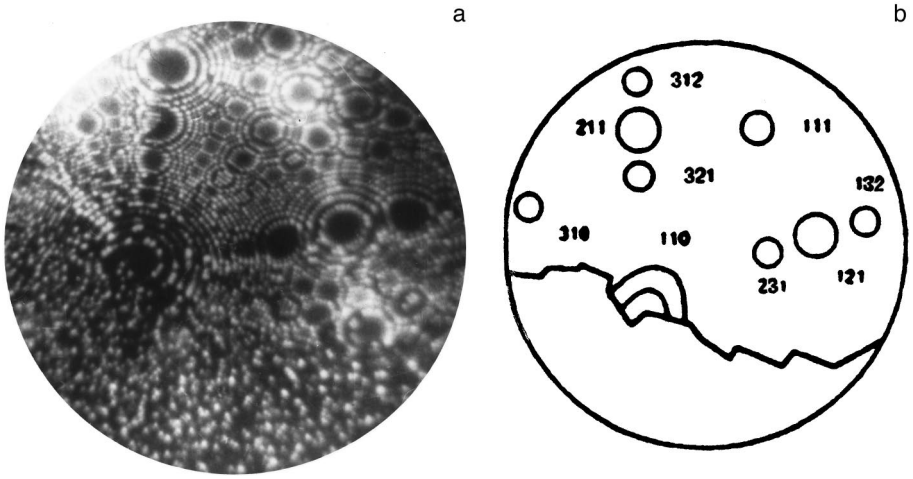

FIG. 4. Ion-microscopic image (a) and stereographic projection (b) of a microscopically rough region of the interface.

emergence of steps on the surface (Fig. 4b) indicate that most steps are oriented along high-index planes.

Incoherence of interfaces

Regularity in the arrangement of atoms in the crystalline phase is preserved up to the interface (Fig. 5). The configuration of concentric atomic steps corresponds to computer images of perfect single crystals obtained by using the geometrical model (see Fig. 2). This indicates the incoherence of the interface between the crystalline and amorphous phases. In the case of a coherent conjugation, the existence of a transition layer and the presence of local distortions of crystal lattice should be expected in the boundary region.

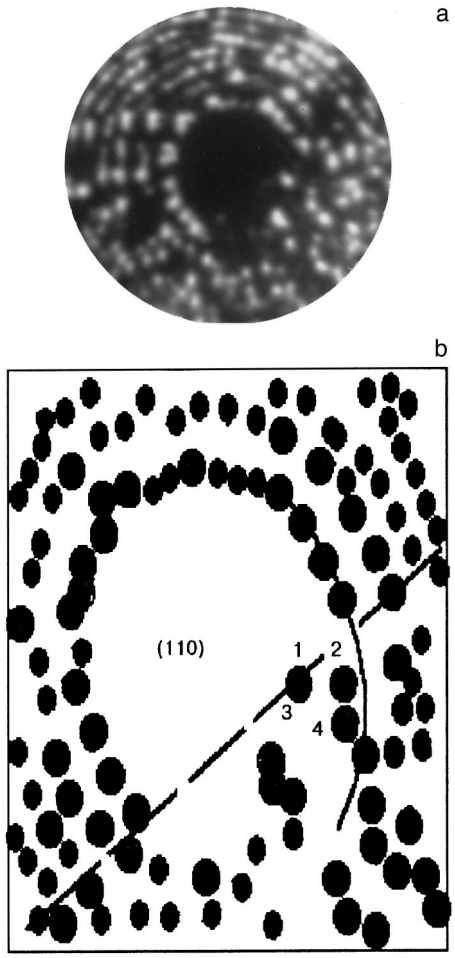

FIG. 5. Ion-microscopic image (a) and schematic diagram (b) illustrating the presence of subatomic displacements at the interface. Figures denote atoms in the amorphous phase, that are the closest to the interface.

Atomic displacements were determined from the local deformation at the boundary of concentric atomic steps on closely packed atomic faces by using the indirect magnification method. The atomic displacements in the crystalline phase along the normal to the {110} face in the region of the core of the interface having a width up to a lattice parameter did not exceed 5×10^{-2} nm. Such displacements can be regarded as small deformations that do not change the crystalline type of atomic packing in the boundary region. A comparison with computer images (see Fig. 2) shows that the pattern of arrangement of boundary poles and atomic steps on closely packed faces typical of bcc lattices does not change in this case.

The absolute values $\Delta|h|$ of atomic displacements in the direction normal to the {110} plane in the boundary region were calculated by the method of indirect magnification on the basis of formula (1) (Fig. 6). Here N is the number of atoms in the crystalline ($N<0$) and amorphous ($N>0$) phases, which are nearest to the interface (see the diagram in Fig. 6). In the crystalline phase, the displacements $\Delta|h|<0.02$ nm were observed. It can be proved that the gradient of displacements does not exceed the deformation level generated by a lattice dislocation at the center of the {110} face. Thus, atomic displacements in the boundary region of the crystalline phase are, as a rule, in the elastic region and do not violate crystallogeometric regularity in the atomic packing. In the boundary regions of the amorphous phase no conjugation effects are observed as a rule. Irregular displacements are typical even for atoms nearest to the boundary. The displacements increase abruptly up to 0.1 nm, and the form of distribution of atomic displacements does not change as we move away from the interface. Thus, the structural width of the interface determined from the length of the region with a peculiar morphology of atomic packing in the core of the interface can be assumed to be zero.

The observed incoherence and small width of interfaces

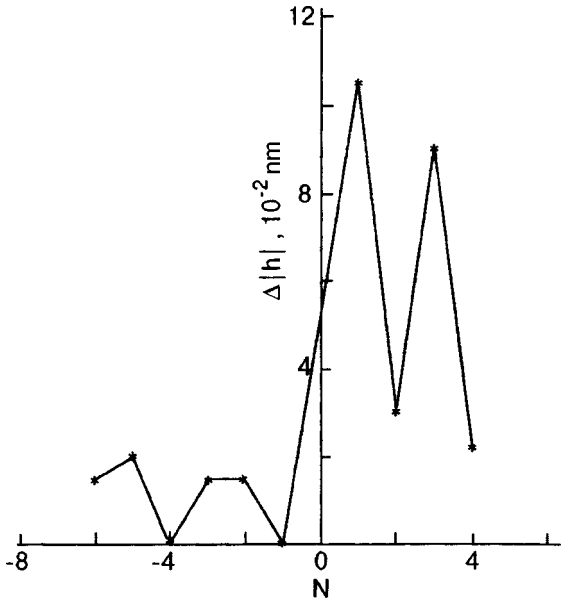

FIG. 6. Subatomic displacements near the interface between the crystalline ($N<0$) and amorphous ($N>0$) phases (N is the number of an atom closest to the interface).

between the crystalline and amorphous phases may play a significant role in diffusive transport of atoms and in the formation of mechanical properties of crystalline–amorphous materials. It can be stated on the basis of the above peculiarities of the interfaces under investigation and proceeding from the topological–geometrical considerations similar to those proposed in Ref. 2 that the network of boundary lattice sites contains coinciding and noncoinciding sites. Boundary sites cannot form translation-invariant structures either in view of the lack of translational invariance in the amorphous structure. Consequently, the structure and properties of crystalline–amorphous interfaces must be similar to those on intercluster boundaries in amorphous alloys. Among other things, we can expect that at high temperatures, when diffusive transport over the boundaries of atoms becomes significant, the main mechanism of plastic deformation in crystalline–amorphous metals and alloys is a diffusive–viscous flow over internal interfaces as in metallic glasses.[2]

Local atomic conjugation at interfaces

The methods of high-resolution transmission electron microscopy[17] and field ion microscopy[18] were used earlier to detect the regions of intermediate ordering in amorphous alloys. These regions had a size of 1.5–2.5 nm and contained closely packed but noticeably distorted atomic planes (paraplanes). The available data indicate the coherent integration of paraplanes with the amorphous matrix and the presence of comparatively large strains. Similar paraplanes were also observed in our experiments.

In the cases when crystallographic planes with low Miller indices intersected an interface at an angle close to 90°, microscopic regions in which atoms formed closely packed planar groups (paraplanes) were observed in the boundary region of the amorphous plane.

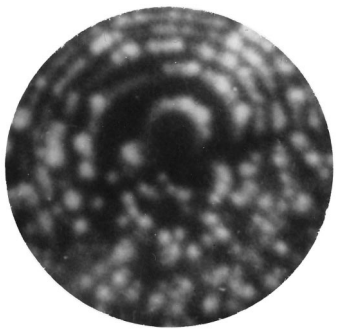

FIG. 7. Conjugation of the crystallographic plane {110} with a closely packed paraplane.

Figure 7 shows an ion-microscopic image of the interface containing the pole [110]. A semicircular atomic step at the (110) face of the crystal conjugates at the interface with a deformed atomic layer (paraplane) in the amorphous phase. The absence of detectable ion-microscopic fractures in atomic steps at the interface indicates a high extent of orientational correspondence of contacting crystallographic planes and paraplanes.

In contrast to planes in the crystalline phase, paraplanes were characterized by the presence of small displacements of atoms. The emergence of atomic images within a semicircular step in the amorphous phase in accordance with the geometrical model of the formation of field ion images indicates a displacement of atoms along the normal to a paraplane. The magnitude of the displacement is proportional to the difference between the step radius and the distance between the atom under investigation and the pole of the paraplane. The distribution of f_d over atomic displacements Δh normal to paraplanes and calculated by the indirect magnification method on the basis of an analysis of a series of ion-microscopic images is shown in Fig. 8. We analyzed displacements in the boundary paraplanes (see Fig. 7) whose length was normally 2–3 nm. Displacements Δh can be regarded as a measure of deviation from planarity in the

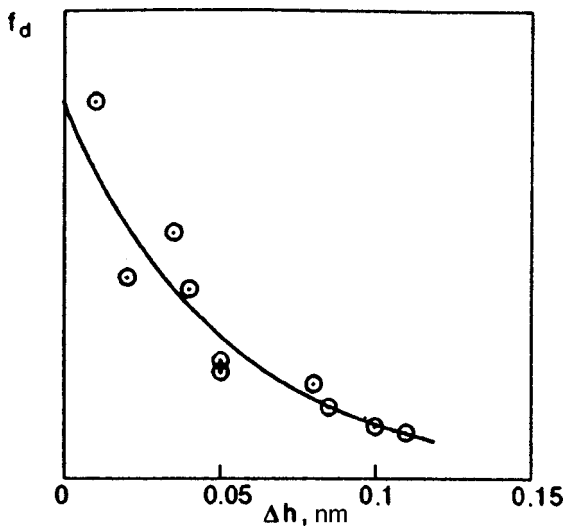

FIG. 8. Distribution of atomic displacements in the boundary closely packed paraplanes.

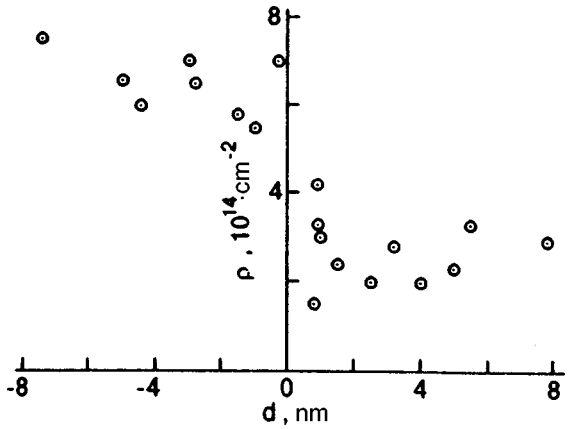

FIG. 9. Dependence of the local concentration of surface atoms on the distance d to the interface.

arrangement of atoms in paraplanes in the boundary regions of the amorphous phase. It should be noted that the distortion of atomic paraplanes in the regions of coherent conjugation with the amorphous environment was observed with the help of high-resolution electron microscopy[17] as well as low-temperature field ion microscopy.[2,18] The estimates obtained by the indirect magnification method show that mutual displacement of planes and paraplanes does not exceed 2×10^{-2} nm. Alternation of mismatched regions and domains of orientational correspondence of closely packed planes and paraplanes was usually preserved during field evaporation of the sample to a depth of 10^2-10^4 nm.

Width of interfacial core

Physical and mechanical properties of interfaces are determined to a considerable extent not only by the structural width, but also by the size of the region with an elevated level of deformation energy. For example, while determining the width of interfaces, we must take into account the peculiarities of the deformation field beyond the structural width of the interface.[2,19]

Considering that atomic displacements in the region of cores of the interfaces[1] are comparable with the thickness δ of the envelope image, we can use the effect of variation of δ under amorphization of metals in order to estimate quantitatively the width of the core of the interface. Thus, the width of the interface core can be determined from the width of the region of continuous variation of the thickness of the envelope image in the interval $\delta_a<\delta<\delta_c$. The inhomogeneity of the structure of interfaces between the crystalline and amorphous phases mentioned above is also manifested in the presence of a considerable dispersion in the values of local width of interfacial cores. Among other things, interfacial regions with a virtually jump-like variation of density are observed in regions of width 0.3–0.4 nm.[8] The width of the core of such an interface can be assumed to be equal to a lattice parameter, which is much smaller than the width of the core of crystallite boundaries.[20] In some cases, the width of the region with varying values of δ_a attained 1.0 nm. Figure 9 shows a typical dependence of the average surface density of atoms on the distance d to the interface. Negative values correspond to the crystalline phase as before. A considerable variation of the surface density is observed in a region having a width corresponding to three atomic spacings. Thus, the width of the core of the interface between the crystalline and amorphous phases in different regions amounts to 1–3 atomic spacings.

CONCLUSIONS

The method of indirect magnification in the field ion microscopy ensures the detection of subatomic displacements at the interface between the crystalline and amorphous phases with an accuracy exceeding the resolution of the microscope by an order of magnitude and higher. The application of this method in our experiments has made it possible to obtain for the first time the experimental information on the structure of the interfaces between the amorphous and crystalline phases at atomic and subatomic levels.

(1) Microscopic topography of interfaces was characterized by alternation of extended plane segments oriented predominantly along the planes with low Miller indices and microscopically rough regions containing nanosteps. Extended plane regions were perfectly atomically smooth.
(2) Atomic displacements in the boundary region of the crystalline phase do not disturb the crystallogeometrical regularity of atomic packing. As a rule, conjugation effects are not observed in the boundary regions of the amorphous phase: irregular displacements are typical even for atoms closest to the interface. The structural width of the interface determined from the width of the region with a peculiar morphology in atomic packing in the interfacial core can be assumed to be equal to zero.
(3) The effect of conjugation of crystallographic planes and paraplanes was observed in separate regions of the interface, and a high extent of their orientational correspondence was indicated.
(4) It is shown that the width of interfacial region in which peculiarities of deformation field were observed with the help of ion microscopy is considerably larger than the structural width of the interface.

Thus, the high-resolution methods of field ion microscopy are used in this work to establish the incoherence and atomic sharpness of the interface between the amorphous and crystalline phases. Structural inhomogeneity of the interfaces was observed. Noncontracting regions alternate with the regions of orientational correspondence of closely packed crystallographic planes and paraplanes in the amorphous phase.

*E-mail: mikhailovskij@kipt.kharkov.ua

[1] A. P. Sutton and R. W. Balluffi, *Interfaces in Crystalline Materials*, Clarendon Press, Oxford (1995).
[2] A. S. Bakai, in *Glassy Metals III* (ed. by H. Beck and H.-J. Guntherodt), Springer, Heidelberg (1994).
[3] H. Y. Tong, B. Z. Ding, H. G. Jiang *et al.*, J. Appl. Phys. **75**, 654 (1994).
[4] E. W. Muller and T. T. Tsong, *Field Ion Microscopy, Field Ionization and Field Evaporation*, Pergamon Press, New York (1978).
[5] I. M. Mikhaĭlovskiĭ, V. A. Ksenofontov, and T. I. Mazilova, Pis. Zh. Éksp. Teor. Fiz **65**, 542 (1997) [JETP Lett. **65**, 537 (1997)].

[6] S. É. Zaĭtsev and A. L. Suvorov, Preprint Inst. Theor. Exper. Phys. No. 154, Moscow (1987).
[7] A. L. Suvorov, *Structure and Properties of Surface Atomic Layers in Metals* [in Russian], Énergoatomizdat, Moscow (1989).
[8] A. S. Bakaĭ, I. M. Mikhaĭlovskiĭ, E. V. Sadanov *et al.*, [JETP Lett. **66**, 504 (1997)].
[9] L. Nordentoft, Philos. Mag. B **52**, L21 (1985).
[10] I. M. Mikhaĭlovskiĭ, Fiz. Tverd. Tela (Leningrad) **24**, 3210 (1982) [Sov. Phys. Solid State **24**, 1822 (1982)].
[11] I. M. Mikhaĭlovskiĭ, Zh. I. Dranova, V. A. Ksenofontov, and V. B. Kul'ko, Zh. Éksp. Teor. Fiz. **76**, 1309 (1979) [Sov. Phys. JETP **49**, 664 (1979)].
[12] I. M. Mikhaĭlovskiĭ, P. Ya. Poltinin, and L. I. Fedorova, Fiz. Met. Metalloved. **56**, 186 (1983).
[13] I. M. Mikhaĭlovskiĭ, V. A. Ksenofontov, E. V. Sadanov, and O. A. Velikodnaya, Pis. Zh. Éksp. Teor. Fiz **57**, 39 (1993) [JETP Lett. **57**, 40 (1993)].
[14] K. Suzuki, H. Fujimori, and K. Hasimoto, *Amorphous Metals* [Russian transl.], Metallurgiya, Moscow (1987).
[15] G. A. Mesyats and D. I. Proskurovskiĭ, *Pulsed Electric Discharge in Vacuum* [in Russian], Nauka, Moscow (1984).
[16] A. S. Bakai, V. B. Kulko, I. M. Mikhailovskij *et al.*, Non-Crystalline Solids **182**, 315 (1995).
[17] Y. Hirotsu, M. Uehaza, and Y. Ueno, J. Appl. Phys. **59**, 3081 (1986).
[18] I. M. Mikhaĭlovskiĭ, L. I. Fedorova, and P. Ya. Poltinin, Fiz. Met. Metalloved. **76**, 123 (1993).
[19] P. A. Bereznyak, O. A. Velikodnaya, T. I. Mazilova, and I. M. Mikhaĭlovskiĭ, JETP Lett. **59**, 542 (1994).
[20] A. N. Orlov, V. N. Perevezentsev, and V. V. Rybin, *Grain Boundaries in Metals* [in Russian], Metallurgiya, Moscow (1980).

Translated by R. S. Wadhwa

Photocurrent generation in single electron tunneling transistors

Ola Tageman

*Department of Applied Physics, Chalmers University of Technology and Göteborg University, S-41296 Göteborg, Sweden**

(Submitted October 14, 1998)
Fiz. Nizk. Temp. **25**, 290–297 (March 1999)

A single-electron tunneling transistor (SET) with a non-equilibrium mode population in one of the leads is analyzed theoretically. We model transport through a dot coupled to a channel, both formed by gates from the two-dimensional electron gas of a GaAs/AlGaAs heterostructure. The non-equilibrium mode population, which is induced by coherent THz-pumping in the channel, produces empty states below the Fermi level for electrons to tunnel into. A photocurrent arises, which is periodically saw-tooth peaked with respect to the voltage on a central gate. For intense THz-fields the peaks display plateaus that reflect the energy dependence of the mode population. We also predict a high-gain $V_{\text{in}}/V_{\text{out}}$ transfer-characteristic, similar to that of a current biased SET. © *1999 American Institute of Physics.* [S1063-777X(99)01003-8]

1. INTRODUCTION

Charging effects are becoming increasingly important in transport experiments, as fabrication technology for nano-scale systems develops. These effects appear in different kinds of circuits that have one thing in common—they all incorporate a small semi-isolated island in which the number of electrons is strongly quantized.[1–3] At low driving voltage, fluctuations of the charge on this island are suppressed due to Coulomb interaction, except if the electrostatic potential of the island is carefully tuned.[4] This Coulomb blockade mechanism is utilized in the Single Electron Transistor (SET), to modulate the conductance through the island by varying the potential on a nearby gate electrode.[5]

When alternating fields are introduced in SETs and related systems, interesting effects arise, and large amount of physical information can be gained. By applying MHz-signals to one or several gates, one can generate precise currents in the pA-range,[6–8] and by monitoring the reflection of a microwave signal from the SET, one can follow charge fluctuations with high accuracy.[9] In these examples the alternating field acts in a quasi-static way, but if the frequency is raised further, then high-frequency effects appear. For example, if a microwave signal in the range 10–75 GHz is fed to the gate of a planar semiconductor SET, both photon assisted tunneling across the barriers and photo-excitations inside the island, can be observed.[10]

So far, no special attention has been paid to utilizing ac-fields for inducing a non-equilibrium electron distribution inside the leads of a SET. Such a distribution can clearly open new ways of tunneling into and out of the island. In a metallic lead of typical dimensions this will have a negligible effect because of strong screening and poor size-quantization. However, in a quasi one-dimensional conductor, such as a split-gate channel in the two-dimensional electron gas ($2D$EG) of a GaAs/AlGaAs heterostructure, the situation is different. Recent transport experiments employing THz-fields touch upon this issue.[11,12]

In this work we consider, theoretically, how the performance of a SET will be influenced by the application of an electric THz-field in one of the leads. The important new ingredient is a non-equilibrium mode-population, which results in a photocurrent generation in the SET. For intense THz-fields we find a short-circuit current that reveals information about the non-equilibrium distribution function in the lead. Considering instead weak THz-fields in an open circuit configuration, we find a $V_{\text{in}}/V_{\text{out}}$ transfer characteristic similar to that of the current biased SET.

2. THEORY

The system under consideration is described in Fig. 1. We choose to have a gated-$2D$EG realization in mind when modeling the system. Such a realization allows both Coulomb-blockade effects and ballistic motion over many electron wavelengths.[13,14] When applying a negative voltage to the gates, the electrons are confined to a dot and a channel, plus to reservoirs on the two sides. We shall refer to the channel-side reservoir as the collector and to the reservoir on the other side as emitter. The emitter is grounded to a back-gate and the collector is also grounded but via a load resistor R_L. Our aim is to calculate the current I through, or the voltage V across this load resistor, as a function of the electrostatic potential on the dot, which can be tuned via the voltage V_g. We use the standard approach, ignore co-tunneling and calculate the current from a master equation.[15,16] The influence of discrete states in the dot will be ignored in order to highlight the influence of THz-pumping.[17] We take the band-bottom in the emitter as our reference of energy.

As long as the width of the channel varies slowly on the scale of the electron wavelength, elastic scattering between transverse modes may be ignored.[18] The resulting mode-potentials are sketched in the lower part of Fig. 1. We choose the width of the channel such that only the lowest mode enters the channel. However, by the application of a coherent

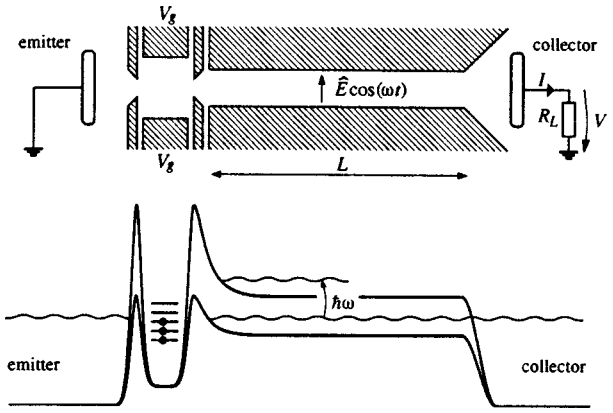

FIG. 1. Sketch of the model system and the corresponding energy diagram. A coherent electric THz-field, polarized across the collector-channel induces a non-equilibrium mode population.

electric THz-field of strength $\hat{E}$, across the channel, we excite higher modes inside the channel, provided that the angular frequency ω is chosen to match the mode-potential separation there fairly well.

We consider a situation in which, even if higher modes are brought to life by absorption of a number of energy-quanta $\hbar\omega$ from the THz-field, only the lowest mode is involved in the tunneling process. This is realistic for a split-gate induced tunneling barrier. If $\hbar\omega$ matches the mode potential separation inside the channel, the kinetic energy in an excited mode will be the same as in the lowest mode. However, at the end of the channel, where the transverse confinement is made stronger by separate split-gates, the kinetic energies will differ. The stronger confinement leads to a larger mode potential separation, as indicated in Fig. 1. Consequently, the kinetic energies decrease more in excited modes. For this reason it is realistic to assume a suppressed tunneling for excited modes.

Population of collector modes

We assume a parabolic confining potential in the channel.[19] Introducing the parameter U_0, which describes a lifting of the bottom of the well, and Ω, which describes how narrow the channel is, we write

$$U(y)=U_0+\tfrac{1}{2}m^*\Omega^2y^2, \tag{1}$$

where m^* is the effective mass and y is the transverse coordinate. The problem of finding the population of different modes in a pumped straight parabolic channel has been addressed previously.[20] It was shown that if the deviation from perfect parabolicity is sufficiently large we can forget about coupling to higher modes. We assume that this is the case and confine our interest to the lowest two modes. It is then straightforward to find an analytical solution.

Starting from the following expression (in which $e>0$ is the elementary charge) for the kinetic energy $K_n(E)$ in mode n:

$$K_n(E)=E+eV-U_0-\left(n-\frac{1}{2}\right)\hbar\Omega+(n-1)\hbar\omega, \tag{2}$$

using the known expression[20] for the coupling energy V_ω:

$$V_\omega=\frac{e\hat{E}}{2\omega}\left(\frac{\hbar\Omega}{2m^*}\right)^{1/2}, \tag{3}$$

and assuming that $|\hbar(\omega-\Omega)|\ll K_1(E)$, $K_2(E)$ and that $V_\omega \ll \hbar\omega$ we get for the population $\xi(E)$ of the lowest mode at the end of the channel

$$\xi(E)=1-\gamma\sin^2[q(E)L]. \tag{4}$$

Here

$$\gamma=\left[1+\left(\frac{\hbar(\omega-\Omega)}{2V_\omega}\right)^2\right]^{-1}, \tag{5}$$

$$q(E)=\overline{q}(E)\left[\left(\frac{\hbar(\omega-\Omega)}{4\overline{K}(E)}\right)^2+\left(\frac{V_\omega}{2\overline{K}(E)}\right)^2\right]^{1/2},$$

$$\overline{q}(E)=\left[\frac{2m^*\overline{K}(E)}{\hbar^2}\right]^{1/2},$$

$$\overline{K}(E)=\frac{K_1(E)+K_2(E)}{2}.$$

There is a strong similarity between Eq. (4) and Rabi's formula for the time developments of a two-level system. Rabi's formula describes population oscillations in time in a two-level system, while our Eq. (4) describes population oscillations between transverse modes, as a function of the spatial coordinate along the channel. The wave-vector of oscillation along the channel is given by $q(E)$ and the resonance strength by γ.

Master equation approach

By $E_d(E,N)$ we denote the energy, relative to the bottom of the well in the dot, of an electron that has tunneled into the dot starting from an energy E, when the number of electrons on the dot increases from $N-1$ to N. If an electron is to tunnel out of the dot into a lead at energy E, thereby decreasing the number of electrons from N to $N-1$, it must start at this very same energy $E_d(E,N)$. We use the following capacitance model for relating $E_d(E,N)$ to E:

$$E_d(E,N)=E-N\frac{e^2}{C_\Sigma}+eV_g\frac{C_g}{C_\Sigma}+eV\frac{C_c}{C_\Sigma}+\text{const.} \tag{6}$$

Here C_Σ is the total capacitance of the dot; C_g is the capacitance between the gate electrodes and the dot; C_c is the capacitance between the collector and the dot. The electrostatic potential of the dot can be continuously tuned via the gate potential V_g and it is dependent also on the electrostatic potential V in the collector. In addition there are contributions to the potential energy on the dot from the point contact gates and from the rest of the surroundings, in particular from random offset charges. We treat this as an unknown constant in Eq. (6). It corresponds to a shift in V_g, which we shall not try to determine.

We assume that the electrons inside the dot, after each tunneling event, quickly thermalize to a Fermi–Dirac distribution with a temperature T given by the surrounding and with a chemical potential $\mu(N)$ given by the number of electrons inside the dot. It then makes sense to introduce $P(N)$,

the probability for having N electrons on the dot. Furthermore, we can use $f[E_d-\mu(N)]$ for the probability of finding an electron in a single-electron energy-level E_d, given that there are N electrons on the dot, where

$$f(x)=[e^{x/kT}+1]^{-1}. \tag{7}$$

By assuming that $kT \gg \Delta E$ we are allowed to use a continuum description in the dot, and we take the density of states there, ρ_d, to be constant. Moreover, we assume that $\Delta E \ll e^2/C_\Sigma$ and therefore ignore the variation of $\mu(N)$ with N. For simplicity we assume that μ is so large ($>E_F-U_0$) that its actual value has no influence other than adding to the constant in Eq. (6).

The probability distribution $P(N)$ is found from the following balance equation:

$$P(N)[W_{e\to d}(N+1)+W_{c\to d}(N+1)]=P(N+1) \times[W_{d\to e}(N+1)+W_{d\to c}(N+1)] \tag{8}$$

plus the normalization condition

$$\sum_N P(N)=1. \tag{9}$$

In Eq. (9) we have used the following definitions of the total tunneling rates: by $W_{e\to d}(N)$ we denote the rate at which electrons tunnel from the emitter into the dot when there are $N-1$ electrons on the dot to start with and thus N electrons on the dot in the final state; by $W_{d\to e}(N)$ we denote the rate for the reversed process, in which electrons leave the dot when there are N electrons on it to start with; we denote the corresponding collector rates by $W_{c\to d}(N)$ and $W_{d\to c}(N)$.

The current I, as defined in Fig. 1, can be found by summing the rates for tunneling out of and into the emitter:

$$I=-e\sum_N P(N)[W_{e\to d}(N+1)-W_{d\to e}(N)]. \tag{10}$$

Tunneling rates

The barriers are formed by split gates and the voltage on these gates is held constant. We crudely choose to ignore the dependence of the barriers on both the photovoltage V and the number of electrons on the dot N. We start from golden-rule expressions for the tunneling rates. By $\Gamma_e(E)$ we denote the rate at which electrons leave the emitter at an absolute energy E and tunnel into the dot. The same rate is used for the reverse process. By $\Gamma_c(E)$ we denote the corresponding tunneling rates from and into the collector,

$$\Gamma_{e/c}(E)=\frac{2\pi}{\hbar}|M_{e/c}(E)|^2\rho_d. \tag{11}$$

Here $M_e(E)$ and $M_c(E)$ are tunneling matrix elements which are given by some overlap integral between initial and final states. Since we are not interested in the details in these matrix elements we choose to describe tunneling by a resistance R_e for the emitter barrier and a resistance R_c for the collector barrier. Both resistances are defined at the Fermi-level.

However, the tunneling resistances R_e and R_c are energy dependent. In our case this dependence must be modeled because the pumping mechanism will depopulate the collector and allow for tunneling far below E_F. We assume an exponential decay in the tunneling rates when the energy is lowered and we introduce a tunneling-decay scale E_T for this purpose. The following form is used for the matrix elements:

$$|M_{e/c}(E)|^2=\frac{\hbar e^{(E-E_F)/E_T}}{2\pi e^2\rho_d\rho_{e/c}R_{e/c}}, \tag{12}$$

where $\rho_{e/c}$ is the density of states in the emitter/collector, which we take to be constant. With this choice all densities of states cancel and we instead introduce the tunneling resistances, which can be measured in an experiment by opening one point contact at a time.

The total rates are given by sums of partial rates associated with the different energies. Turning to a continuum description we get

$$W_{e\to d}(N)=\int_0^\infty \rho_e f(E-E_F)\Gamma_e(E)\{1-f[E_d(E,N)-\mu]\}dE,$$

$$W_{d\to e}(N)=\int_0^\infty \rho_e f(E_d(E,N)-\mu)\Gamma_e(E)[1-f(E-E_F)]dE, \tag{13}$$

$$W_{c\to d}(N)=\int_{U_0+\hbar\Omega/2-eV}^\infty \rho_c f(E+eV-E_F)\xi(E) \times\Gamma_c(E)\{1-f[E_d(E,N)-\mu]\}dE,$$

$$W_{d\to c}(N)=\int_{U_0+\hbar\Omega/2-eV}^\infty \rho_c f[E_d(E,N)-\mu] \times\Gamma_c(E)[1-f(E+eV-E_F)\xi(E)]dE.$$

3. SHORT-CIRCUIT CURRENT

When $R_L=0$ we know that $V=0$ and we can find the current from Eq. (10). In our numerical calculations we vary three important experimental variables, V_g, $\hat{E}$ and E_T. For the rest of the parameters we use the following realistic values: $R_e=R_c=200\,\mathrm{k\Omega}$, $C_\Sigma=100\,\mathrm{aF}$, $C_g=0.4C_\Sigma$, $T=0.1\,\mathrm{K}$, $E_f=14\,\mathrm{meV}$, $U_0=10\,\mathrm{meV}$, $\hbar\Omega=4\,\mathrm{meV}$ and $L=2.5\,\mu\mathrm{m}$. We assume that the frequency, or equivalently the voltage on the gates that form the channel, is tuned to resonance, i.e., $|\hbar(\omega-\Omega)|\ll 2V_\omega$ [see γ in Eq. (5)].

With our definition in Fig. 1 the current I is negative. In order to avoid confusion in our explanations we shall always plot $-I$. In Fig. 2 we plot $-I$, as a function of V_g, for a set of field strengths $\hat{E}$ ranging from 0 to 500 V/cm for three different values of the tunneling-decay scale E_T: 0.2, 0.5, and 1.0 meV. Upon increasing V_g, at some point $-I$ increases abruptly and then decays more slowly, until the next point of increase. For large E_T plateaus are seen on the decaying side, especially when $\hat{E}$ is large.

We explain this behavior in Fig. 3. An enlargement of one of the curves is shown to the left, the one with $E_T=0.5\,\mathrm{meV}$ and $\hat{E}=600\,\mathrm{V/cm}$. In the right part we illustrate the population of both charge-states and lead-states, corresponding to the cross-hair point on the current curve. Because of the pumping, depopulation appears in the

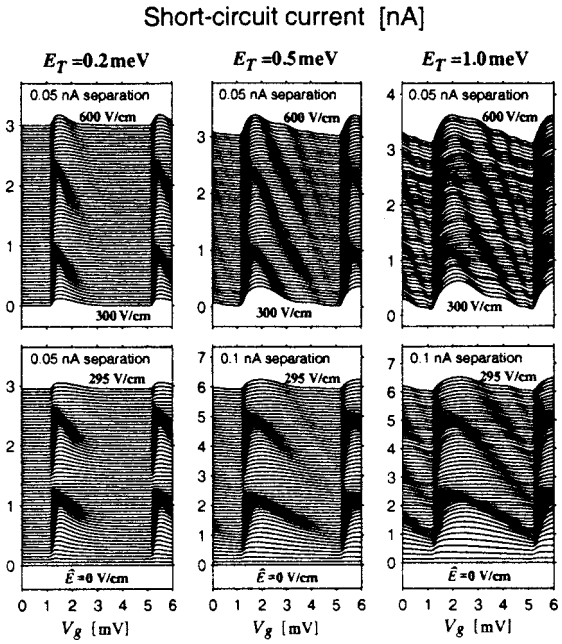

FIG. 2. Short-circuit current $-I(V_g)$ for three different values of the tunneling-decay scale E_T. Each curve corresponds to a particular value of the field strength $\hat{E}$. For clarity the curves are separated by a constant offset.

collector which means that not all levels below the Fermi-level are occupied. Such depopulation enables tunneling out of the dot.

Increasing V_g corresponds to lowering all charge-states in the dot. The dramatic increase in $-I$ occurs when a charge state falls below E_F in the emitter so that there is a way to fill the dot. To start with the inflow from the emitter limits $-I$, and therefore $-I$ rises in proportion to the lowering of this charge state.

After the top, the outflow will limit $-I$. The slow decay of the current is understandable since the outflow takes place at many different energies and we must thus bring the charge-state far down in order to shut $-I$ off completely. The tunneling-decay scale E_T determines this decay rate.

Also, the plateaus in the decay can be understood from the population diagram. The first plateau appears when the charge state passes the first population maxima as shown to the right in Fig. 3. Since the charge-state is occupied most of the time, the outflow rate from this charge-state limits the

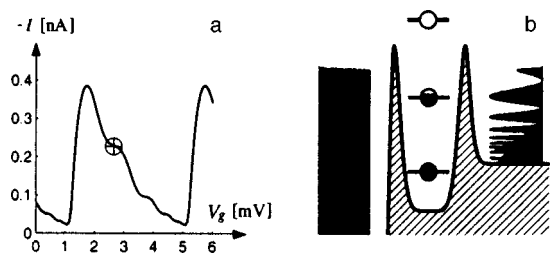

FIG. 3. Short-circuit current $-I(V_g)$ for the $E_T=0.5$ meV and $\hat{E}=600$ V/cm (a) and population diagram corresponding to the cross-hair point (b). The energy dependence in the population of collector levels gives rise to plateaus in $-I(V_g)$. Note that a population peak is aligned with a charge state for this particular choice of V_g.

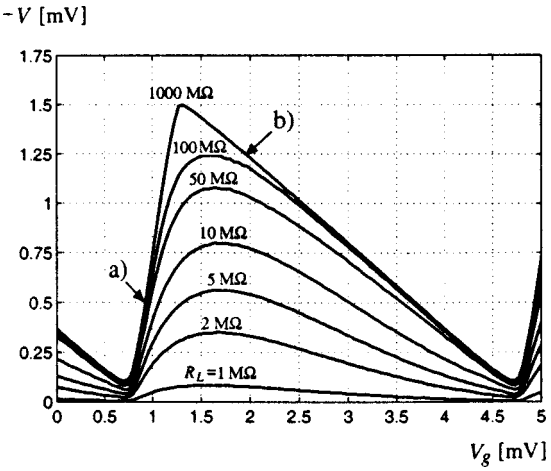

FIG. 4. Transfer-characteristic, when $\hat{E}=40$ V/cm, for different values of the load resistance. For $R_L=1000$ MΩ the voltage gain exceeds 3, but it is smaller for smaller R_L.

$-I$. But at the population maxima there are no empty states to tunnel into, which means that the outflow is insensitive to a change in V_g there. The reason why the plateau is not perfectly flat, is that as we pass a population peak there is an increasing back-flow from the collector, which tends to reduce the net flow.

As we continue increase V_g and thus lower the charge-states, $-I$ drops when we pass population minima and is steady when we pass a population maximum in a repetitive manner. The steps get smaller and smaller as the energy-period of population oscillations decreases.

4. VOLTAGE GAIN

In this section we deal with photovoltaic effects. We now assume the collector load R_L to be in the MΩ-range, allowing a significant negative collector-potential V to build up relative to the grounded emitter. The load R_L, which simulates either a voltmeter or the input of another transistor, is varied in order to demonstrate the driving capability of the device. We must now solve for the particular value of V that gives rise to a current I given by Eq. (10) that fulfills $V/I=R_L$.

We make two assumptions about the system that must be fulfilled in an experiment, if the voltage swing is not to be limited. First, we assume that the mode spectrum in the channel is robust to changes in the channel-gate potential. If it is not, the system is brought out of resonance as V changes, which makes the pumping ineffective. In the Appendix we elaborate a bit more on this point. Second, we assume that the tunneling barriers are relatively high and thin and allow for tunneling far below the top. To this end we set $E_T=0.5$ meV and $R_e=R_c=1$ MΩ. The high values of the tunneling resistances assure that the charge-states are well quantized even when V rises. A promising technique for achieving high barriers is Inplane gating.[21]

Figure 4 shows the transfer characteristic $-V(V_g)$, for $\hat{E}=40$ V/cm, when $C_g=0.4C_\Sigma$ and $C_c=0.1C_\Sigma$. Note that we plot $-V$, which is positive, in order to avoid confusion in the explanations. The result is not very sensitive to a

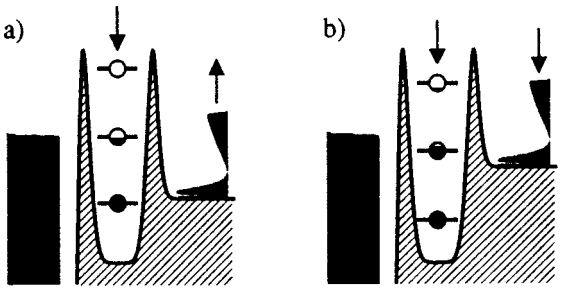

FIG. 5. Level diagrams for two different points on the transfer-characteristic for $R_L = 1000\ \mathrm{M\Omega}$. In a) the mechanism behind the rising edge of $-V$ is illustrated. A charge state is aligned with E_F in the emitter. When V_g is raised slightly, the charge state is lowered via C_g and V starts to decrease. This decrease in V tends to lift the charge state back again via C_c. Ideally the gain is C_g/C_c. In b) the mechanism behind the falling edge of $-V$ is illustrated. Here E_F in the collector has reached a higher charge state. Now a lowering of the charge states is allowed.

variation of $\hat{E}$. Each curve corresponds to a particular value of R_L. The voltage gain, which can be read off as the steepest slope of a curve, is ideally C_g/C_c. This can be understood from Fig. 5(a), where we analyze the rising edge for the case $R_L = 1000\ \mathrm{M\Omega}$.

Let us for the moment put $T=0$, $R_L=\infty$ and ignore all but one charge-state. When this charge state is exactly leveled with E_F, in the emitter the current is blocked since there can be no flow between the emitter and the charge-state. However, when V_g is slightly raised the charge-state is lowered via capacitive coupling. Now electrons start to flow from the emitter into the charge-state. The flow from the charge-state into the collector is already made possible due to the depopulation in the collector. Since the collector is an isolated region, such a flow will accumulate electrons on the collector, and accordingly its electrostatic potential V will become more negative. Because the dot is also coupled capacitively to the collector, the decrease in V tends to lift the charge-state back again. This accumulation stops when the charge-state again is leveled with E_F. This way the electrostatic potential of the dot is regulated to be constant, and from Eq. (6) it is then clear that $\partial V/\partial V_g = -C_g/C_c$. In reality there will be corrections to this simple description that reduces the voltage gain. An estimation of the maximum slope of the $R_L = 1000\ \mathrm{M\Omega}$ curve in Fig. 4 indicates that the gain is about 3.3 and not exactly 4.

The falling edge in $-V(V_g)$ is governed by a different mechanism. As illustrated in Fig. 5(b), a strong back-flow sets in when E_F in the collector tries to rise above the next higher charge-state. This back-flow drains the collector of electrons, and E_F in the collector is thus bound to follow the higher charge-state on its way down. By a consideration similar to that for the rising edge we find a slope: $\partial V/\partial V_g = -C_g/(C_\Sigma - C_c)$.

5. DISCUSSION

An interesting aspect of our findings is that not only Fermi-level properties are probed. The plateaus in the short-circuit current, reflect the energy dependence of the mode-population. If a plateau can be observed for some energy below the Fermi-level, then we know that a single particle description without phase-breaking works well at that energy. The influence of phase breaking is most pronounced for slow electrons since they spend more time inside the channel. Therefore, we expect the smallest plateaus in the short-circuit current to disappear first. There is room for future work on how to account for phase-breaking.

The photovoltage result of section 4 seems less sensitive to the details in the depopulation and it requires a comparatively small field-strength of the THz-field.[11] Photovoltage generation relies in principle only on there being depopulated states in the collector for electrons to tunnel out to. Even though the precise energy-dependence of the depopulation determines the current-driving capability, it does not have much influence on the open-circuit voltage.

The transfer characteristic for large R_L in Fig. 4 is very similar to that of the current biased SET with a large load resistance.[22] In particular it has the same voltage gain, and the underlying mechanisms are similar. This kind of transfer characteristic seems attractive from the application perspective since it allows for poor precision in fabrication of cascaded devices for logic applications. It has good gain, large voltage-swing and shows a saturation-like behavior. Such properties in combination make the precise value of the V_g-threshold, within limits, irrelevant.

A pumped SET has the potential of giving a very simple circuit architecture. Each device works as a tiny voltage-controlled battery, which takes its energy from the THz-field. There is thus no need for power-lines on a chip. Nor do we need clock-signal lines since in principle we can synchronize the devices by modulating the frequency of the THz-field. A similar vision has been presented for devices consisting of chains of islands.[23]

Future research on material science and fabrication technology may bring other ways of realizing a pumped SET than the one we have in mind. The key ingredient is a channel, adiabatically connected to reservoirs, in which the electrons preserve their coherence for 50 wavelengths or so. It would be advantageous to define the boundaries of the device without metallic gate electrodes, using for example etching and regrowth techniques, focused ion-beam implantation or perhaps—many years from now—by tailoring a carbon nanotube.[3,24,25]

CONCLUSIONS

We have analyzed the influence of THz-pumping in one of the leads of a SET. THz-induced depopulation opens the possibility for electrons to leave the dot below the Fermi-level allowing a photocurrent to flow. As the gate voltage is changed, the charge state in the dot acts as a probe of the energy dependence of this depopulation. From the application perspective we present a new way of obtaining voltage-gain from a SET.

APPENDIX

If the walls of the channel move as the electrostatic potential in the collector changes relative to that in the channel-gates, it may result in a limited output voltage swing. From

Eq. (7) we find that the system is brought out of resonance if the mode-spacing $\hbar\Omega$ changes by more than $2V_\omega$. In a typical experiment[26] it takes a change in the split-gate voltage of about 100 mV to go from the threshold of mode 1 to the threshold of mode 2. Assuming a parabolic potential and considering the worst case, in which U_0 does not change at all, we find that this corresponds to a 40% change in the mode-spacing $\hbar\Omega$. From this we conclude that if the mode-spacing is allowed to change only by an amount $2V_\omega$ then the voltage swing must not exceed $-V_{\max}=(100\,\mathrm{mV})2V_\omega/0.40\hbar\Omega$. With our choice of parameters in section 4, we get: $-V_{\max}=3\,\mathrm{mV}$. Thus, we can not rule out such an influence in a gated-2DEG realization of the system. To get good performance it may be necessary to look for a different fabrication technique, for example an etching and regrowth technique.[24]

ACKNOWLEDGMENTS

We acknowledge financial support from the EU (MEL ARI Research project 22953—CHARGE), from the Swedish Research Council for Engineering Sciences (TFR) and from Ericsson Microwave Systems AB. We are grateful to L. Y. Gorelik who proposed the problem and who has contributed in discussion. Also Peter Wahlgren and Mats Jonson are acknowledged for helpful discussions.

*E-mail: tageman@fy.chalmers.se

[1] T. A. Fulton and G. J. Dolan, Phys. Rev. Lett. **59**, 109 (1987).
[2] J. H. F. Scott-Thomas, S. B. Field, M. A. Kastner, H. I. Smith, and D. A. Antoniadis, Phys. Rev. B **62**, 583 (1989).
[3] S. J. Tans, M. H. Devoret, H. Dai, A. Therss, R. E. Smalley, L. J. Geerligs, and C. Dekker, Nature (London) **386**, 474 (1997).
[4] I. O. Kulik and R. I. Shekhter, Zh. Éksp. Teor. Fiz. **68**, 623 (1975) [Sov. Phys. JETP **41**, 308 (1975)].
[5] K. K. Likharev, IEEE Trans. Magn. **23**, 1142 (1987).
[6] L. J. Geerligs, V. F. Anderegg, P. A. M. Holweg, and J. E. Mooij, Phys. Rev. Lett. **64**, 2691 (1990).
[7] H. Pothier, P. Lafarge, C. Urbina, D. Esteve, and M. H. Devoret, Europhys. Lett. **17**, 249 (1992).
[8] J. M. Martinis, M. Nahum, and J. D. Jensen, Phys. Rev. Lett. **72**, 904 (1994).
[9] R. J. Schoelkopf, P. Wahlgren, A. A. Kozhevnikov, P. Delsing, and D. E. Prober, Science **280**, 1238 (1998).
[10] T. H. Oosterkamp, L. P. Kouwenhoven, A. E. A. Koolen, N. C. van der Vaart, and C. J. P. M. Harmans, Phys. Rev. Lett. **78**, 1536 (1997).
[11] D. D. Arnone, J. E. F. Frost, C. G. Smith, D. A. Ritchie, G. A. C. Jones, and R. J. Butcher, Appl. Phys. Lett. **66**, 3149 (1995).
[12] Q. Hu, S. Verghese, R. A. Wyss, Th Schäpers, J. del Alamo, S. Feng, K. Yakubo, M. J. Rooks, M. R. Melloch, and A. Förster, Semicond. Sci. Technol. **11**, 1888 (1996).
[13] L. P. Kouwenhoven, N. C. van der Vaart, A. T. Johnson, W. Kool, C. J. P. M. Harmans, J. G. Williamson, A. A. M. Staring, and C. T. Foxon, Z. Phys. B Cond. Matter. **85**, 367 (1991).
[14] T. Honda, S. Tarucha, T. Saku, and Y. Tokura, Jpn. J. Appl. Phys., Part 2 **34**, L72 (1995).
[15] C. W. J. Beenakker, Phys. Rev. B **44**, 1646 (1991).
[16] D. V. Averin, A. N. Korotkov, and K. K. Likharev, Phys. Rev. B **44**, 6199 (1991).
[17] A. T. Johnson, L. P. Kouwenhoven, W. de Jong, N. C. van der Vaart, and C. J. P. M. Harmans, Phys. Rev. Lett. **69**, 1592 (1992).
[18] L. I. Glazman, G. B. Lesovik, D. E. Khmel'nitskii, and R. I. Shekhter, Pis'ma Zh. Éksp. Teor. Fiz. **48**, 218 (1988) [JETP Lett. **48**, 238 (1988)].
[19] S. E. Laux, D. J. Frank, and Frank Stern, Surf. Sci. **196**, 101 (1988).
[20] Ola Tageman and L. Y. Gorelik, J. Appl. Phys. **83**, 1513 (1998).
[21] H. Tomozawa, K. Jinushi, H. Okada, T. Hashizume, and H. Hasegawa, Physica B **227**, 112 (1996).
[22] M. I. Lutwyche and Y. Wada, J. Appl. Phys. **75**, 3654 (1994).
[23] A. N. Korotkov, Appl. Phys. Lett. **67**, 2412 (1995).
[24] P. Ramvall, N. Carlsson, I. Maximov, P. Omling, L. Samuelsson, W. Seifert, Q. Wang, and S. Lourdudoss, Appl. Phys. Lett. **71**, 918 (1997).
[25] T. Fujisawa, Y. Hirayama, and S. Tarucha, Appl. Phys. Lett. **64**, 2250 (1994).
[26] B. J. van Wees, H. van Houten, C. W. J. Beenakker, J. G. Williamson, L. P. Kouwenhoven, D. van der Marel, and C. T. Foxon, Phys. Rev. Lett. **60**, 848 (1988).

This article was published in English in the original Russian journal. It was edited by R. T. Beyer.

LATTICE DYNAMICS

Structure and lattice parameters of thin C_{60} films

A. T. Pugachev, N. P. Churakova, N. I. Gorbenko, and H. Saadly

Kharkov State Polytechnical University, 310002 Kharkov, Ukraine

A. A. Solodovnik

*B. Verkin Institute for Low Temperature Physics and Engineering, National Academy of Sciences of the Ukraine, 310164 Kharkov, Ukraine**

(Submitted September 29, 1998; revised October 30, 1998)
Fiz. Nizk. Temp. **25**, 298–304 (March 1999)

The structure and lattice parameters of C_{60} fullerite films evaporated in vacuum on the (100) cleavage plane of NaCl at the substrate temperature 290–400 K are investigated in the temperature range 300-5 K by electron-optical methods. Fullerite films have an fcc lattice at room temperature. The film structure changes with the temperature of condensation from epitaxial with the (111) orientation to a disordered and highly nanodisperse structure with a grain size of 4–5 nm. The crystallographic conditions of conjugation of the (100) surface of NaCl and epitaxial C_{60} fullerite films are determined, and the four-position type of their structure is established. The fcc–sc transition temperature and the observed jump in the lattice parameter are close to the corresponding characteristics of bulk fullerite. The temperature dependence of the lattice parameter in the temperature range 100–260 K is used to determine the average linear thermal expansion coefficient α of the films. An increase in α for small thicknesses is a size effect associated with a considerable influence of the surface. A mechanism of formation of the structure of condensed C_{60} fullerite films is proposed on the basis of the obtained results.
 [S1063-777X(99)01103-2]

INTRODUCTION

The discovery of stable polyatomic molecules, viz., fullerenes C_n ($n=\ldots,60,70,\ldots$) in the form of convex polyhedrons, led to a new class of carbon-based solids (fullerites) possessing peculiar properties. The C_{60} molecule having the shape of regular truncated icosahedron was of special interest. The structure and properties of fullerite C_{60} have been investigated by many authors.[1,2]

Pure fullerite C_{60} whose molecules are bound by weak Van der Waals forces at room temperature and under the normal pressure is an orientationally disordered crystal with a face-centered cubic (fcc) lattice. At 260 K, the fcc lattice is transformed into a simple cubic (sc) lattice. In this transition, C_{60} molecules remain in the same positions, but their third-order axis starts being oriented along the [111] direction of the crystal. As a result of an increase in pressure and temperature and also irradiation by visible and ultraviolet light, fullerite C_{60} can be transformed to the well-known phases of carbon (graphite and diamond) as well as other one- and two-dimensional polymerized structure simulating the orthorhombic, tetragonal, and rhombohedral phases.[2,3] Investigations of C_{60} in the thin-film state is of independent interest due to the possibility to vary the structure, substructure, and morphology by varying the condensation conditions.[4]

This paper is devoted to an analysis of the structure, orientation, and lattice parameter of thin C_{60} fullerite films condensed on NaCl. For small thicknesses, the structure of condensed films can be determined not only by the type of the substance being evaporated, but also by the structure of the substrate. The lattice parameter of NaCl ($a=0.564$ nm) is smaller than not only the C_{60} lattice parameter ($a=1.42$ nm, but also the diameter of the molecule itself (0.7 nm). At the same time, the given film–substrate system is characterized by crystallographically favorable relations for the epitaxial growth of films[5] in spite of considerable difference in the lattice parameters for fullerite and NaCl. For instance, two periods of the C_{60} lattice are equal to five periods of the NaCl lattice to within 1%, while two diagonals of the C_{60} fullerite lattice correspond to seven periods of NaCl lattice to within 2%. For this reason, we can expect either parallel or 45°-orientation in condensed films of C_{60}. The information on the lattice parameter of C_{60} films of thickness of a few molecular layers is also of considerable interest.

EXPERIMENT

The films of C_{60} fullerite were obtained by evaporation and condensation of C_{60} single crystal of purity not worse than 99.9% in a vacuum of $\sim 10^{-3}$ Pa. Fullerite crystals were evaporated from a quartz crucible heated by a molybdenum spiral to a temperature ~ 800 K. Cleavage surfaces (100) of NaCl served as substrates. The substrate

temperature T_s changed from 290 to 400 K. Individual crystals whose mass did not exceed $\sim 10^{-3}$ g were evaporated. The thicknesses of the films under investigation varied from 3 to 30 nm. The thickness of the films, which was determined preliminarily by the mass of the sample and the evaporation geometry, was calculated from the change in the frequency of quartz resonator and from the size of the reciprocal lattice site in a direction normal to the plane of the film.[6]

The films intended for electron diffraction and electron microscopy studies were separated in water and recovered by copper electron-microscope meshes so that the film edge indicating the [100] direction in NaCl was parallel to a side of the mesh. The mesh with the film was photographed on a photographic plate with an electron diffraction pattern in electron diffractometer. The photographing conditions ensured the absence of rotation between the mesh and its image. For this reason, the photographic plate with the electron diffraction pattern also contained information on the [100] direction of NaCl. This experimental approach simplified the subsequent analysis of electron diffraction patterns and allowed us to establish the crystallographic directions along which the fullerite film was conjugate to the substrate.

The lattice parameter of films was determined by the method of transmission high-energy electron diffraction using a standard grating. The latter was in the form of a thin annealed aluminum film of thickness ~ 50 nm. The sample and the standard grating were placed in an attachment of the electron diffractometer, whose temperature could be changed controllably from room to liquid helium temperature.[7] The sample and the standard grating were in the same plane perpendicular to the electron beam which passed simultaneously through the sample and the standard. The electron diffraction patterns from the sample and the standard were photographed on the same plate. The electron diffractometer constant $2L\lambda$ (L is the distance between the sample under investigation and the photographic plate and λ the electron wavelength) was determined at each temperature. For this purpose, the available data on the temperature dependence of the lattice parameter for bulk aluminum were used.[8,9]

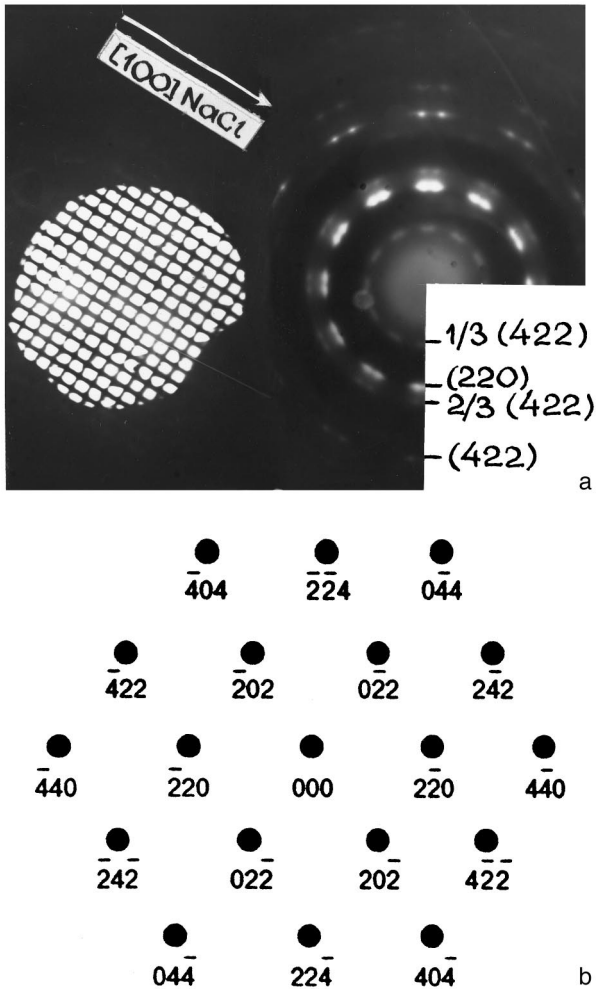

FIG. 1. Experimental electron diffraction pattern from C_{60} films condensed on (001) NaCl at $T_s = 370$ K; the side of a mesh cell indicates the [100] direction of NaCl, $2L\lambda = 13.25$ nm·mm (a) and theoretical diffraction pattern for a (111) monocrystalline film with the fcc lattice (b).

DISCUSSION OF RESULTS

According to the results of electron diffraction and electron-microscopic experiments, the films of C_{60} fullerite were continuous in the given range of thickness and temperatures and had a fcc lattice at room temperature. Electron diffraction patterns ($T_s = 370$ K) contained reflexes of the (220) and (422) type, which are typical of the (111) orientation (Fig. 1a). It should be specially noted that when the film was displaced by ± 3 mm under the electron beam, the form of the diffraction pattern did not change, indicating that the sample had a monocrystalline structure. However, the obtained electron diffraction pattern of C_{60} films differed considerably from that predicted theoretically for the (111) oriented monocrystalline film (Fig. 1b). The difference can be described as follows: we observed 24 reflexes of the (220) and (422) type instead of 6 reflexes expected for the given orientation; according to the results of precision measurements, the angles between neighboring reflexes were 6.6° $\pm 0.2°$ and 23.3° $\pm 0.1°$; reflexes of the type (220) and (422) were located on the same radius vector $\mathbf{r}_{hkl}$ drawn from the zeroth site of the reciprocal space (the center of the electron diffraction pattern); reflexes forbidden by the structural factor for an fcc lattice and characterized by the interplanar distances $d = 0.86$ and 0.43 nm reproducing the arrangement of the main reflexes were present.

According to Fig. 1a, the [100] direction in NaCl is parallel to the radius vector containing the reflexes (220) and (422). This means that the (111)-oriented C_{60} film is conjugate with the substrate according to the following orientational relations:

$$(111)[110]C_{60} \| (100)[100]\text{NaCl}, \tag{1}$$

$$(111)[1\bar{1}2]C_{60} \| (100)[100]\text{NaCl}. \tag{2}$$

The simultaneous fulfillment of relations (1) and (2) indicates that the film contains two types of (111)-oriented crystals turned through 90° relative to one another. The electron diffraction pattern from such a film must be a superposition of two electron diffraction patterns from (111)-

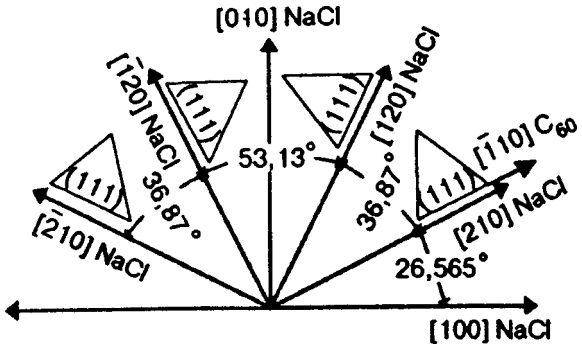

FIG. 2. Epitaxial four-position orientations of (111) nuclei on the (100) surface of NaCl.

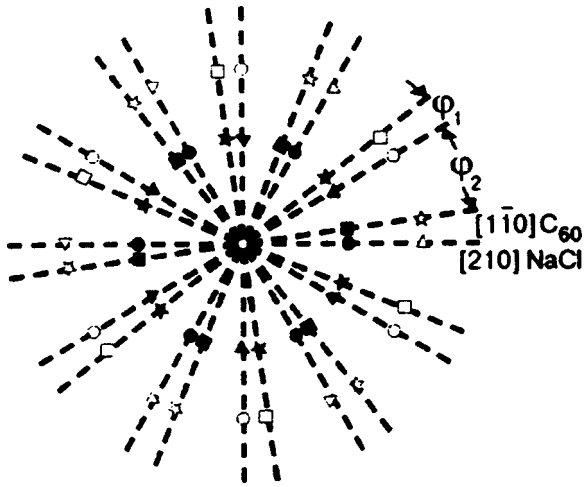

FIG. 3. Theoretical electron diffraction pattern of (111)-oriented C_{60} films with a four-position structure defined by the orientational relations $|1\bar{1}0|C_{60}\|[210]$NaCl (●,○); $|1\bar{1}0|C_{60}\|[120]$NaCl (★,☆); $|1\bar{1}0|C_{60}\|[\bar{1}20]$NaCl (▲,△); $|1\bar{1}0|C_{60}\|[\bar{2}10]$NaCl (■,□) for reflexes of the (220) type (dark symbols) and (422) (light symbols).

oriented monocrystalline films turned through 90° relative to each other. However, electron diffraction patterns from films with such a two-position structure must contain 12 reflexes of the (220) and (422) type instead of 24 observed reflexes. Thus, neither parallel, nor 45°-orientation is realized for such an epitaxial conjugation of the C_{60} films under investigation and the (100)-surface of the NaCl single crystal.

The presence of 24 reflexes (220) and (422) on electron diffraction patterns and the fact that these reflexes lie on the same radius vector indicate that the electron diffraction pattern of the C_{60} film can be regarded as the superposition of four diffraction patterns. This means that the film has a multiposition structure, and the following orientational relation of a more general form must hold:

$$(111)[110]C_{60}\|(100)[hK0]\text{NaCl}. \tag{3}$$

This relation permits the nucleation and growth of crystallites in four equivalent orientations, ensuring the four-position structure of thin C_{60} fullerite films.

The information on the $[hk0]$ direction can be obtained if we know the exact position of the direction [100] in NaCl on the electron diffraction pattern. The [100] direction in NaCl was determined experimentally on electron diffraction patterns to within $\pm 5°$. In this case, the $[hk0]$ direction was determined by comparing the obtained electron diffraction patterns with the theoretically constructed patterns for a multipositional nucleation. It should be noted that the angle between $\mathbf{r}_{220}$ and $\mathbf{r}_{422}$ on the electron diffraction pattern from a monocrystalline film with the (111) orientation is 30° (Fig. 1b). For this reason, taking into account the above-mentioned error in determining the [100] direction in NaCl, we analyzed the direction $[hk0]$ the angle between which and the [100] direction in NaCl was in the interval 25–35°. Such directions were [210], [320], and [740]. For these directions of conjugation of the C_{60} film and NaCl, theoretical electron diffraction patterns were constructed for films with four-position structure. The model of the structure of such a film is shown in Fig. 2. By way of an example, Fig. 3 shows an electron diffraction pattern for the (111)-oriented C_{60} film in which the closely packed direction [110] is parallel to a direction of the [210] type in NaCl. The electron diffraction pattern contains only the most intense reflexes of the (220) and (422) type. The electron diffraction patterns in which the [110] direction is parallel to the [320] and [740] direction have the same form. These diffraction patterns differ only in the angles φ_1 and φ_2. For this reason, a comparison of experimental and theoretical electron diffraction patterns was carried out for the angles φ_1 and φ_2. Table I generalizes the results of precision measurements of angles φ_1 and φ_2 between adjacent reflexes on experimental (Fig. 1a) and theoretically constructed electron diffraction patterns for a four-position nucleation. The table contains only the results for the directions [210] and [320] for which the values of φ_1 and φ_2 are close to the experimentally observed values. It follows from the table that $[hk0]$ corresponds to the direction [210] to within the error in the measurements of the angles.

The four-position structure of epitaxial films of C_{60} fullerite is in accord with the results of electron microscopic studies. According to the data on dark-field images in the light of reflexes (220), the films were polycrystalline in structure (Fig. 4). The average size of crystallites was ~35 nm. Thus, an epitaxial film contains four types of (111)-oriented crystals each of which has the closely packed direction [110] parallel to a direction of the [210] type in NaCl. The formed nuclei of C_{60} fullerite are oriented so that their (111) plane is parallel to the (100) plane of NaCl in four equivalent azimuthal positions characterized by a rotation through the angles 36.87° and 53.13° relative to the [111] axis (see Fig. 2). For this reason, the films with such a structure give an electron diffraction pattern (see Fig. 1a) which

TABLE I. Values of angles φ_1 and φ_2 on theoretical and experimental diffraction patterns from (111)-oriented films with a four-position structure.

	Angles, rad.	
Orientation (theory)	φ_1	φ_2
$\|1\bar{1}0\|C_{60}\|\|210\|$NaCl	6.8	23.2
$\|1\bar{1}0\|C_{60}\|\|320\|$NaCl	7.4	22.6
Experiment	6.6±0.2	23.3±0.1

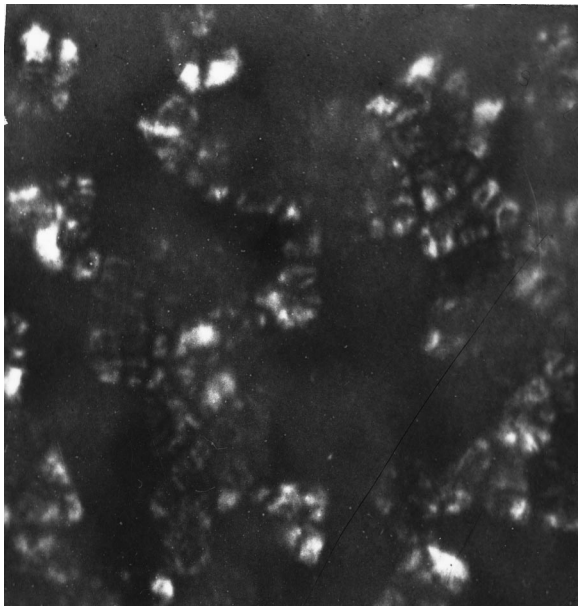

FIG. 4. Electron microscopic dark-field image in the light of (220) reflexes of a C_{60} fullerite film of thickness 4.5 nm. Magnification $\times 120000$.

can be regarded as a superposition of four electron diffraction patterns from monocrystalline films (Fig. 1b) rotated through the above angles relative to the [111] axis.

Thus the emergence of additional reflexes of (220)- and (422)-types and their mutual arrangement on electron diffraction patterns from thin C_{60} fullerite films with (111)-orientation can be explained successfully by the model of the structure formed as a result of nucleation and growth of (111)-oriented C_{60} crystalliltes in four equivalent positions on the (100)-surface of NaCl.

It was noted above that electron diffraction patterns contained reflexes forbidden by the structural factor for the fcc lattice, which can be identified as reflexes of the type 1/3 (422) and 2/3 (422) associated with stacking faults.[10,11] For the (111) orientation, a film with an fcc lattice can be presented as a sequence of alternating layer $ABC,ABC,\ldots$. If the number of layers over the film thickness is not equal to $3n$, where n is an integer, the above-mentioned additional reflexes are formed. It follows hence that for small thicknesses (~ 10 nm and smaller) and interplanar spaces $d_{111} = 0.82$ nm in fullerite, the intensity of these reflexes can be comparable with the intensity of the main reflexes and must decrease with increasing thickness. Such a situation is observed experimentally in the C_{60} fullerite films under investigation. The multipositional type of the structure is responsible for the increase in the number of extra reflexes to 24, and they reproduce the arrangement of matrix reflexes.

It should be noted that in spite of the point-like form of electron diffraction patterns recorded in a wide electron beam, the perfection of the epitaxial films of C_{60} fullerite under investigation is intermediate between texturized and monocrystalline films.

Figure 5 shows the temperature dependence of the lattice parameter for a fullerite film with a four-position structure. The film thickness was 4.5 nm. It follows from Fig. 5 that the lattice parameter changes from 1.418 nm ($T = 300$ K) to

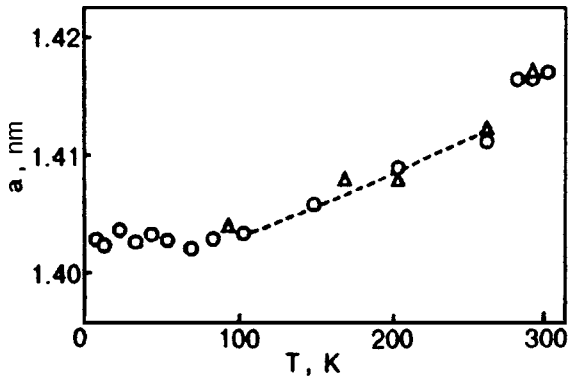

FIG. 5. Temperature dependence of the lattice parameter of a C_{60} film of thickness ~ 4.5 nm: circles and triangles correspond to independent experiments.

1.404 nm ($T = 5$ K). The phase jump $\Delta a/a = 0.35\%$ observed at $T = 260$ K is associated with a phase transition from the fcc to sc lattice. The obtained dependence $a(T)$, the fcc–sc transition temperature, and the observed jump in the lattice parameter of the films are close to similar data for bulk fullerite.

The average thermal expansion coefficient α is determined from the $a(T)$ dependence for the temperature range 260–100 K. The value of this coefficient for the oriented phase is $\alpha = 33 \times 10^{-6}\,\mathrm{K}^{-1}$, which is almost twice the value of $\alpha = 19 \times 10^{-6}\,\mathrm{K}^{-1}$ for bulk fullerite[12] and is in good agreement with the estimates obtained earlier.[13] The value of α increases with decreasing thickness. Such a size effect of thermal expansion is apparently due to the effect of the surface.

Figure 6 shows a typical electron diffraction pattern of C_{60} films condensed on (100) NaCl at $T_s = 290$ K. The form of the electron diffraction pattern did not change when the sample was tilted through an angle of $\pm 30°$ relative to the electron beam, indicating the absence of any orientation. The electron diffraction pattern contained broad halo-shaped rings typical of the amorphous, nanodisperse, or amorphous–

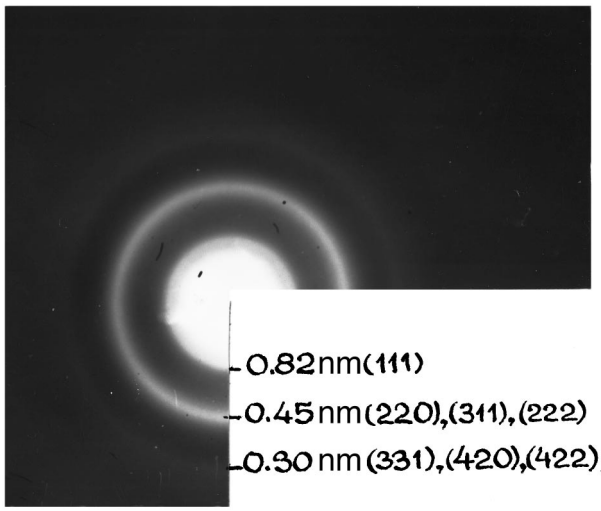

FIG. 6. Electron diffraction pattern of C_{60} films condensed on (100) NaCl at $T_s = 290$ K, $2L\lambda = 13.25$ nm·mm.

nanodisperse states. Crystallites of the size 4–5 nm can be resolved on dark-field electron images, which is an evidence of the nanodisperse state. The rings observed on electron diffraction patterns can be identified in the fcc structure of fullerite. For example, the first three rings correspond to interplanar distances $d \simeq 0.82$, 0.45, and 0.30 nm. The ring with $d \sim 0.82$ nm is close to the (111) position of the line from C_{60}, while the second and third rings are superpositions of rings (220), (311), and (222) with $d = 0.502$, 0.428, and 0.410 nm and (331), (420), and (422) with $d = 0.326$, 0.317, and 0.290 nm, respectively. The line (200) was missing due to size relation between the diameter of the C_{60} molecule and the parameter of the fcc lattice of fullerite.[14]

The above-mentioned size of blocks in disoriented fullerite films corresponds to three parameters of the C_{60} lattice. This means that crystals of such a size contain $\sim 10^2$ molecules of C_{60}. According to theoretical calculations,[15] icosahedral, i.e., quasi-crystalline structure is favorable for crystallites with such a degree of dispersion. It can easily be verified that the size of the icosahedron constructed from 12 C_{60} molecules is ~ 2 nm. In other words, each block contains 8 icosahedrons if we presume that the shape of the blocks is isotropic. A more detailed analysis of the obtained results from the point of view of the quasi-crystalline structure requires additional experimental data.

Thus, the structure of thin C_{60} films may change over a wide range from a disordered nonodisperse (amorphous-type) to well-oriented epitaxial structure upon the variation of condensation conditions.

A typical feature of the obtained films is their continuity for small thicknesses (~ 3 nm), which was monitored in experiments by the method of high-resolution (~ 0.2 nm) electron microscopy. The continuity for small thicknesses of the films is attained either by layer-by-layer monocrystalline growth, or by the formation of the amorphous structure of the film. The observed structure contradicts the layer-by-layer growth concept. The amorphous state is formed in the films under the conditions of confined mobility of atoms, molecules, or clusters of the substance being deposited. For substances with a monatomic composition of vapor (e.g., metals), the amorphous structure is observed only at low (helium) temperatures of the substrate. At higher temperature of the substrate including room temperature, the amorphous structure is observed for substances with a continuous composition of vapor (carbon, germanium, or silicon).[4]

The large mass of C_{60} molecules is an important factor limiting the mobility of fullerene during condensation. These considerations and experimental data (continuity for small thicknesses and the four-position type of the structure) suggest that condensed fullerite films are formed according to the mechanism vapor→disordered (amorphous) state→ordered state. The amorphous phase is formed at first stages of condensation followed by crystallization and recrystallization at higher temperatures under the orienting effect of the substrate.

*E-mail: solodovnik@ilt.kharkov.ua

[1] V. M. Loktev, Fiz. Nizk. Temp. **18**, 217 (1992) [Sov. J. Low Temp. Phys. **18**, 149 (1992)].
[2] V. V. Brazhkin and A. G. Lyapin, Usp. Fiz. Nauk **166**, 893 (1996) [*sic*].
[3] A. M. Rao, Ping Zhou, Kai-An Wang *et al.*, Science **259**, 955 (1993).
[4] L. S. Palatnik, M. Ya. Fuks, and V. M. Kosevich, *Mechanism of Formation and Substructure of Condensed Films* [in Russian], Nauka, Moscow (1972).
[5] L. S. Palatnik and I. I. Papirov, *Orientational Crystallization* [in Russian], Metallurgiya, Moscow (1964).
[6] P. Hirsch, A. Howie, R. Nicholson *et al.*, *Electron Microscopy of Thin Crystals*, London (1965).
[7] S. I. Kovalenko and V. A. Godovannyĭ, Prib. Tekh. Éksp. **No. 2**, 235 (1967).
[8] B. F. Figgins, G. O. Jones, and D. P. Riley, Philos. Mag. **1**, 747 (1956).
[9] M. E. Straumanis and C. L. Woodard, Acta Crystallogr., Sect. A: Cryst. Phys., Diffr., Theor. Gen. Crystallogr. **A27**, 549 (1971).
[10] D. Cherns, Philos. Mag. **30**, 549 (1974).
[11] W. B. Zhao, X.-D. Zhang, K. J. Luo *et al.*, Thin Solid Films **232**, 149 (1993).
[12] L. S. Fomenko, V. D. Natsik, S. V. Lubenets *et al.*, Fiz. Nizk. Temp. **21**, 465 (1995) [Low Temp. Phys. **21**, 364 (1995)].
[13] A. T. Pugachev, N. P. Churakova, and N. I. Gorbenko, Fiz. Nizk. Temp. **23**, 854 (1997) [Low Temp. Phys. **23**, 642 (1997)].
[14] S. Amelinckx, C. van Heurck, D. van Dyck, and G. van Tendeloo, Phys. Status Solidi A **131**, 589 (1992).
[15] B. W. van de Waal, J. Chem. Phys. **98**, 4909 (1993).

Translated by R. S. Wadhwa